Institut für Bio- und Geowissenschaften (IBG), Pflanzenwissenschaften (IBG-2), Forschungszentrum Jülich

Photoassimilates Transport and Distribution in Sugar Beet Taproots affected by Biotic Stress and Shoot Manipulations

Dissertation

zur Erlangung des Grades

Doktor der Agrarwissenschaften (Dr. agr.)

der Agrar-, Ernährungs- und Ingenieurwissenschaftlichen Fakultät
der Rheinischen Friedrich-Wilhelms-Universität Bonn

von
Kwabena Mensah Agyei

aus
Kumasi, Ghana

Bonn 2026

Referent: Prof. Dr. Uwe Rascher
Korreferentin: Prof. Dr. Anne-Kathrin Mahlein

Tag der mündlichen Prüfung: 16.03.2026

Angefertigt mit Genehmigung der Agrar-, Ernährungs- und Ingenieurwissenschaftlichen Fakultät der Universität Bonn

“You might not think you know enough, don’t let that deter you.
It’s all part of growing up”
Damian “Jr. Gong” M

Summary

Background and Motivation: Exogenous factors such as diseases, herbivory damage and mechanical manipulation may disrupt photoassimilates transport and distribution between source and sink organs in plants, possibly affecting the economic value of the plants. A current economically relevant example is the syndrome “basses richesses” (SBR) disease, which is prevalent in sugar beet and already spreads to other crops. The thesis investigates how photoassimilates transport and allocation dynamics in sugar beet taproot are altered spatially and temporally by SBR, partial defoliation and partial shading; aiming to provide mechanistic understanding of how exogenous factors affect source-sink dynamics in sugar beet.

Materials and Methods: In this thesis, a combination of two tomographic methods, magnetic resonance imaging (MRI) and positron emission tomography (PET), using ^{11}C as tracer was employed to non-invasively determine SBR effects on structural growth and photoassimilates distribution within the developing taproot over several weeks. Compartmental modeling for long-distance tracer transport in plants was used to characterize photoassimilates transport properties in sugar beet taproots. In follow up experiments, the effect of shoot manipulations like partial defoliation and partial shading on the distribution of recently fixed photoassimilates was investigated.

Results: MRI analysis revealed a deformed cross-sectional anatomical structure, a reduction in taproot volume and width of inner cambium ring structures upon SBR disease. PET analysis revealed a heterogeneous distribution of labeled photoassimilates for diseased plants, but transport velocities were not affected by SBR disease. However further analysis of tracer transport properties revealed that transport velocities vary locally inside the taproot and over the developing sugar beet taproot. Partial defoliation had no distinct effects on recently fixed photoassimilates distribution homogeneity. On the contrary, partial shading induced a sequential redistribution of recently fixed photoassimilates, towards attaining homogeneity in the distribution of photoassimilates resources within sugar beet taproot.

Conclusions: The findings indicate that healthy sugar beet taproot redistributes photoassimilates when parts of connecting shoot vasculature is disturbed. But when the vasculature of the taproot is altered by a biotic stressor (as in the case of SBR), photoassimilates distribution becomes limited at the infected sectors, thereby affecting sink capacity and the development of taproot sink organ.

Zusammenfassung

Hintergrund und Motivation: Exogene Faktoren wie Krankheiten, Fraßschäden oder mechanische Eingriffe können den Transport und die Verteilung von Photoassimilaten zwischen Quellen- und Senkenorganen in Pflanzen stören und somit den ökonomischen Wert der Pflanzen verringern. Ein aktuell wirtschaftlich relevantes Beispiel ist die Krankheit Syndrome “basses richesses” (SBR), die vor allem in Zuckerrüben verbreitet ist und sich zunehmend auf weitere Kulturarten ausbreitet. Die vorliegende Arbeit untersucht, den Einfluss von SBR, pratieller Entblätterung und Beschattung auf die Dynamik in Transport und Allokation von Photoassimilaten in der Zuckerrübenrübe. Dadurch soll ein mechanistisches Verständnis der Auswirkungen von exogenen Faktoren auf die Quelle-Senke-Dynamik in der Zuckerrübe gewonnen werden.

Material und Methoden: In der vorliegenden Arbeit wurde eine Kombination zweier tomographischer Verfahren eingesetzt - Magnetresonanztomographie (MRT) und Positronen-Emissions-Tomographie (PET) mit ^{11}C als Tracer -, um nichtinvasiv die Auswirkungen der SBR-Krankheit auf das strukturelle Wachstum und die Verteilung der Photoassimilate innerhalb der sich entwickelnden Rübe über mehrere Wochen zu erfassen. Ein Kompartimentmodell für den Ferntransport von Tracern in Pflanzen wurde verwendet, um die Transporteigenschaften von Photoassimilaten in Zuckerrübenrüben zu charakterisieren. In nachfolgenden Experimenten wurde untersucht, wie Eingriffe am Spross - wie partielle Entblätterung und partielle Beschattung - die Verteilung der kürzlich fixierten Photoassimilate beeinflussen.

Ergebnisse: Im Fall der SBR-Krankheit zeigte die MRT-Analyse eine deformierte Querschnittsanatomie sowie eine Verringerung des Rübenvolumens und der Breite der inneren Kambiumringe. Die PET-Analyse ergab eine heterogene Verteilung der markierten Photoassimilate bei erkrankten Pflanzen, während die Transportgeschwindigkeit durch SBR nicht beeinflusst wurde. Eine weiterführende Analyse der Transporteigenschaften zeigte jedoch, dass die Transportgeschwindigkeiten je nach vertikalem Abschnitt oder radialer Zone innerhalb der sich entwickelnden Rübe variieren. In den Manipulationsexperimenten wurde beobachtet, dass eine teilweise Entblätterung keine deutlichen Auswirkungen auf die Homogenität der Verteilung der kürzlich fixierten Photoassimilate hatte. Im Gegensatz dazu führte eine teilweise Beschattung zu einer sequentiellen Umverteilung der kürzlich fixierten Photoassimilate, mit dem Ziel, eine homogene Verteilung der Ressourcen innerhalb der Zuckerrübenrübe zu erreichen.

Fazit: Die Ergebnisse der vorliegenden Arbeit zeigen, dass eine gesunde Zuckerrübe die Verteilung von Photoassimilaten anpasst, wenn Teile des Sprossgefäßsystems beeinträchtigt sind. Wird jedoch das Gefäßsystem der unterirdischen Rübe durch einen biotischen Stressfaktor- wie im Fall von SBR – verändert, wird die Verteilung der Photoassimilate ungleichmäßig, daraus folgt eine Einschränkung der Senkenkapazität und der Entwicklung des Rübenorgans.

List of abbreviations

°C	Degree Celsius
^{11}C	Carbon-11 isotope
$^{11}CO2$	Carbon dioxide labeled with carbon-11 isotope
^{13}C	Carbon 13 isotope
^{14}C	Carbon 14 isotope
c	Circa
2D	Two dimensional
3D	Three dimensional
3PGA	Three-Phosphoglyceric Acid
C3	Three-carbon pathway
BBCH	Biologische Bundesanstalt, Bundessortenamt und Chemische Industrie
CC	Companion cells
cq	Quantification cycle
DAI	Days after inoculation
DAP	Days after planting
DNA	Deoxyribonucleic acid
EPPO	European and Mediterranean Plant Protection Organization
FAO	Food and Agricultural Organization
FZJ	Forschungszentrum Jülich
H	Heterogeneity
HSP20	Heat Shock Protein 20
IfZ	Institute of Sugar beet Research
IIP	Intra measurement intensity projection
LED	Light emitting diode

M02 Module 2

MAM Minutes after manipulation

min Minutes

MIP Maximum intensity projection

MRI Magnetic resonance imaging

OECD Organization for Economic Co-operation and Development

P protein Phloem protein

PET Positron emission tomography

PP Phloem parenchyma

qPCR Quantitative polymerase chain reaction

ROI Region of interest

RTD Rubbery taproot disease

SE Sieve elements

SLL Single leaf labelling

SBR Syndrome “basses richesses”

TAC Time activity curve

WSL Whole shoot labelling

List of figures

Table of Contents

CHAPTER 1

General Introduction

[t] Sections of this chapter draw upon and, adapt concepts and texts originally published in author's article: **Agyei K. et al., 2025. Plant Phenomics 7: 100053. https://doi.org/10.1016/j.plaphe.2025.100053.** Some background concepts and contextual paragraphs from the article's introduction were adapted here to provide a broader foundation in Chapter 1 of this thesis.

1 General Introduction

Autotrophic plants fix atmospheric carbon dioxide, convert it into sugars, which are allocated to different organs to enhance growth and storage of carbon (Braun et al., 2014). The phloem mediates the long-distance translocation of photoassimilates from source to sink organs (Hardtke, 2023), a process fundamental to plant growth, development, and reproductive success (Babst et al., 2019; Lazar, 2003). When exposed to stressors, plants modify their allocation strategies to suit current needs, thereby enhancing resilience (Castrillón-Arbeláez et al., 2012; Ferrieri et al., 2013; Paine et al., 2012; Schwachtje et al., 2006; Vargas-Ortiz et al., 2013). Monitoring carbon allocation in plants is challenging owing to several factors, including the complexity of phloem physiology and limited technologies available for direct and precise estimations (Babst et al., 2019; Broussard et al., 2023). Understanding carbon allocation in plants will guide strategies to optimize production systems and help feed the growing global population amid climate change (Braun, 2022). This thesis determines transport and partitioning of recently fixed photoassimilates in sugar beet plants exposed to stressors.

1.1 The sugar beet crop

Sugar beet (*Beta vulgaris* L.) is a biennial dicotyledonous plant belonging to the chenopodiaceae family (Artschwager, 1926; Hoffmann et al., 2021; Misra & Shrivastava, 2022). Sugar beet accumulates sugar in the taproot during vegetative development (i.e. during the first year) and switches to reproductive development after vernalization when flowers and fruits are produced (i.e. during the second year) (Misra & Shrivastava, 2022). Although sugar beet can last for more than one year, it has a commercial lifespan of about 5-6 months. It is a temperate crop, grown purposely for commercial sugar production (Hoffmann et al., 2021). Following sugarcane, sugar beet is the second largest raw sugar producer worldwide (Misra & Shrivastava, 2022). According to OECD & FAO (2025) report about twenty percent of the world's sugar supply is derived from sugar beet. In 2022, the world's sugar beet production was estimated to be approximately 260 million metric tons (Statista, 2023). The major producers of sugar beet include countries in Europe, North America and some parts of Asia. In Europe, the major sugar beet producing countries include France, Germany, Netherlands, Belgium and Poland (Hoffmann et al., 2021).

1.1.1 Cultivation, development and morphology

Commercial sugar beet is mostly cultivated from spring to autumn (Hoffmann et al., 2021). Seeds of sugar beet are usually sown directly in soils at a depth of 1-2 cm. Rows of plants are spaced at about 40-70 cm

with in-row distance of approximately 20 cm to achieve a final plant density of c. 80 to 100 thousand plants per hectare (Märländer et al., 2003). Germination of sugar beet seeds is weather dependent, and it requires optimal temperatures ranging between 22-25 °C (Hoffman et al., 2021). Thermal time can be used to predict time of emergence (Gummerson, 1986). The first true leaves appear some few days after emergence. The number of leaves can increase up to between 37 and 40 during the growing season (Milford, 1973). As older leaves senesce and are replaced by younger ones, total leaf area declines because the new leaves are smaller than the wider, older ones. Therefore, crop canopy cover tends to decline from its maximum in summer to autumn (Kenter et al., 2006). Compared to the tail, the crown of sugar beet is broadened and assumes a cone-shape at its apex. On top of the crown sit the leaves (Misra & Shrivastava, 2022). The leaf of sugar beet has a petiole which is attached to the crown. Storage root development initiates early as leaf development, but leaf development is dominant at early stages (until c. 100 days after sowing) (Hoffman et al., 2021). The storage root of a well-formed sugar beet plant has one taproot (Artschwager, 1926).

1.1.2 Sucrose distribution and storage in sugar beet taproot

Sugar beet is a C3 plant, meaning the initial product formed during photosynthesis is a three-carbon compound called Phosphoglyceraldehyde (3PGA). 3PGA is converted to glucose and fructose which later forms sucrose (Lazar, 2003), making sucrose the major photoassimilates compound stored in sugar beet taproot, unlike other storage root species that store starch (Hennion et al., 2019). Orthostichy and vascular anastomosis influence the distribution patterns of photoassimilates within a sugar beet plant (Joy, 1964; Zamski & Azenkot , 1981). Even though vascular anastomosis exists, photoassimilates resources in the sink are preferentially imported from orthostichous source leaves (Jahnke et al., 2009; Joy, 1964). Therefore, heterogeneity in shoot sector specific resource capture and contribution owing to leaf age or size, coupled with orthostichy can make the distribution of photoassimilates within sink organs heterogenous (Jahnke et al., 2009; Joy, 1964).

Early anatomical investigations of sugar beet taproot, such as those by Artschwager (1926), provided comprehensive descriptions that remained important for subsequent studies. Per the descriptions by Artschwager (1926), a cross-section of sugar beet taproot, whether young or mature, shows several cambium rings which are also referred to as annular zones. Cambium rings formation is induced by leaves during early stages development and maintain intimate connection to these leaves for sucrose supply (Zamski & Azenkot, 1981) to enhance storage root development (Artschwager, 1926; Milford, 1973). Cambium rings comprise of rings of vascular tissues which are also referred to as vascular rings (Milford,

1973). Sucrose is stored in the vacuoles of parenchyma cells, particularly in the broad storage parenchyma located between the vascular rings (Artschwager, 1926; Hoffmann et al., 2021; Märländer et al., 2003). At early stages when the sugar beet plant is about 6 weeks old, it possesses about six cambium rings. The plant continues to add more cambium rings as it develops and can reach up to 12-15 at full maturity. In the inner zone (usually 1-6 rings for a mature taproot) rings have a wider distance between them and are often approximately equidistant from each other (Milford, 1973; Zamski & Azenkot, 1981). At the periphery, rings are relatively close to each other and are often undifferentiated (Artschwager, 1926; Hoffmann, 2010; Zamski & Azenkot, 1981). Hence the inner ring zone is mostly considered as hotspot for sucrose accumulation. Ring characterization such as width, area and density is a good proxy for quantifying storage root performance, especially when exposed to biotic and abiotic stressors, and a selection criterion for breeding (Artschwager, 1930; Hoffmann, 2010; Metzner et al., 2014; Milford, 1973; Schmittgen et al., 2015).

1.2 Mechanisms of phloem transport

The phloem is a nutrient and sugar rich vascular tissue (Bové & Garnier, 2003). Even though it is critical for plant growth and development, it's one of the least-understood organs in plants (Braun, 2022; Broussard et al., 2023; Lewis et al., 2022). It consists of a transport conduit, i.e. sieve tubes, which is responsible for long-distance transport of photoassimilates in plants (Braun, 2022; van Bel, 1993). During long-distance transport, the phloem pathway can be divided into three consecutive functional zones, each performing a distinct role: collection, transport, and release phloem (Reviewed by Malinowski et al., 2024; Schepper et al., 2013). Sucrose produced by photosynthetically active plant organs is loaded into the sieve tubes of the collection phloem either symplasmically or apoplasmically (Braun, 2022; Braun et al., 2014; Demmig-Adams et al., 2014; Godt & Roitsch, 2006; Muller et al., 2014; Schepper et al., 2013; van Bel, 1993). In plants that exhibit symplasmic loading, sucrose passively moves through the plasmodesmata from the mesophyll cells to enter the sieve tube elements. For species that exhibit apoplasmic loading, sucrose moves actively to the sieve tube elements via the plasma membrane (Demming-Adams et al., 2014; van Bel, 1993). The accumulation of solutes in source leaves creates a very high osmolarity, thereby attracting water from the xylem into the sieve tubes (Braun et al., 2014; Schepper et al., 2013). This raises the osmotic pressure within the cells. For sink organs, solutes are removed from the sieve tubes into adjacent parenchyma cells (Braun et al., 2014). The associated water returns to the xylem, this lowers the pressure within sieve tubes (Braun, 2022). According to Münch's (1930) hypothesis, osmotic pressure differences

between source and sink organs drive the bulk flow of phloem sap, transporting sucrose through the sieve tubes.

In the transport phloem, phloem sap may be released into lateral sinks. These lateral sinks support the continuous leakage and retrieval of solutes in and out of the transport pathway; a process referred to as leakage-retrieval mechanism. The leakage-retrieval mechanism regulates the pressure gradient between sources and sinks, ensuring a steady flow of solutes. The mechanism is based on a balance between unloading of sucrose out of the sieve element companion cell complexes into the surrounding apoplast and their subsequent reloading into the sieve element companion cell complexes (Reviewed by Schepper et al., 2013). In the release phloem, sucrose exists the sieve element through plasmodesmata or are effluxed into the parenchyma cells in sink tissues by symplasmic or apoplasmic movement (Braun, 2022; Ross-Elliott et al., 2017). Differences in the solute concentration within sink compartments drives post-sieve element transport by diffusing solutes via the plasmodesmata bridges (Patrick & Offler, 1996). While transport by diffusion is probable, movement by bulk flow is predominant in sinks that accumulate high concentration solutes (Godt & Roitsch, 2006; Jammer et al., 2020; Patrick & Offler, 1996; Ross-Elliott et al., 2017). Ross-Elliott et al. (2017) proposed convective phloem unloading, a term which describes the combination of both diffusion and bulk flow as the main mechanism that regulates phloem unloading within belowground sink organs.

In sugar beet plants, the *BvSUT1* transporter gene is known to be responsible for the loading of sucrose into the phloem companion cells in source leaves (Nieberl et al., 2017; Vaughn et al., 2002) while *BvTST2.1* transporter gene is known to be associated with unloading of sucrose into the vacuole of sugar beet taproot sinks (Jung et al., 2015). Jammer et al. (2020) indicated that sucrose metabolism enzymes are highly active in the phloem and cambial sites to aid unloading in sugar beet taproots. Per the findings of Godt & Roitsch (2006), sugar beet utilizes both symplasmic and apoplasmic pathways during phloem sap unloading in the taproots. According to Schepper et al. (2013) the retrieval process of the leakage-retrieval mechanism is active and mediated by sucrose symporters. The presence of the BvSUT1 proton-coupled sucrose symporter in phloem of taproot tissues (Jung et al., 2015) suggests evidence of leakage-retrieval mechanism in sugar beet taproots. After sucrose is unloaded into the sink organ, sucrose can be used either as an energy source or as a building block for growth and for the biosynthesis of storage compounds (Rodrigues et al., 2020). Sink strength, which describes the capacity of sink organs to mobilize and store sucrose from source organs influences development and final economic value of plants (Lazar, 2003). The

sink strength depends on sink size and sink activity, i.e. the total weight of the sink tissue and the rate of uptake of photosynthates per unit weight of the sink tissue (Lazar, 2003).

1.3 Biotic factors affecting phloem sap distribution and transport: the case of Syndrome “basses richesses” (SBR) disease of sugar beet[ł]

The nutrient rich nature of the phloem tissue makes it a target for biotic exploiters (Bendix & Lewis, 2018; Lewis et al., 2022). In most cases phloem-restricted pathogens enter the phloem through insect vectors like aphids, psyllids, and planthoppers during feeding on plants (Bosco & Tedeschi, 2013). This enables them to arrive directly at the deeply located phloem (Bendix & Lewis, 2018; Santi et al., 2013). When pathogens arrive at the phloem, they manipulate several aspects to draw nutrients or weaken the plants’ immune system (Malinowski et al., 2024). Plant cells respond to the presence of phloem-restricted pathogens by inducing callose deposition or aggregation of P proteins at the sieve plates. This could lead to phloem occlusion and programmed cell death, thereby impairing phloem transport. The physical blockage of phloem sap transport can lead to reduced long distance transport (Fig. 1.1; Bendix & Lewis, 2018; Malinowski et al., 2024). Because the phloem is buried deeply in the plant, coupled with its high sensitivity to tissue damage, precise probing into phloem activity during biotic attack remains challenging owing to limited technologies available for direct and precise estimations of the phloem activity (Babst et al., 2019; Broussard et al., 2023; Lewis et al., 2022). Several phloem-restricted diseases have become increasingly prevalent worldwide and are causing substantial yield losses (Summarized by Bendix & Lewis, 2018). The case of Syndrome “basses richesses” (SBR) disease of sugar beet will be investigated in this thesis.

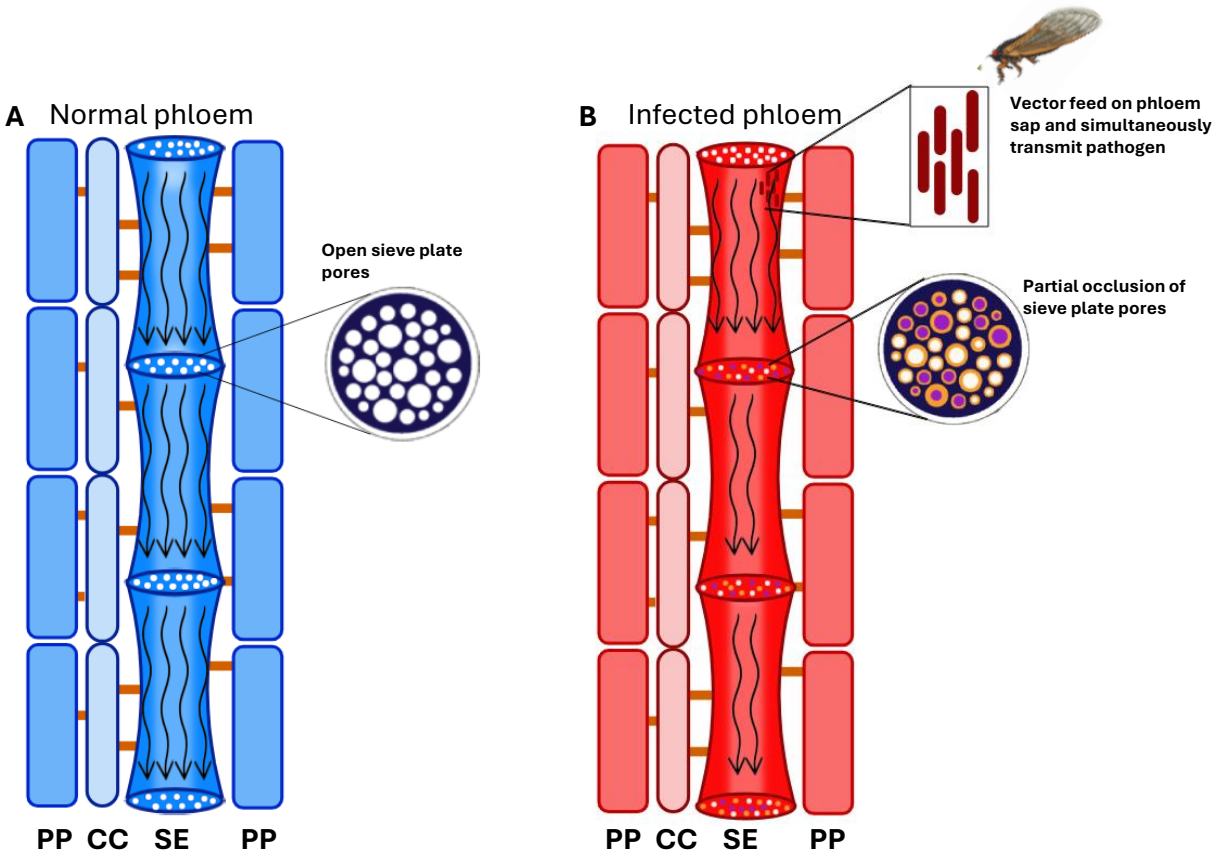

Figure 1.1. Features of the phloem conducting tissues and modification upon pathogen transmission during feeding of vector on phloem sap. (A) Normal phloem transport and (B) disruption of transport during infection. Pathogens (brown rods) can spread during feeding of insect vectors on phloem sap by inserting their stylet into sieve elements, thereby enabling pathogens direct access into the deeply located phloem tissue (Malinowski et al., 2024). Arrows depict long distance transport via pressure flow. Open pores of sieve plate in the normal phloem enable flow of phloem sap whilst in the infected phloem, sieve plate pores are partially occluded by defense processes triggered by P proteins (purple spheres in sieve pores) and callose deposition (orange spheres in sieve pores). Reduced number of arrows reflects reduced transport rate. Orange lines indicate plasmodesmata adjoining cells. PP; phloem parenchyma, CC; companion cells, SE; sieve elements (adapted from Bendix & Lewis, 2018; Malinowski et al., 2024).

1.3.1 History and geographical distribution of SBR disease

SBR is a phloem-restricted disease known to be associated with sugar beet. Characterized by its French nomenclature, the disease was first reported in 1991 in the Burgundy region of eastern France. In 1992, SBR led to a 50% reduction in the income of growers and the local sugar beet industry (Gatineau et al.,

2002). Over the past years, SBR has been prevalent in mid-Europe where the magnitude of occurrence fluctuates from year to year (Mahillon et al., 2022). According to EPPO (2025) global database, the disease is present in Austria, Czechia, France, Germany, Hungary, Romania, Serbia, Slovakia and Switzerland. SBR can lead to c. 29% reductions in taproot biomass (Bressan et al., 2008) and decrease sugar content from, e.g., c. 18 to 13 % (Sémétey et al., 2007).

1.3.2 Pathogens, transmission vector, disease symptoms and management

SBR is caused by two phloem-restricted plant pathogenic bacteria: the proteobacterium '*Candidatus* Arsenophonus phytopathogenicus' (herein referred to as SBR proteobacterium) and the phytoplasma '*Candidatus* Phytoplasma solani' (herein referred to as SBR phytoplasma; Bressan et al, 2008; Gatineau et al., 2002). SBR phytoplasma has also been associated with rubbery taproot disease (RTD) affecting sugar beet plants (Duduk et al., 2023). SBR is a vector transmitted disease, and hence the pathogens involved in SBR exhibit a tritrophic relationship with their hosts (Bressan, 2014; Bressan et al., 2008; Bressan et al., 2012; Sémétey et al., 2007) and have evolved as endosymbionts (Bove & Garnier, 2003; Bressan, 2014; Bressan et al., 2012). Recent reports indicate that vector and pathogens involved in SBR are already extending to other crops (Behrmann et al., 2023; Mahillon et al., 2025; Witczak et al., 2025). Per a report by Duduk et al. (2023), the pathogens involved in SBR can predispose sugar beet plants to other fungal diseases.

It has been clearly established that the cixiid planthopper *Pentastiridius leporinus* (L.) is the primary vector of the SBR pathogens (Behrmann et al., 2022; Bressan, 2014; Bressan et al., 2011; Gatineau et al., 2002; Pfitzer et al., 2022; Sémétey et al., 2007; Therhaag et al., 2024). However, a recent report by Kreitzer et al., (2025) identified another cixiid planthopper, *Reptalus artemisiae* as a vector of both pathogens associated with SBR.

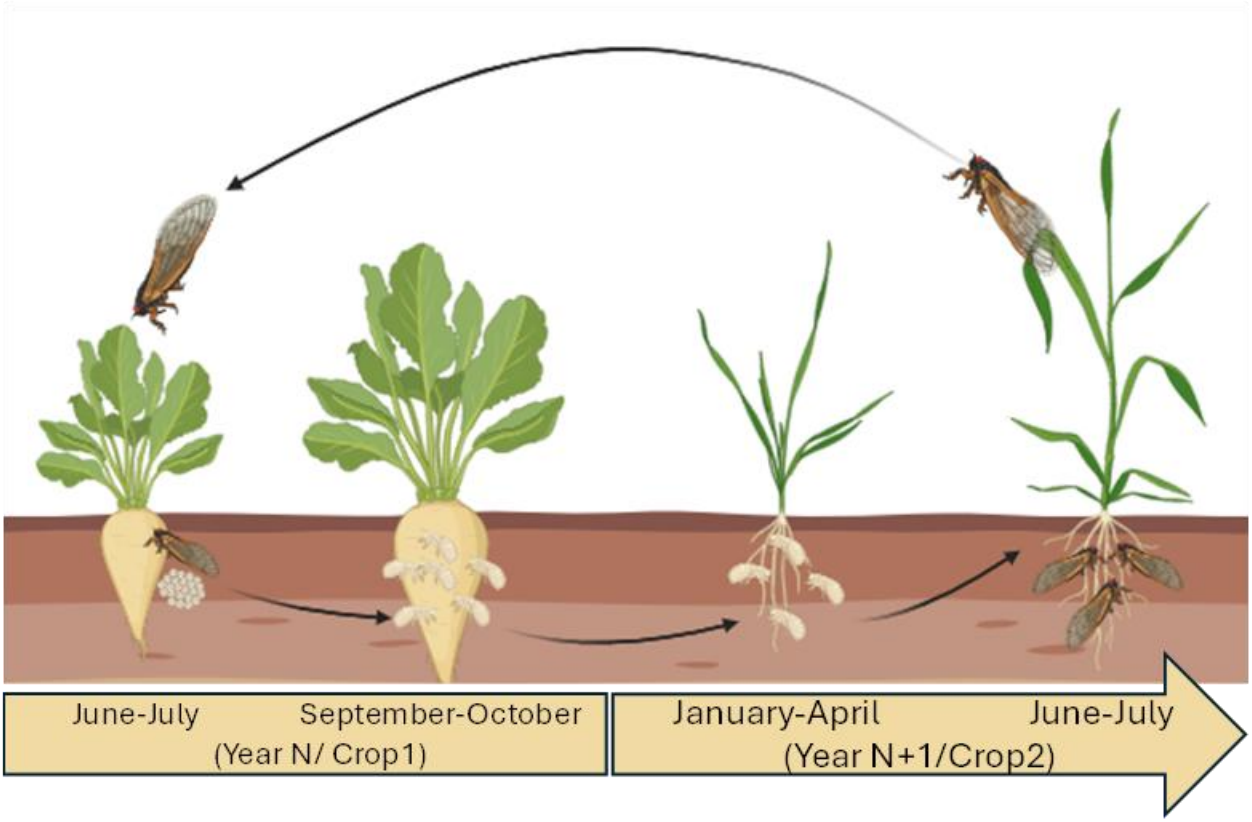

Figure 1.2. Life cycle of *Pentastiridius leporinus* in the sugar beet and wheat crop rotation. Adult planthoppers migrate to sugar beet fields where they feed and reproduce. Terricolous nymphs develop by feeding on sugar beet roots. In the autumn, sugar beet roots are harvested and nymphs diapause as 2nd and 3rd instars. In the following spring, nymphs mature into adults by feeding on wheat root tissue. Upon emergence, the adults migrate to neighboring sugar beet fields (adapted from Bressan et al., 2011).

This thesis will focus on *P. leporinus* since it is the main established vector of the two pathogens associated with SBR disease. In natural habitat, life cycle of *P leporinus* begins when gravid females lay eggs adjacent to sugar beet or potato roots. After 10-15 days, the nymph hatches and develops by feeding on sugar beet roots during summer and autumn. The nymphs overwinter underground. After harvest of sugar beet in autumn nymphs diapause and continue developing on wheat as a succession crop. Emerging adults migrate from wheat to newly sown sugar beet fields (Fig. 1.2; Bressan et al., 2011). The insect vector can acquire the pathogens by either vertical or horizontal transmission (Bressan, 2014). Vertical transmission is predominant with SBR proteobacterium whilst vertical transmission of SBR phytoplasma is not possible (Lang et al., 2025). *P. leporinus* seems polyphagous and can be hosted by several cultivated plants (Berhmann et al., 2023; Lang et al., 2025; Mahillon et al., 2025; Rinklef et al., 2024).

SBR disease symptoms are remarkable for above-below ground crop organs. Older leaves of diseased plants become chlorotic or necrotic. Another symptom observed above-ground is the proliferation of younger leaves (Gatineau et al., 2002). These are symptoms known to be expressed by phloem-restricted pathogens such as phytoplasmas (Bove & Garniar, 2012). As per Detring et al. (2025), SBR disease leads to reduction in area and length of the leaf. Further, a change in spectral response of the leaves, which is a common response by plants to stressors, has been observed for SBR (Detring et al., 2025). In the belowground sugar beet organ, the main symptom observed is the brownish discoloration of vascular bundles (Gatineau et al., 2002; Mahillon et al., 2022). As reported by Gatineau et al. (2002), infections caused by SBR pathogens may lead to the lignification of phloem cell walls. Moreover, analysis of phloem sap indicated a change in the chemical composition of the phloem sap (Kais et al., 2023).

According to Mahillon et al. (2025), the processing quality of belowground crop organs infected with the SBR pathogens is greatly reduced. Currently controlling SBR disease and the associated vector remains a bottleneck (Lang et al., 2025). Classic control strategies for vector transmitted pathogens include eradication or reduction of the vector populations (Bove & Granier, 2003). But the high mobility, the extensive migration period, and the polyphagous nature of the planthoppers (Bressan et al., 2010; Kreitzer et al., 2025) makes eradicating through chemical control difficult. Agronomic practices such as crop rotation and tillage were proposed as a promising approach to control the population of the insect vector (Bressan, 2009). However, this has proven not very efficient (Pfitzer et al., 2024). Even though Lang et al. (2025) proposed a multifactorial management approach to reduce the SBR vector population and the consequences of the disease, the plant hopper continues to be a threat to the sugar industry. A basic understanding of the SBR-sugar beet complexity will propel efforts towards sustainable disease management and hence, Lang et al. (2025) advocated for urgent and collaborative research efforts for the SBR-sugar beet pathosystem.

Controlled transmission assays are required to gain insights into the SBR-sugar beet complexities (Kreitzer et al., 2025). A prerequisite towards robust transmission experiments is the availability of a laboratory colony of the vector (Pfitzer et al., 2022). Therefore, mass rearing protocols and continuous mass rearing of *P. leporinus* have been established (Behrmann et al., 2022; Pfitzer et al., 2022). Under laboratory conditions, the life cycle of *P. leporinus* begins when eggs hatch and pass through five different instar stages. After the fifth stage, the instar matures into adults. Male and female adults copulate and produce eggs which will later hatch to continue life cycle (Behrmann et al., 2022; Pfitzer et al., 2022). Unlike in natural habitats where a successive host plant is required (Fig. 1.2; Bressan et al., 2011), *P. leporinus* can

complete its life cycle on a single plant when reared under control conditions (Behrmann et al., 2022; Pfitzer et al., 2022). **Chapter 2** of this thesis will harness the continued mass rearing of *P. leporinus* at the insect rearing facility of Institute of Sugar beet Research (IfZ) (Pfitzer et al., 2022), enabling establishment of SBR disease through artificial transmission assay for answering relevant questions regarding the SBR-sugar beet interaction.

1.4 Experimental manipulations to explore source-sink dynamics in plants

Often in terrestrial ecosystems, above-ground plant parts are exposed to exogenous factors such as pathogens attack, patchy incident radiation and herbivory damage, all of which can significantly affect phloem sap distribution and hence, resource distribution homogeneity (Orians & Jones, 2001). For example, interference with translocation pathway by shoot herbivory damage can alter the allocation patterns established by proximity and vascular architecture (Ferrieri et al., 2013). Also, Qu et al. (2016) indicated that root herbivore damage induces an uneven distribution of photoassimilates within the lateral root primordia. Experimental manipulations involving physical alteration of source and sink balance have been used to simulate deviations posed by exogenous factors (reviewed by White et al., 2016). Patchy incident radiation and herbivory damage experiments can be simulated through shading and defoliation manipulation experiments (Castrillón-Arbeláez et al., 2012; Ferrieri et al., 2013; Paine et al., 2012; Schmitt et al., 2013; Schwachtje et al., 2006). Defoliation or shading can reduce the overall photosynthetic surface area and incident radiation, thereby decreasing rate of photoassimilates incorporation in plants (Jackson & Caldwell, 1992; Schmitt et al., 2013; Wyse, 1980). During shading or defoliation, plants may remobilize stored photoassimilates to compensate for energy demand such as for vegetative growth (Castrillón-Arbeláez et al., 2012; Schmitt et al., 2013; Vargas-Ortiz et al., 2013). According to Castrillón-Arbeláez et al. (2012), the effects of defoliation on the partitioning of carbon reserves occur rapidly in plants. When faced with such scenarios, plants optimize source and sink strength to regulate the plants by feedback mechanisms (White et al., 2016).

The regulation of source sink balance is critical for plants to achieve a growth rate that is proportional to available resources (White et al., 2016). Moreover, vascular anastomoses permit plants an alternate pathway to supply photoassimilates in the absence of a direct connection between source and sink (Joy, 1964). For instance, Joy (1964) indicated that removing source leaves from one side of the shoot architecture of sugar beet plant can bring about cross distribution of photoassimilates to young sink leaves on the pruned side. Plant organs have the capacity to switch their sink and source identities, which is known to be triggered by environmental stressors (Launay et al., 2009; Rodrigues et al., 2020). Launay et

al. (2009) reported a simultaneous leaf regrowth and sugar content decrease in storage roots after defoliation. When sugar beet plants were exposed to cold stress it was observed that photoassimilates were relocated from taproot to shoots (Rodrigues et al., 2020). Studies by Schmitt et al. (2013) and Paine et al. (2012) indicated that defoliation and shading have different impacts on photoassimilates redistribution and growth patterns in plants, suggesting that plants tolerate shade and herbivory damage with different strategies. The redistribution of photoassimilates reserves after defoliation is governed by demand for resources for shoot regrowth (Schmitt et al., 2013). Unlike in defoliated plants, shaded plants do not invest energy to support shoot regrowth, but rather, the main effect after shading is a higher utilization of photoassimilates reserves for maintaining respiration (Schmitt et al., 2013). According to Vargas-Ortiz et al. (2013) the activity of sugar metabolism enzymes tends to increase in shaded plants compared to defoliated plants. Further, Kebrom (2024) indicated that expression of sugar-inducible gene *SbPFP* is reduced in the buds of defoliated plants when compared to shaded plants. Owing to the differences in the factors triggering redistribution of stored photoassimilates (Schmitt et al., 2013), the varied levels of enzymatic (Vargas-Ortiz et al., 2013) and gene expression profiles (Kebrom, 2024) for shaded and defoliated plants, one can assume that the temporal dynamics of distribution of recently fixed photoassimilates within sugar beet taproot may differ when the sugar beet plant is defoliated or shaded. Unfortunately, information regarding the distribution patterns of recently fixed photoassimilates upon partial defoliation or shading, especially in storage roots is completely missing. To address this knowledge gap, **Chapter 4** of this thesis explores the distribution of recently fixed photoassimilates upon shoot manipulations, providing an initial step toward resolving the problem stated above.

1.5 Exploring phloem sap transport with ^{11}C tracer and tomographic imaging

Temporal and spatial quantification of phloem sap properties such as transport velocities or storage rates by tomographic imaging has been achievable in some plant species and for different experimental scenarios (Karve et al., 2015; Lanzrath et al., 2025; Schepper et al., 2013; Suwa et al., 2008; Windt et al., 2006; Zierer et al., 2025). Most of these studies highlighted phloem sap properties for above ground parts of relatively larger plants (Lanzrath et al., 2025; Schepper et al., 2013; Suwa et al., 2008; Windt et al., 2006; Zierer et al., 2025). This is probably due to the easy accessibility of above-ground plant organs for measurements. Windt et al. (2006) employed magnetic resonance imaging (MRI) to characterize phloem flow dynamics in poplar, castor beans, tomato and tobacco. MRI application for measuring phloem sap velocity in sugar beet is limited presumably due to the large amount of stationary water making it difficult to clearly observe and measure flowing phloem sap (Windt et al., 2006). In most cases, MRI was used to

study the detailed structural development of sugar beet taproot (Hillnhütter et al., 2012; Metzner et al., 2014; Schmittgen et al., 2015).

Pulse labelling of plants with stable isotopes like ^{13}C (Kaiser et al., 2015; Kakouridis et al., 2024) or the long-lived ^{14}C (Gottwald et al., 2000; Joy, 1964; Liu et al., 2012; Rodrigues et al., 2020) and short-lived ^{11}C (Babst et al., 2008; Babst et al., 2019; Hinz et al., 2024; Jahnke et al., 2009; Karve et al., 2015; Lanzrath et al., 2025; Metzner et al., 2022; Qu et al., 2016; Schultes et al., 2025; Yu et al., 2024; Zierer et al., 2025) radioactive carbon isotopes provide unique techniques to track the fate of labeled photoassimilates. With this approach, the axial transport and distribution of photoassimilates within a plant can be monitored. Unlike ^{13}C and ^{14}C which mostly require a destructive approach to analyze photoassimilates transport or distribution in plant organs, the relatively short half-life (20.4 min) of ^{11}C allows for multiple labelling of an individual plant, thereby enabling in-vivo, non-invasive temporal analysis of photoassimilates distribution in plants (Minchin & Thorpe, 2003). Due to its short half-life, ^{11}C applications in plant studies have some limitations. ^{11}C applications must be performed at a close proximity to a cyclotron facility (Minchin & Thorpe, 2003). This probably reduces its fame in plant applications. Moreover, short-term physiological processes are feasible with ^{11}C, but relatively long-term processes such as remobilization are impossible to capture (Minchin & Thorpe, 2003).

In most plant applications, ^{11}C is supplied to leaves in the form of $^{11}CO_2$ where it is incorporated into recently fixed photoassimilates (Babst et al., 2019; Hinz et al., 2024; Janhke et al., 2009; Karve et al., 2015). Depending on the system or biological question at hand, ^{11}C can be applied to single leaf or whole shoot of plants (Babst et al., 2019; Ferrieri et al., 2013; Jahnke et al., 2009; Qu et al., 2016; Schultes et al., 2025). ^{11}C emits high energy positrons which annihilate upon encounter with an electron to produce two high-energy photons. These photons can be detected by positron emission tomography (PET) scanner (Babst et al.,2019; Hinz et al., 2024; Jahnke et al., 2009; Karve et al., 2015). PET scanners typically form a ring around the biological object in question (Hinz et al., 2024). Coincidence events are recorded from all angles of the detectors simultaneously. The 3D distribution of ^{11}C within the biological object is reconstructed from the measured coincidence events through mathematical algorithms (Hinz et al., 2024). The reconstruction of PET measurements is done in frames with a defined time (Hinz et al., 2024). Based on the half-life of ^{11}C, decay correction of PET images is required to account for the radioactive decay of the signal obtained (Babst et al., 2019; Hinz et al., 2024; Karve et al., 2015). Moreover, scatter and attenuation effects presents challenges in the quantitative accuracy of PET data by yielding misaligned and weaker signals (Babst et al., 2019; Hinz et al., 2024; Karve et al., 2015), especially when measuring organs embedded in porous media

(Hinz et al., 2024; Karve at al., 2015). Karve et al. (2015) indicated that attenuation yielded to 55% error in root radioactivity measurements. In plant PET systems, transmission scans are a potent approach to correct for attenuation and scatter effects (Hinz et al 2024; Karve et al., 2015).

1.5.1 Qualitative and quantitative analysis of ^{11}C PET data

Intensity projections of regions of interest in PET images can be analyzed qualitatively by a simple "look-see" method (Babst et al., 2019). Qualitative analysis of PET data generated by $^{11}CO_2$ labelling determines the distribution or allocation patterns of labelled ^{11}C photoassimilates within the biological organ under question based on ^{11}C signal intensity (Jahnke et al., 2009; Miyoshi et al., 2022; Schultes et al., 2025). For example, Jahnke et al. (2009) indicated a sectorial distribution of photoassimilates upon feeding $^{11}CO_2$ to a single leaf of sugar beet plant. Also, Schultes et al. (2025) showed that recently fixed photoassimilates are not translocated into the roots of 6 days old maize plant. By monitoring the allocation pattern of ^{11}C, Miyoshi et al. (2022) proposed that photosynthates are mainly allocated to seminal roots upon water deficit in rice.

For a quantitative analysis, time activity curves (TACs) can be obtained from the regions of interest of the biological organ under study (Babst et al., 2019; Hinz et al., 2024; Karve et al., 2015; Lanzrath et al., 2025). According to Lanzrath et al. (2025) the characteristics of TACs reflect tracer transport properties such as velocity and storage, which benefits functional plant phenotyping. The horizontal distances between TACs determine transport speed (i.e. the smaller the distance from TAC to TAC, the faster the transport velocity and vice versa; see **Chapter 3** for details). Also, the vertical distances between TACs or distances between heights of TACs determines the local storage of tracer in plant samples (i.e. the wider the distance from TAC to TAC, the greater the storage and vice versa; see **Chapter 3** for details). As mentioned briefly above, scatter and attenuation can reduce PET signal intensity (Hinz et al.2024), this poses potentially huge errors in storage analysis. Therefore, scatter and attenuation corrections become inevitable when estimating storage from a PET dataset.

Several methods, either data driven or model based, exist to determine tracer transport dynamics (Summarized by Lanzrath et al., 2025; Minchin & Thorpe, 2003). Based on quantitative PET data, Karve et al. (2015) employed the intercept method to estimate photoassimilates transport and allocation in *Sorghum bicolor*. Also, the dynamics of transport velocity and loss (aka storage) of recently fixed photoassimilates for partially girdled oak tree were unraveled by ^{11}C tracer and PET imaging (Schepper et al., 2013). Recently, Zierer et al. (2025) used ^{11}C and PET to analyze transport velocities in the stem of

cassava plants. The studies of Schepper et al. (2013) and Zierer et al. (2025) employed a compartmental model (Bühler et al., 2014) to characterize tracer transport properties.

Prior to this thesis, there were no studies employing ^{11}C and PET to characterize changes in the distribution of recently fixed photoassimilates in sugar beet taproot due to a biotic stressor. Moreover, information regarding temporal characteristics of ^{11}C transport within the developing sugar beet taproot has not been studied in vivo so far. To address this gap, **Chapters 2 and 3** present both qualitative and quantitative analyses based on a series of short-term ^{11}C PET measurements that were repeated over a six-week period on individual sugar beet plants growing in natural soil following exposure to a biotic stressor.

Bühler et al. (2014) showed the applicability of compartmental tracer transport models to quantitatively analyze TACs obtained from ^{11}C PET measurements of sugar beet plants. Using this method, transport velocities, tracer exchange with surrounding tissues and tracer storage along the highway of transport can be estimated from the TACs (Bühler et al., 2014; Lanzrath et al., 2025). As highlighted by Lanzrath et al. (2025), compartmental models proposed by Bühler et al. (2014) integrate plant mechanistic properties while focusing on a selective subset of physiological parameters, thereby preventing an excessive complexity and overabundance of parameters. Uniquely, this family of models can fit TACs of every ROI simultaneously. As stated by Bühler et al. (2014), the performance of these models depends on plant species and plant parts being observed. Hence, identifying and adopting a model for such analysis requires a careful choice to suit an experimental scenario. For storage type transport, Lanzrath et al. (2025) identified model M02 as the best fitting model from the Bühler models family. Model M02 is a model including flux velocity and storage as parameters, but no other exchange processes. Since storage is a dominant activity during sugar beet taproot development (Jammer et al., 2020; Zhang et al., 2017) model M02 of the Bühler model family, was adopted for analyzing transport properties in sugar beet taproot in **Chapter 3** of this thesis.

1.6 Scope and Objectives

To date, relatively few studies have monitored photoassimilates transport and distribution, and taproot development in sugar beet over an extended period; this thesis addresses this gap. The thesis studies the effect of a biotic stressor, partial defoliation and partial shading on photoassimilates distribution in sugar beet taproot growing under climate chamber conditions. Based on the extensive data obtained from relatively long term repeated ^{11}C labelling and MRI-PET imaging, this thesis strategically explores dynamics in long distance tracer transport properties (Bühler et al., 2014) by further utilizing PET quantitative data.

In follow-up experiments, this thesis investigated the distribution dynamics of recently fixed photoassimilates within sugar beet taproots under partial defoliation and partial shading manipulations. Within this scope, the structure of this thesis encompasses 3 main experimental **Chapters** (i.e. **2, 3** and **4**) and a general discussion **Chapter (5)**. The chapter specific objectives are:

Chapter 2 aimed to elucidate the effect of SBR disease on storage root development and the distribution of recently fixed photoassimilates within sugar beet taproot. More specifically, MRI-PET was employed to non-invasively uncover temporal and spatial alterations caused by SBR disease on cross-sectional taproot anatomical features. In addition, the chapter investigated temporal and spatial photoassimilates distribution within the taproot as the disease progressed.

Chapter 3 aimed to quantify tracer transport velocity and rate of storage of recently fixed photoassimilates within the taproot of sugar beet. Based on the PET data, **Chapter 3** sought to elucidate the effect of SBR disease on temporal dynamics of tracer movement along the vertical axis of sugar beet taproots. Tracer transport velocities and rate of storage of recently fixed photoassimilates within the taproot were quantified using a compartmental model analysis according to Bühler et al. (2014). Specifically, temporal and spatial variations in tracer transport velocities as well as rate of tracer allocation as the tracer travelled along the vertical axis of the sugar beet taproot was analyzed in this chapter.

To obtain more mechanistic understanding, shoot manipulation experiments were performed in **Chapter 4.** The chapter aimed at providing qualitative evidence regarding how shoot architecture and the manipulation of parts of the shoot architecture influences distribution dynamics of recently fixed photoassimilates. Single-leaf labelling in PET was performed to obtain the distribution pattern of recently fixed photoassimilates from a single leaf of sugar beet plant. The effects of single-leaf removal and shading on the spatial and temporal distribution of recently fixed photoassimilates in the taproot are compared.

Chapter 5 is a general discussion of the experimental **Chapters (2, 3** and **4)**. The chapter links the major findings of this thesis and proposes mechanisms regulating phloem sap distribution and transport within sugar beet taproot and deviations upon stressors. Further, the opportunities and challenges of the approaches employed in this thesis are discussed. Future research directions as a build up to the current thesis will be addressed.

CHAPTER 2

This chapter is based on author's published article: K. Agyei, J. Detring, R. Metzner, G. Huber, D. Pflugfelder, O. Eini, M. Varrelmann, A.-K. Mahlein, R. Koller. (2025). Syndrome "basses richesses" disease induced structural deformations and sectorial distribution of photoassimilates in sugar beet taproot revealed by combined MRI-PET imaging. *Plant Phenomics* 7:100053. https://doi.org/10.1016/j.plaphe.2025.100053

Author contributions: KA, JD, AKM, and RK: Conceptualization; KA, RM, GH, DP, OE, and MV: Investigation; RM, DP, MV, and AKM: Resources; DP: Software; KA: Formal Analysis; KA: Visualization; KA: Writing – Original Draft; KA, JD, GH, DP, OE, AKM, RK: Writing – Review & Editing; GH, AKM, and RK: Supervision; RK and AKM: Funding Acquisition.

Overall contribution by KA: 85 %

[#] The background section has been adapted for the purpose of this thesis (to avoid repeating materials included in Chapter 1). The remaining sections of this chapter (Materials and Methods, Results, and Discussion) reproduces author's published article with only minor changes.

2 Syndrome "basses richesses" disease induced structural deformations and sectorial distribution of photoassimilates in sugar beet taproot revealed by combined MRI-PET imaging

2.1 Background[ǂǂ]

Syndrome "basses richesses" (SBR) is a fast-spreading sugar beet disease in mid Europe (Duduk et al., 2024; Kreitzer et al., 2025; Pfitzer et al., 2024). Detailed information regarding mechanisms of disease progression, how the disease alters the anatomical structures and physiology of the taproot, which forms the main economic value of sugar beet, are missing and may reveal insights on how SBR affects the sink organ of the growing plant (see Section 1.3 for more background).

This chapter employed MRI and PET to uncover tempo-spatial effects of SBR on belowground taproot development. The effects of the phloem-restricted pathogen causing SBR, '*Candidatus* Arsenophonus phytopathogenicus', on cross-sectional taproot features and development of taproot volume was observed non-invasively over several weeks, complemented by the investigation of temporal and spatial photoassimilates distribution within the taproot. With this approach, the chapter sought to answer these three main questions:

- From which time point in sugar beet development do SBR symptoms become visible in the taproot?
- How does severity of SBR symptoms in the taproot progress over time?
- Assuming that SBR symptoms are not evenly distributed over the taproot volume: does this distribution change over time?

2.2 Materials and Methods

2.2.1 Experimental Design

Multiple plants of sugar beet (*Beta vulgaris* L.) were grown under controlled conditions and subjected to two treatments, non-inoculated and inoculated with the SBR pathogen '*Ca*. A. phytopathogenicus'. Two non-invasive tomographic imaging techniques (MRI and PET) were employed for belowground taproot phenotyping. All plant samples were subjected to MRI measurements after the inoculation access period. For PET measurements, a subset of samples from each treatment was selected randomly. MRI and PET

acquisitions were performed over a period of six weeks to follow growth dynamics and disease progression. The timeline of the experiments is depicted in Fig. 2.1. The acquired MRI and PET images were reconstructed followed by taproot traits analysis and further quantification of disease effects (Fig. 2.2).

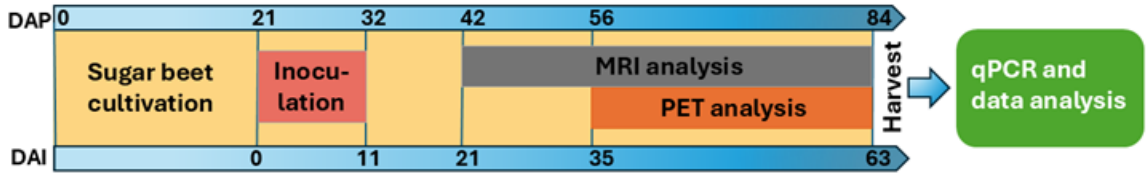

Figure 2.1. Schematic of experimental timeline and processes. Key steps include plant cultivation, SBR disease transmission (inoculation), MRI-PET imaging phase and qPCR-based discrimination between diseased and control samples after harvest. DAP = days after planting, DAI = days after inoculation.

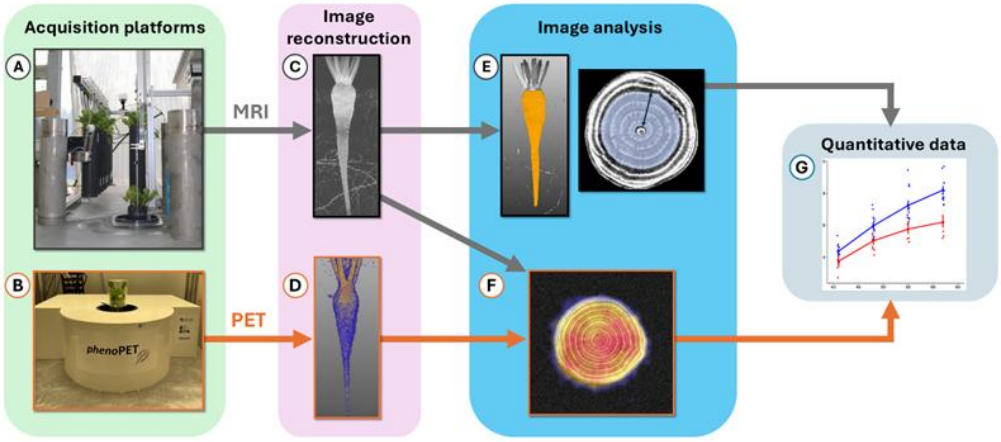

Figure 2.2. Workflow of image data acquisition and analysis. (A) Magnetic resonance imaging (MRI) acquisition platform; (B) Positron emission tomography (PET) acquisition platform; (C) MRI data reconstruction; (D) PET data reconstruction; (E) Taproot segmentation (determined taproot volume in orange) and cambium ring contouring (marked by blue circle with arrow); (F) MRI-PET co-registration, grey image parts represent MRI, colored image parts represent PET; (G) Quantitative trait analysis and visualization.

2.2.2 Soil substrate preparation.

MRI compatible soil substrate (Speyer 2.1, LUFA Speyer, Germany, characterized in Pflugfelder et al. (2017) was oven-dried at 60 °C for 24 hours, demagnetized and prewetted. The resulting soil was filled into PVC pots of 400 mm height and 81 mm inner diameter covered with a nylon meshed-perforated bottom. Soil

moisture was maintained at c. 20 % volumetric water content by regularly watering pots to keep pot weight at a set value established initially with dried soil.

2.2.3 Plant cultivation

A single seed of sugar beet (*Beta vulgaris* L.) genotype BTS 8750 (uncoated) (Betaseed GmbH, Frankfurt, Germany) was planted into each pot at depth of 1 cm. Plants were grown in a climate chamber at 24 °C: 16 °C temperatures, 16 h: 8 h light: dark, and 60% relative humidity. Light was sourced from LED panels (CreeLED Inc, Shanghai, China) with an intensity of 680 µmol m^{-2} s^{-1} at plant level.

2.2.4 SBR transmission assay

For the transmission assay, 21 days old sugar beet plants were transported from Forschungszentrum Jülich (FZJ) to Institute of Sugar beet Research (IfZ) and kept at the planthopper rearing facility of the IfZ. *P. leporinus* adults diseased with γ-3 proteobacterium '*Ca*. A. phytopathogenicus' were acquired from the planthopper rearing facility of IfZ according to Pfitzer et al. (2022). Per tent, four healthy sugar beet plants (BBCH stage 11-12) were exposed to 20 *P. leporinus* planthoppers in 60 * 60 *60 cm rearing tents with a mesh size of 150 µm (BugDorm-2120F, Insect rearing Tent, MegaView Science Co., Ltd., Taichung, Taiwan) for an inoculation access period of 11 days. For the negative control group, plants were kept in rearing tents without planthoppers. During this period, plants and planthoppers were kept under controlled conditions at 22.8 ± 1.0°C, 43.4% ± 6.5% relative humidity and a 16h: 8h light: dark cycle. Light was sourced from a full-spectrum LED panel (Valoya, RX 400, Spektrum NS 1, Helsinki, Finland). The light intensity within the tent was set at 250 µmol $(s\ m^2)^{-1}$. At the end of the inoculation period, all plants were sprayed with the insecticide Imidacloprid (Bayer AG, Frankfurt, Germany) at a concentration of 0.035% according to manufacturer's manual to eradicate the planthoppers. Plants were inspected three days after spraying to ensure that all planthoppers were eliminated prior to the return of the plants to FZJ. At FZJ, plants were cultivated at standard conditions as stated in the plant cultivation section above. We set the time when plant hoppers were introduced in the tents as reference time for the definition of days after inoculation (DAI). Since the measurements of each sample run had to be performed on more than one day, there were time differences between the single samples of up to 13 h for MRI and up to 30 h for PET. As a consequence, measurement times expressed as DAI have an uncertainty of approximately 1 day. In order to prevent a bias in the results we randomly changed the order of plants at each PET imaging date.

2.2.5 MRI measurements

Belowground sugar beet organs were imaged weekly using MRI (van Dusschoten et al., 2016). The MRI set-up includes a robot system which enables automated image acquisition (Fig. 2.2A). The MRI consists of a 4.7 T magnet (Magnex, Oxford, UK) equipped with a MRS console (MR Solutions, Guildford, UK). The vertical orientation of the magnet enables acquiring plant images in their natural vertical inclination. A radio-frequency coil with an inner diameter of 100 mm (Varian, Palo Alto, CA, USA) was used. MR images were acquired with a Spin-Echo Multi-Slice sequence with the following parameters: Repetition time =1250 ms, bandwidth = 400 kHz, horizontal slices with 2.0 mm thickness, in plane resolution 0.2*0.2 mm^2, matrix size 500*500*50, echo time = 10 ms, two averages. The measurement time was approximately 21 min for a soil volume of 10*10*10 cm^3.

2.2.6 $^{11}CO2$ tracer production, Gas exchange system and labelling approach

$^{11}CO_2$ tracer was produced onsite at an 18 MeV fixed-energy cyclotron (IBA Molecular Europe, Louvain-la-Neuve, Belgium). For each shoot labelling, the $^{11}CO_2$ from the cyclotron was trapped on a molecular sieve (Kim et al., 2014). The trapped $^{11}CO_2$ was recovered by heating it up to 200 °C and subsequently flushed into the administration cycle of the gas exchange system. Sugar beet plants were mounted in the field of view of the plant dedicated PET system "*pheno*PET" (Hinz et al., 2024). The whole shoot of sugar beet plant was enclosed in a $^{11}CO_2$ labelling cuvette. Different cuvette sizes of 170, 210 or 260-mm height with a diameter of 81 mm were employed depending on plant age and height. The cuvette was air-tightened and connected to the gas exchange and the $^{11}CO_2$ application system. The serial connections between the gas exchange system, the $^{11}CO_2$ tracer application system and the cuvette enabled gas exchange measurements and the parallel administration of $^{11}CO_2$ to the whole shoot of the sugar beet plants. Each sequence of $^{11}CO_2$ administration was done with approximately 50 MBq of $^{11}CO_2$ for a period of 6 min. Details about functionality of the gas exchange system and procedures of releasing $^{11}CO_2$ in the cuvette were described in Metzner et al. (2022).

2.2.7 PET image acquisition

*pheno*PET was used to acquire tomographic images of ^{11}C tracer within the taproot (Fig. 2.2B). The bore of the *pheno*PET is built in a vertical orientation and has a cylindrical field of view of 180 mm in diameter and 202 mm in height. The resolution of acquired tomographic images comprises of voxel size of 0.9×0.9×1 mm with spatial resolution of 1.8 mm. *pheno*PET is installed in a climate chamber to provide optimal climate conditions for plants during measurements. The climate conditions in this chamber were similar

to the plant cultivation climate chamber. Prior to PET measurements, plants were allowed to acclimate until CO_2 assimilation was stabilized. Image data was acquired for 150 min after each $^{11}CO_2$ pulse labelling. After each measurement, the plants remained in the *pheno*PET climate chamber until the next day and afterwards were transferred back to the cultivation climate chamber.

2.2.8 PET image reconstruction

PET images were reconstructed into 30 frames with 5 min duration (Hinz et al., 2024). Scatter and attenuation corrections were not employed in this chapter. The individual frames were decay corrected such that the image intensity was proportional to the tracer amount in each frame. For data analysis and visualization, maximum intensity projection of the PET tracer over time was used (Fig. 2.2D).

2.2.9 MRI and PET image analysis

After MRI and PET image acquisitions MeVisLab software (version 3.6.1, MeVis Medical Solutions AG, Bremen, Germany) was used to visualize and analyze structural features as well as dynamic ^{11}C tracer distribution patterns inside the taproot.

2.2.10 Analysis of MR images of taproot

For taproot volume quantification, a binary MR image was generated from MR images (Fig. 2.2C), using an image intensity threshold. Fine structures such as root segments were removed using a median filter and subsequently selecting the largest connected component. Finally, the leaf base was selected manually. The remaining volume defined the taproot (Fig. 2.2E). For taproot cross-sectional visualization and quantification, MRI data was visualized in 2D. A qualitative as well as quantitative analysis of taproot cross sectional features was done based on 2D slices at three different vertical positions of the taproot. The positions were chosen similar to the cross-sectional slices at final harvest (Supplementary Fig. A. S1). For quantitative analysis, the ring structures of each taproot sample were contoured manually while excluding the central core (Fig. 2.2E). The mean distance between adjacent contours represented the ring width. Innermost ring width was calculated by summing the width of rings 1-4 (Fig. 2.2E).

2.2.11 MRI- PET Co-registration

To gain insights into ^{11}C distribution patterns, MRI and PET images were co-registered manually. A fixed color scale for all PET images was used for image display (Fig. 2.2F). For MRI images, the color scale needed to be adapted manually between the different time points to compensate for signal changes due to different tuning and matching settings necessary to accommodate the growing taproot and different soil

water levels. To distinguish both modalities, MRI images were presented in grey values whilst PET images were shown in color (Fig. 2.2F).

2.2.12 Determination of intra taproot tracer distribution heterogeneity

The tracer distribution was analyzed in 10 slices of 5 mm thickness each, spread over the taproot. Tracer heterogeneity (*H*) was defined as $H = (p_{80} - p_{20})/p_{50}$, with p_N being the N-th percentile of the tracer distribution. Mean heterogeneity and standard deviation were estimated from heterogeneity of all 10 slices.

2.2.13 Post harvest taproot biomass estimation

Taproots were excavated from pots and cleaned from soil by washing at 63 DAI directly after the last MRI and PET measurements. Fine roots were removed from the taproot with a scalpel. The cleaned taproots were wrapped in paper towels to absorb excess water. Subsequently, they were unwrapped, and their fresh biomass was obtained by weighing on a laboratory balance (Mettler-Toledo GmbH, Giessen, Germany). The taproot diameter was measured with a caliper at the thickest part of the taproot.

2.2.14 Taproot tissue sampling and qPCR detection of 'Ca. A. phytopathogenicus'

Taproot tissue samples were collected from all plants after harvest at three different cross-sections of the taproot (upper section: directly below the pith, mid-section: 2 cm below upper portion and lower section: 3 cm below mid-section) (Supplementary Fig. A. S1). Taproot tissue samples were collected in 1.5 ml centrifuge tubes (Eppendorf AG, Hamburg, Germany) and stored in -80 °C until further analysis. Nucleic acid extraction to determine infection by '*Ca*. A. phytopathogenicus' was performed using the MagMAX Plant DNA kit (ThermoFischer Scientific, Frankfurt, Germany) for all inoculated samples and two non-inoculated samples. The absolute DNA concentration was estimated by using Nanodrop (Ds-11 Spectrometer, Denovix, Wilmington, USA) and diluted with sterile water to a final concentration of c. 20 ng μl^{-1}. Samples were later transferred into 96-well plates (Bio-Rad Laboratories GmbH, Feldkirchen, Germany) for further analysis.

Primer sequences (Supplementary Table A S1) as designed and described in Zübert & Kube (2021) were used to target HSP20 gene sequences of '*Ca*. A. phytopathogenicus'. A qPCR reaction mix comprised 6.3 µl distilled water, 10 µl Maxima Probe qPCR Mix, 0.9 µl of each primer, 0.4 µl of Probe (10µM; Fam-BHQ1 labeled) and 1.5 µl of DNA template. PCR was conducted on a CFX96 real time system C1000 touch thermal cycler (Bio-Rad, Feldkirchen, Germany). qPCR conditions were 95 °C for 3 min, 40 cycles at 95 °C for 15 seconds, 60 °C for 30 seconds. The resulting data was analyzed via Bio-Rad CFX Manager software (version

3.1). In this design, samples can be considered diseased if Cq values are ≤ 35.00 or non-diseased if Cq values are > 35.00.

2.2.15 Statistical analysis

R statistical computing software (version 4.2.1: packages; ggplot2, tidyverse, rstatix and ggpubr) was used for analysis of the data for taproot volume, inner rings and intra taproot tracer heterogeneity. Differences among means were tested using a t-test. Significance levels were set at *** $p < 0.001$, ** $p < 0.01$ and * $p < 0.05$.

2.3 Results

2.3.1 Identification of diseased taproot samples by qPCR analysis and detection of SBR symptoms after harvest

The experimental set-up consisted of 10 inoculated and 10 non-inoculated sugar beet plants. The presence of '*Ca*. A. phytopathogenicus' was confirmed in 8 out of the 10 inoculated plants based on qPCR analysis. Cq values for diseased samples ranged between 23.6 to 29.5 and '*Ca*. A. phytopathogenicus' was detected in three sections in each diseased plant (Supplementary Table A. S2). In addition, cross sections of all diseased taproot showed brownish discoloration of the vascular bundles at harvest (Fig. 2.3L, M, N, and Supplementary Fig. A. S13-S19). Brownish discolorations were localized to specific regions and in some cases were surrounded by healthy tissues (Fig. 2.3, and Supplementary Fig. A. S13-S19). Brownish discoloration was not observed in taproot samples of non-inoculated plants and plants that showed negative for the proteobacterium by qPCR (Fig. 2.3E, F, G, and Supplementary Fig. A. S2-S12). Based on the results of the qPCR analysis and the symptoms observed during destructive analysis, we defined control as non-diseased plants (10 non-inoculated plus two non-diseased inoculated samples). In the following, we number control samples as C1-12 and diseased samples as D1-8.

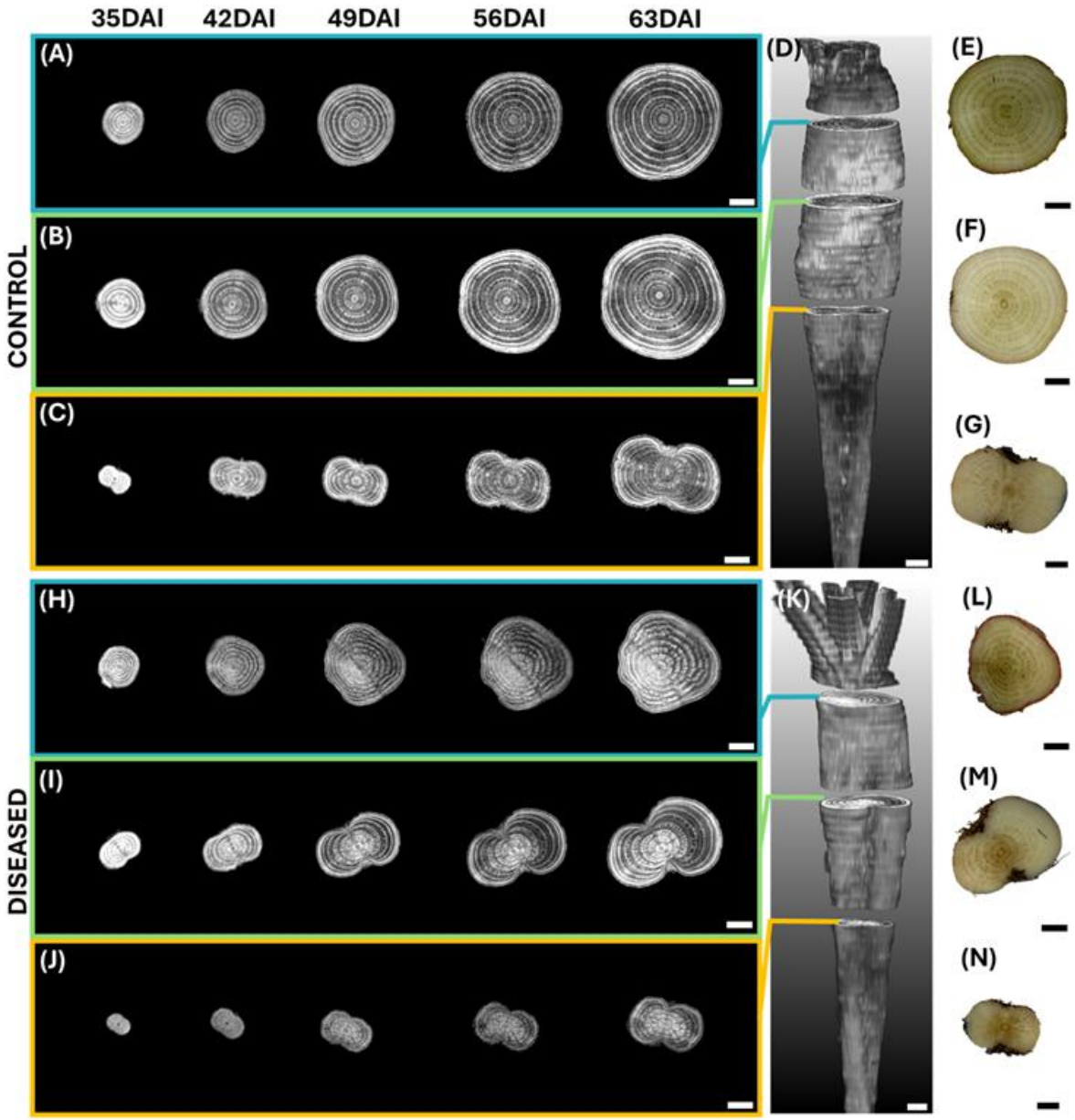

Figure 2.3. Examples of cross-sectional anatomical features at three vertical positions of control taproot C1 (A-G) and diseased taproot D1 (H-N). Grey images (A, B, C, H, I, J) represent slices of MRI acquired at five time-points after inoculation (35, 42, 49, 56 and 63 DAI). (D, K) indicate vertical positions where slices were obtained for control and diseased taproot, respectively. (E, F, G, L, M, N) RGB images show a cross-section of the same control (E, F, G) and diseased (L, M, N) taproots after destructive harvest at 63 DAI. Brownish discoloration in (L, M, N) shows SBR symptoms. Bars, 0.5 cm.

2.3.2 SBR effects on taproot diameter and fresh weight after harvest

At harvest the infection with the SBR proteobacterium reduced fresh weight of the taproots on average from 43.6 ± 1.3 g of control to 33.6 ± 2.1 g (mean ± SE) of diseased taproots. Similarly, mean taproot diameter at harvest was reduced from 29.6 ± 0.5 mm for control plants to 25.7 ± 0.8 mm (mean ± SE) for diseased taproots (Supplementary Table A. S3).

2.3.3 SBR effects on taproot development

To analyze SBR effects on structural taproot development, MRI of belowground taproot was imaged weekly from 21 DAI until 63 DAI. Temporal MRI acquisition was achievable for all samples, except for measuring dates 35, 42 and 56 DAI where one, two and one measurements were unsuccessful, respectively, due to technical problems. Apart from this unsuccessful imaging, the mean of diseased plants for taproot volume and inner rings represented 8 samples whilst mean of control plants represented 12 samples. Quantitative

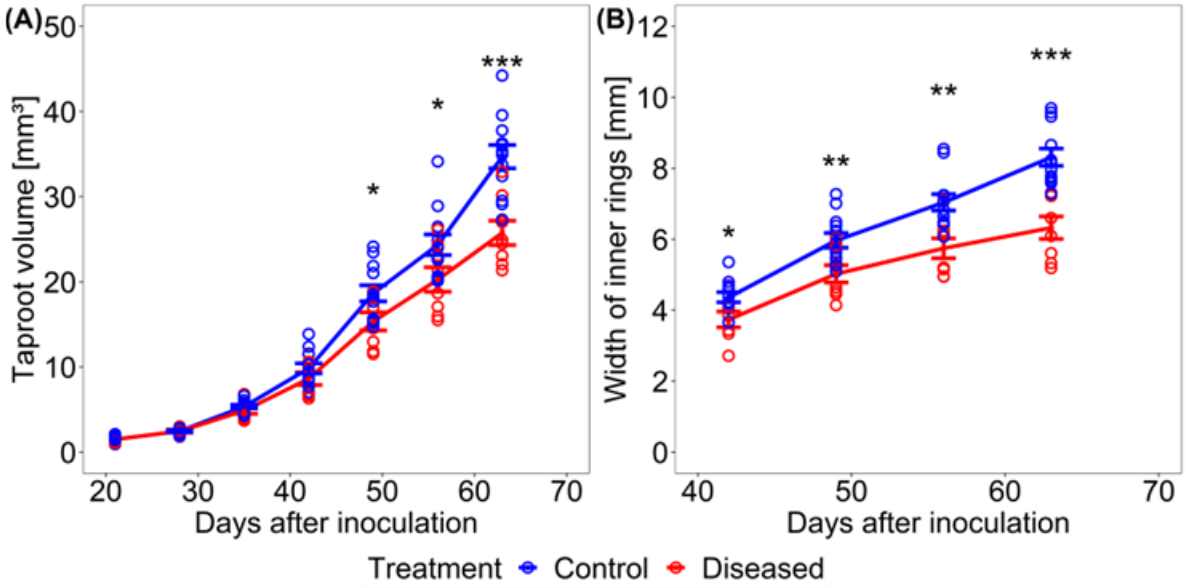

Figure 2.4. Quantification of taproot development by MRI. (A) Taproot volume and (B) inner ring width of control (blue) and diseased (red) taproots over time. Circles represent single values and lines represent their means. Number of replicates n = 12 for control at 21, 28, 35, 49 and 63 days after inoculation (DAI); n = 11 for control at 42 and 56 DAI; n = 8 for diseased at 21, 28, 39, 56 and 63 DAI; n = 7 for diseased at 35 and 42 DAI. Error bars represent standard error. Asterisk marks indicate significant differences in a t-test, *** $p < 0.001$, ** $p < 0.01$, * $p < 0.05$.

image data analysis revealed a significant, progressing reduction in taproot volume in the presence of the SBR proteobacterium. Reduction in taproot volume was significant at 49 DAI until 63 DAI (Fig. 2.4A).

Diseased samples showed a 12, 18, 17 and 26% reduction relative to control samples at 42, 48, 55 and 63 DAI, respectively. Analysis of temporal development of inner taproot ring width showed a significant reduction by the presence of the SBR proteobacterium. Reduction in inner rings was significant earliest at 42 DAI until 63 DAI (Fig. 2.4B). Diseased samples showed a 16, 17, 19 and 24%-decrease relative to control samples at 42, 48, 55 and 63 DAI, respectively.

2.3.4 SBR effects on taproot cross-sectional anatomical features

2D slice images of taproot, obtained from MRI, enabled differentiation of cambium rings, central core, and storage parenchyma for both control and diseased plants (Fig. 2.3 and 2.5). The MRI signal of diseased tissue was clearly distinguishable from healthy tissue in diseased plants. This was prominent for all the three cross-sections at different vertical positions of the taproot (Fig. 2.3H, I, and J). MRI of diseased taproot showed deformed cambium rings with broader indefinite patterns unlike in diseased taproot where cambium structures were definite (Fig. 2.5). Moreover, sections of cambium rings showed a brighter image signal. The pattern of deformations observed by MRI was similar to the brownish colored portions of the taproot cross-sections observed during destructive analysis at harvest.

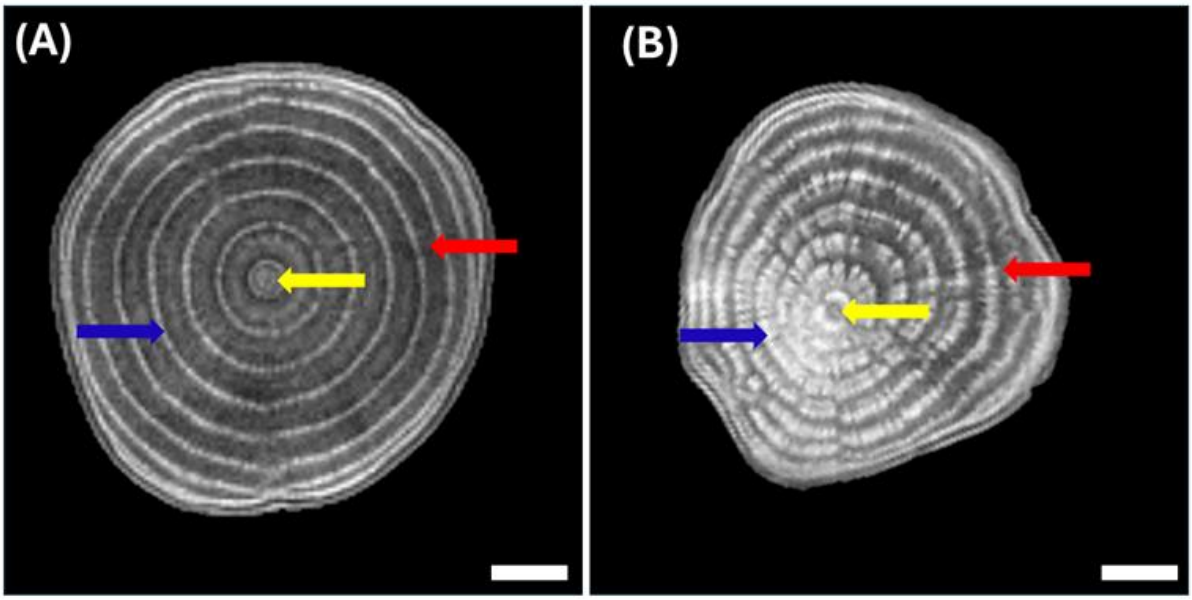

Figure 2.5. Comparison of MRI signal intensity and cross-sectional structures of (A) control taproot C1 and (B) diseased taproot D1 at 63 days after inoculation. Yellow arrows indicate central core, red arrows indicate storage parenchyma and blue arrows indicate cambium ring structure. Diseased taproot shows brighter and smeared ring structure with less phloem parenchyma area as compared to control taproot. Bars, 0.5 cm.

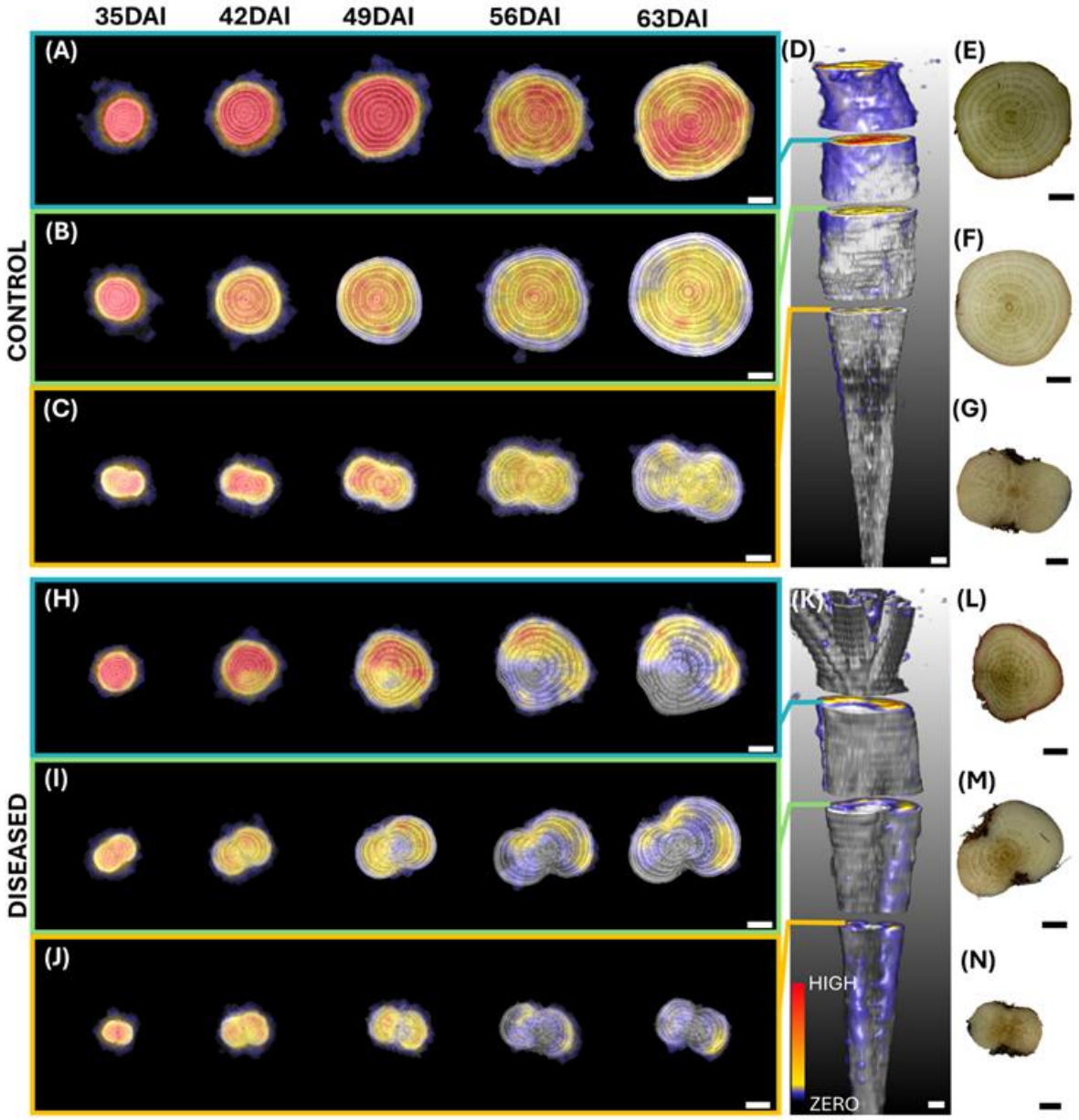

Figure 2.6. Examples of MRI-PET co-registration showing tracer distribution in the developing taproot as well as RGB images of taproot at destructive analysis for control taproot C1 (A-G) and diseased taproot D1 (H-N). Figure layout is same as in Fig. 2.3 except for additional PET images overlaid in color. Areas with cooler colors (grey, blue) indicate no or very low ^{11}C tracer activity while areas with warmer colors (yellow and red) indicate high ^{11}C tracer activity. Bars, 0.5 cm.

2.3.5 SBR effects on distribution of recently fixed photoassimilates within taproot

The effect of SBR on distribution of recently fixed photoassimilates was determined by co-registration of PET images with the structural MRI images (MRI-PET). PET acquisition was performed for three non-inoculated and three inoculated samples, except that one image was unsuccessful during acquisition at imaging day 42 DAI. Two out of the three inoculated plants dedicated for PET acquisition tested positive for '*Ca*. A. phytopathogenicus'. Therefore, in the PET and subsequent heterogeneity analysis, the mean of control plants represented four samples whilst the mean of diseased plants represented two samples apart from the reported unsuccessful imaging.

Qualitative analysis considered 2D slices at three different vertical positions of the taproot that were similar to the cuttings for determining the presence of SBR protobacterium by qPCR at final harvest. For control samples, photoassimilates were distributed homogenously over the taproot slices (Fig. 2.6A, B, C, Supplementary Fig. A. S20-S22 and Video A. S1). A sectorial distribution of recently fixed photoassimilates was observed in the presence of the SBR proteobacterium (Fig. 2.6H, I, J, Supplementary Fig. A. S23 and Video A S2). The signal intensity of tracer was either missing or very low for a sector of the developing taproot. The sectorial distribution was visible from 42 DAI and was predominant at later imaging dates (56 and 63 DAI). This sectorality was extending throughout the taproot from top to bottom (Video A S2). Sectors of the taproot with low to no tracer signal were similar to areas that showed brownish

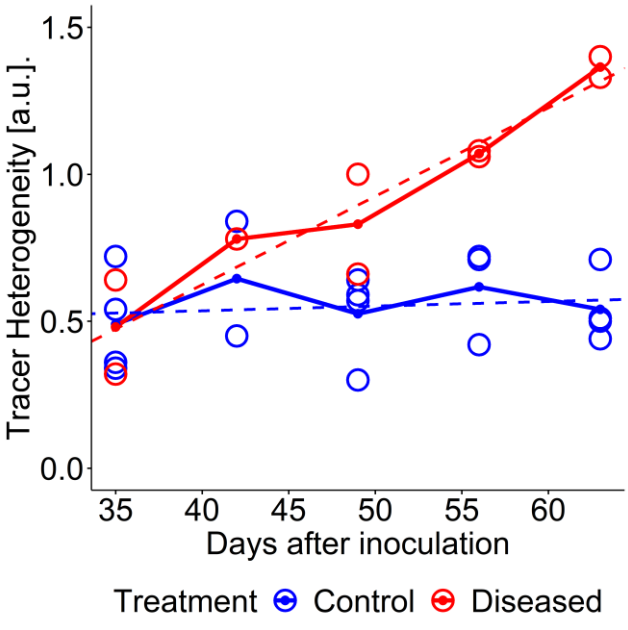

Figure 2.7. Temporal development of mean heterogeneity *H* of tracer distribution within taproots. Heterogeneity was averaged over 10 slices of taproot for control (blue) and diseased (red) taproots, respectively. Circles represent values per taproot and lines represent their means. Blue and red dotted lines represent linear regressions for control (R^2 = 0.011) and diseased (R^2 = 0.859) taproots, respectively. Number of replicates n = 4 for control at 35, 49 and 63 DAI; n = 2 for control at 42 DAI; n = 3 for control at 56 DAI; n = 2 for diseased at 35, 49, 56 and 63; n = 1 for diseased at 42 DAI. Individual intra taproot mean and standard deviation values for slices are displayed in Supplementary Table A S4.

discoloration. For quantitative analysis, the heterogeneity (*H*) of tracer distribution was determined within 10 slices of the taproot. (Fig. 2.7, and Supplementary Table A. S4). Heterogeneity *H* increased by a factor of 2.8 in diseased plants over the course of the experiment. In control plants the tracer distribution within the taproot remained homogeneous (Fig. 2.7, and Supplementary Table A. S4). In general, the intensity of tracer signal in the developing taproot detected by PET was reduced for all plants. This could be explained by the fact that the same amount of ^{11}C tracer was being diluted into larger taproot volume at later imaging periods.

2.4 Discussion

In this chapter MRI and PET were employed to uncover temporal-spatial effects of the biotic stressor SBR on belowground taproot development. This was the first time that individual plant development was monitored non-invasively with MRI-PET over such a long time period. Also, this study was the first to analyze the effect of a biotic stressor on photoassimilates distribution within individual sugar beet taproots.

2.4.1 SBR disease effects on morphological and physiological sugar beet taproot development

Repeated MRI measurements showed a decrease in volume and inner ring width of diseased taproot relative to control taproot samples. A similar result was reported by Schmittgen et al. (2015) for sugar beet diseased with *Cercospora* leaf spot. The symptoms observed by MRI started at 42 DAI and continued progressively until harvest at 63 DAI, when plants were 84 days old (Fig. 2.4). While the effect of SBR pathogen on taproot volume did not start before 49 DAI, cambium ring structure could have been affected even earlier. But cambium ring analysis was possible earliest at 42 DAI due to the time required for secondary thickening of the taproot. At this stage, the four innermost rings were clearly defined and separated from each other by phloem parenchyma unlike outer ring structures which could not be distinguished (Fig. 2.3). This was expected, since the widening of phloem parenchyma due to storage is observed in the innermost rings of the taproot at this stage (Artschwager, 1926).

In addition to inner ring width, qualitative changes in vascular structures exerted by SBR (Figs. 2.3, and 2.5) were detected also as early as 42 DAI. Deformations of parts of the vascular structures are some of the microscopic and macroscopic symptoms known to be present in the taproot of SBR diseased plants (Gatineau et al., 2002). However, there is no clear explanation yet for the observed broadened and interrupted cambium rings in cross-sections of the taproot (Fig. 2.5B). These features were confined to specific sectors of the observed cross-sections and could be distinguished from surrounding tissues which

looked healthy. Affected regions identified early with MRI and brownish discolored regions seen in the destructive analysis conformed with the sectors of the taproot which received little to no recently fixed photoassimilates (Fig. 2.6H, I, and J). The latter could be detected from DAI 49 onwards, i.e., one week later than the symptoms detected with MRI, probably because of the lower spatial resolution of PET compared to MRI.

2.4.2 Linking shoot architecture to distribution of belowground SBR disease symptoms

The inoculation period started at BBCH stage 11-12 and ended at BBCH stage 14, i.e., when there were just two to four fully expanded leaves. These leaves initiate the formation of the three innermost cambium rings and later stay connected to maintain an intimate relationship between leaves and cambium rings (Artschwager, 1926). Since phloem-restricted pathogens are translocated with photoassimilates from source to sink organs (Christensen et al., 2004; Tatineni et al., 2008), the pathogen infection can be assumed to be established in the innermost cambium. Development of outer rings after the inoculation period was not directly affected by the pathogen, explaining the observation of infected inner rings surrounded by healthy tissue (Supplementary Fig. A. S17, and A. S19).

The specific sectorality of disease symptoms we observed in some cases (Fig. 2.3H, L, and 2.6H, L) could be explained by a possible selective nature of the transmitting vector. Selection of a specific side of the shoot architecture or leaf by the vector will be directly proportional to abundance of SBR pathogens at a specific sector of the taproot, because vascular architecture plays a relevant role in the phloem sap distribution (Jahnke et al., 2009; Joy, 1964).

2.4.3 Possible mechanistic explanations for observed SBR disease symptoms

The relative difference in taproot volume and inner ring width increased over time for control and diseased plants (Fig. 2.4). In parallel, the heterogeneity of tracer distribution increased over time (Fig. 2.7). This indicates that SBR effects on taproot physiology and growth worsened as the disease progressed, which would be possible only if the pathogen spread inside the taproot. It is suggested that the increasing portions of the cross-section with little to no signal in the PET measurements (Fig. 2.6H-J) are related to a growing abundance of the pathogen in these regions.

The observed distribution patterns of photoassimilates could be due to low metabolic activity of adjoining leaves which supplied photoassimilates to specific taproot sections. Schmittgen et al. (2015) suggested this mechanism for their observation of reduced growth of inner ring structures under pathogen attack, albeit for a different pathosystem. Another explanation would be that the distribution pattern is driven by

reduced metabolic activity of both source and sink cells. In a case of a source leaf with little or no metabolic activity, neighboring source leaves might compensate for the supply of photoassimilates to other parts of the sink. This would be possible due to the subtle existence of vascular connections between leaves and cambium rings. Such compensatory mechanism in resource distribution has been observed in a case of partially defoliated sugar beet (Joy, 1964). Owing to this and the observed abnormalities in MRI as well as brownish discolored tissue in destructive analysis, we are suggesting that the observed sectorality is driven by dead sink cells, which leads to a compromised structural integrity exerted by SBR. Thus, SBR weakens host tissue structure and may cause leakage of cellular contents. The leakage could be the reason for the abnormal cambium ring formation observed in MRI. Another explanation could be that the SBR pathogen might secrete effectors or toxins in the phloem (as suggested by Christensen et al. (2004) for a different phloem-restricted pathogen) which trigger host responses and cause the morphological changes (Greenberg & Yao, 2004).

2.4.4 Perspectives for future studies

The current approach enabled monitoring allocation dynamics of recently fixed photoassimilates, thus uncovering short term dynamics of tracer distributions. On the other hand, using ^{11}C as tracer limits clues regarding relatively long-term remobilization of photoassimilates in the taproot. Long-term analysis of storage dynamics of photoassimilates may reveal how a stressor induces a switch in sink-source identities of the developing taproot (Rodrigues et al., 2020). Other carbon isotopes such as the stable ^{13}C tracer (Kakouridis et al., 2024) or long-lived ^{14}C (Joy, 1964; Rodrigues et al., 2020) could be used in combination with ^{11}C to investigate short- and long-term carbon dynamics at the same time (Schultes et al., 2025).

Apart from sizes, quality in the form of taproot shape (Märländer et al., 2003) and tissue strength (Hoffmann, 2010) are important parameters for sugar beet processing. Effects exerted on sugar beet tissue structure and content by pathogens affect the processing quality of taproot (Rossi et al., 2000). It is assumed that SBR will not only affect taproot volume as seen in this study, but also the geometry of the developing taproot. Therefore, further experimentation and implementation of algorithms for the detection and quantification of SBR effects on taproot geometry will be beneficial. Also, a detailed tissue characterization of taproot under specific stress scenarios would provide a strong basis for quantifying performance and harnessing tissue strength in future breeding programs (Hoffmann, 2010; Kleuker & Hoffmann, 2021).

Further experimentation is needed to link shoot physiological traits to belowground taproot traits. This will provide a holistic overview of functional and structural relationships among above-and below-ground organs of sugar beet during SBR disease progression

It might be possible to determine the distribution of the pathogen by using MRI-PET for image guided tissue sampling, followed by qPCR to quantify pathogen presence in contrasting regions of interest. The same approach of image guided-sampling with MRI-PET could also be applied to investigate the role of sucrose transporter genes during SBR pathogenesis. These may unravel molecular mechanisms regarding sucrose export out of source tissues to receiving sink tissues and may present novel opportunities towards improving crop performance (Braun et al., 2014; Chen et al., 2010; Reyer et al., 2024).

CHAPTER 3

In vivo quantification of temporal transport velocities and storage of photoassimilates within sugar beet taproot by tomographic imaging.

3 In vivo quantification of temporal transport velocities and storage of photoassimilates within sugar beet taproot by tomographic imaging

3.1 Background

This chapter harnesses the quantitative 3D datasets generated by ^{11}C labelling and tomographic imaging as described in **Chapter 2** to determine temporal dynamics in tracer transport properties within the sugar beet taproots. A member of the Bühler family of compartmental models, model M02, which includes flow velocity and storage parameters (Bühler et al., 2014), was used to determine tracer transport properties within sugar beet taproot. The analysis was performed in different parts of the sugar beet taproot separated along the vertical or radial axis. Within this framework, the current chapter addressed these questions:

- Do phloem sap transport velocities and rate of storage vary during early stages development of the taproot?
- Does transport velocities and storage differ for different vertical or radial zones of the sugar beet taproot?
- How does SBR disease affect phloem sap transport velocities within sugar beet taproot?

3.2 Materials and Methods

3.2.1 Plant material and data acquisition

As mentioned above, the data set analyzed in this chapter was obtained from the experiments in **Chapter 2**. Details of growth conditions, treatment application and imaging protocols are presented in **Chapter 2**. Unlike in **Chapter 2**, scatter and attenuation corrections (Hinz et al., 2024) were employed to the PET data set analyzed in this chapter. Steps and processes encompassing imaging and analysis are shown in Fig. 3.1.

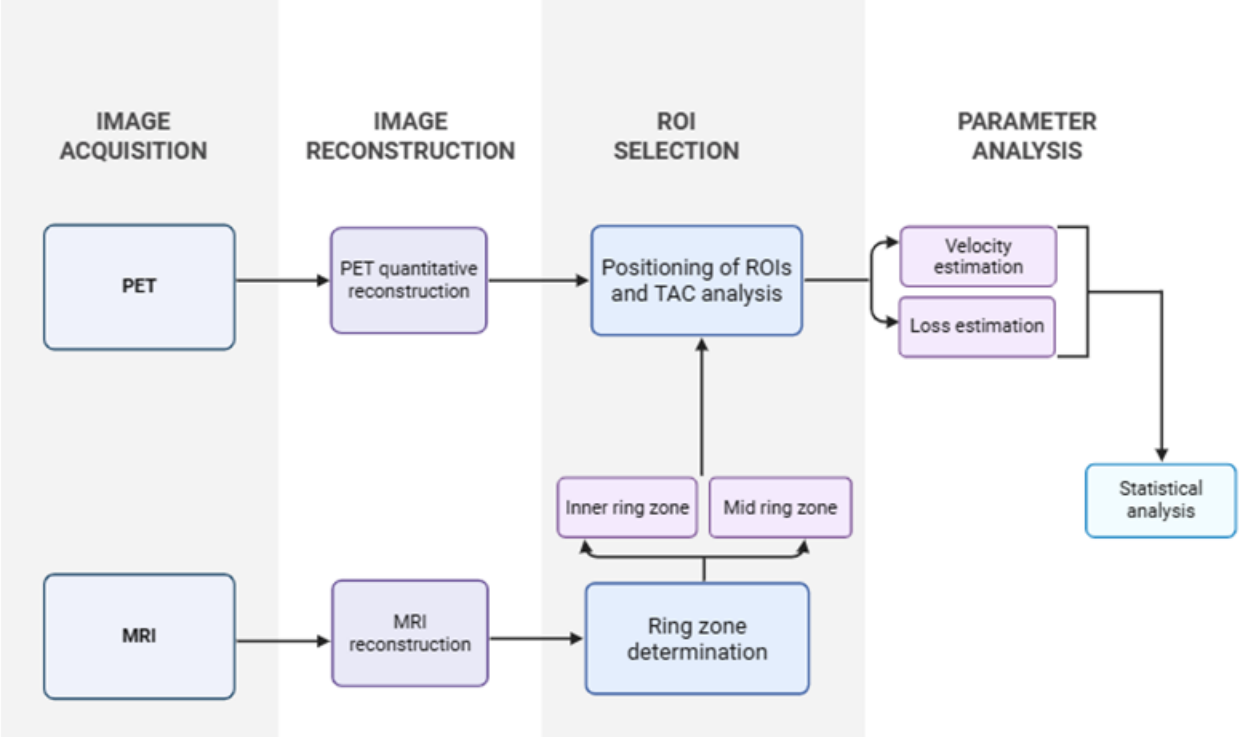

Figure 3.1. Overview of MRI and PET imaging and analysis pipeline. After PET reconstruction, regions of interest (ROIs) were positioned along the vertical axis of the taproot to generate time activity curves (TACs). For vertical sectioning analysis ROIs were positioned directly around the whole girth of the taproot (see Fig. 3.2 and Supplementary Fig. B. S1). For radial zones analysis, ROIs were separated into inner and mid ring zones. The position of these zones was determined based on cross-sectional rings radius obtained by MRI. Based on TACs generated from ROIs, a compartmental model for long-distance tracer transport in plants (M02; Bühler et al., 2014) was used to analyze transport velocities and rates of storage.

3.2.2 Estimating tracer transport velocity and storage in sugar beet taproot.

To determine tracer transport velocity and storage in sugar beet taproot, ROIs were positioned along the vertical axis of the taproot within MeVisLab software (version 3.6.1, MeVis Medical Solutions AG, Bremen, Germany) according to Jahnke et al. (2009) with some improvements to aid adjustments of ROIs to suit taproot geometry (Fig 3.2). Custom-built MeVisLab scripts provided a longitudinal 2D views of opposite sides of the sugar beet taproot geometry. From this 2D views, the ROIs for each measured taproot were defined (Fig. 3.2). Number, height and radius of the ROIs were set to suit the taproot geometry

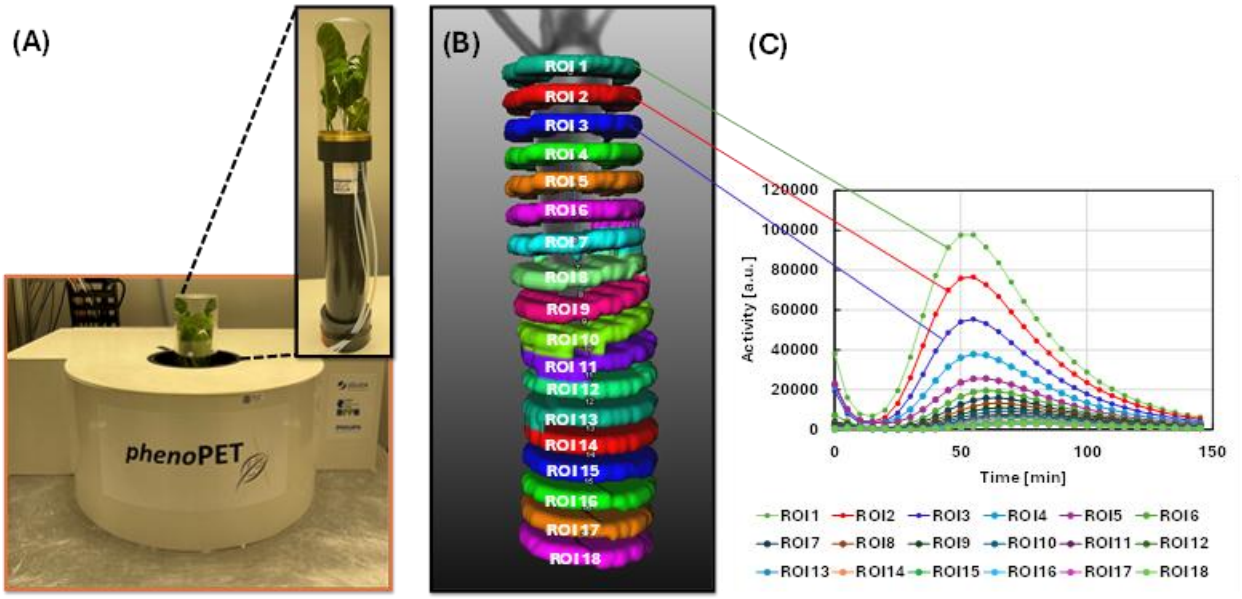

Figure 3.2. Set-up for sugar beet PET imaging and time activity curves acquisition. (A) Sugar beet plant growing in soil-filled pot with the whole shoot enclosed in a cuvette, mounted in *pheno*PET for $^{11}CO_2$ administration and PET imaging. (B) Reconstructed PET image of sugar beet taproot with ROIs positioned along the vertical axis of the PET signal in the sugar beet taproot. (C) Time activity curves generated from ROIs in B. Examples of corresponding ROIs to TACs are shown by lines connecting B and C. ROIs were manually positioned to analyze 3D PET data with MeVisLab software. Parameters used for ROIs are listed in Supplementary Table B S1-3.

(Supplementary Table B. S1-3). As shown in Fig. 3.2C, the tracer activity inside each ROI was integrated over defined time intervals of 5 min, resulting in a time activity curve (TAC) (Lanzrath et al., 2025). Tracer transport velocity and rate of tracer storage were estimated using the model-based analysis of Bühler et al. (2014). Out of the class of compartmental models described by Bühler et al. (2014) for long-distance tracer transport in plants, the simple model M02 was chosen because it is sufficient to describe tracer transport with a strong storage component (Lanzrath et al., 2025) as expected in sugar beet. The model fits TACs of all selected ROI simultaneously to estimate tracer transport velocity and rate of storage. Prior to application of model M02 to the TAC data for tracer transport velocity analysis, a preliminary analysis was performed with the half maximum approach. The half maximum method utilizes the times at which TAC curves reach half-height of their maximum as reference time points for each ROI. From these reference time points and the known distances between ROIs, the tracer flow velocity was calculated as the slope of a linear fit. (Lanzrath et al., 2025).

3.3 Results

3.3.1 Differences of transport velocity along vertical transport pathway within sugar beet taproot

A preliminary analysis of transport velocities was performed with the half maximum approach prior to the application of the compartmental model fitting to the TAC data. When fitting a single linear regression to all the ROIs for each taproot sample, the residuals were relatively large and there was a systemic deviation from the fit line (see example in Fig. 3.3), indicating that the single linear model did not optimally represent transport velocity along the vertical axis of the taproot through all of the ROIs. Instead, different slopes of the data points were apparent between the ROIs in the upper and the lower part of the taproot, suggesting that tracer flow velocity dynamics varied along the vertical axis of the taproot (Fig. 3.3). To account for this, the taproot was divided into upper and lower sections and fitted with separate linear models for each section. Depending on the geometry of the taproot, grouping the first 7 or 8 ROIs (i.e. upper section) and the 8th or 9th to last ROIs (i.e. lower section) yielded an improved model fit with considerably reduced residuals (see Supplementary Table B S3 for the total number of ROIs per taproot sample).

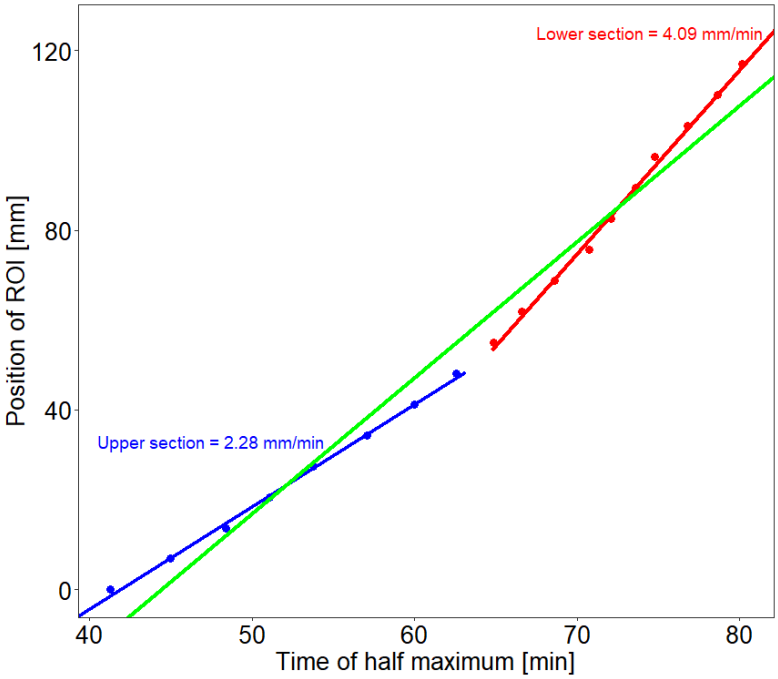

Figure. 3.3. An example of linear regression of distance and time to determine tracer flow velocity in sugar beet taproot, based on reference time points obtained with the half maximum method for each region of interest (ROI). The green line represents the regression fitted to the full dataset, showing larger residuals. The blue and red lines represent separate regressions for the upper and lower sections of the taproot, respectively, showing reduced residuals and better fit, highlighting differences in tracer transport dynamics between sections.

The analysis of transport velocity using the compartmental model M02 was based on the same grouping into upper and lower sections as identified before with the half maximum method. The estimated flow velocities of tracer ranged between 1.4 and 15.2 mm/min. Transport velocities were higher in lower

sections than in upper sections. Transport velocity was highest at around 49 to 54 days after planting (DAP) and decreased substantially until 84 DAP (Fig. 3.4). This was obvious for all measured samples except in a few instances where velocity was constant for the last two imaging days (i.e. 77 and 84 DAP) or increased slightly for the last imaging day (i.e. 84 DAP). When first and last (i.e. 49 and 84 DAP) measurements were compared, a substantial reduction in transport velocity of approximately 66 and 50 % was observed for lower and upper sections, respectively.

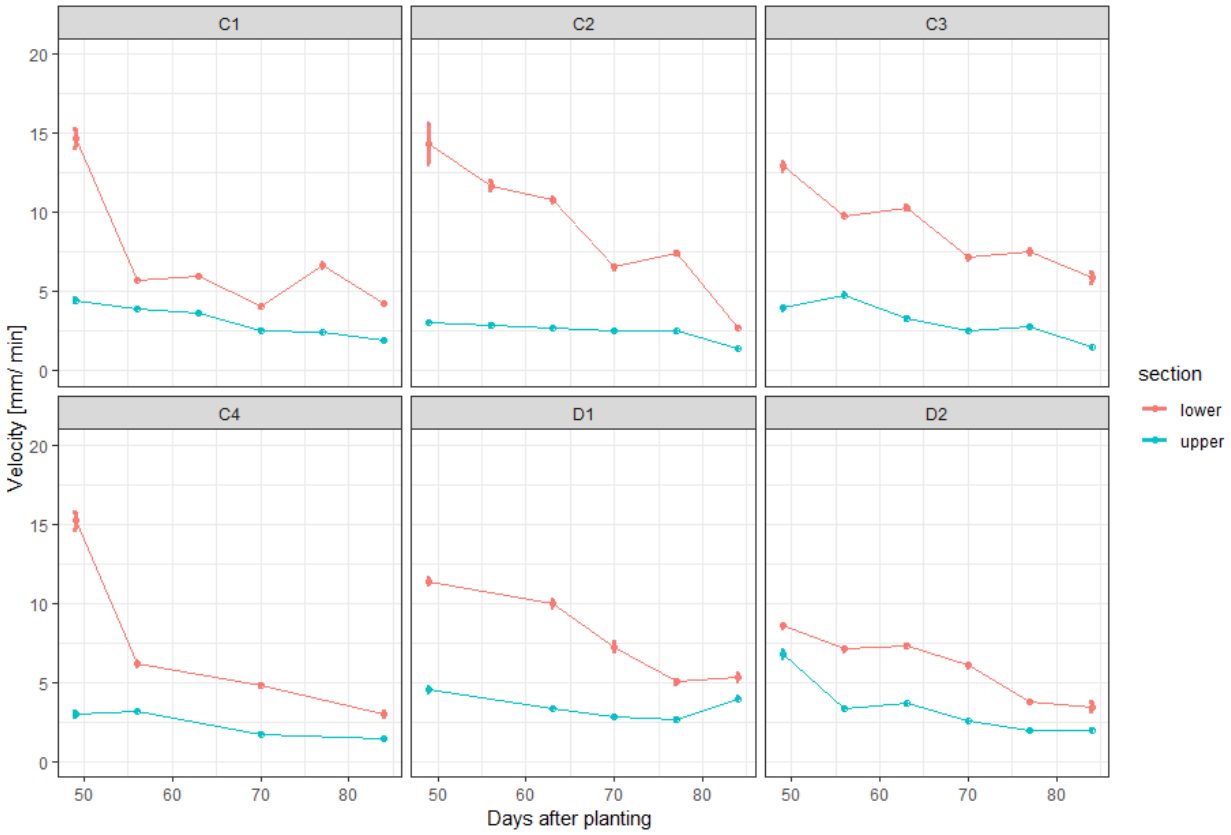

Figure 3.4. Tracer transport velocities over taproot development, separated between upper and lower parts of taproots. Each facet represents dynamics in an individual sugar beet taproot sample, i.e., control samples C1-C4 and diseased D1-D2, see chapter 2. Each point represents tracer transport velocity and standard errors estimated with model M02 of the Bühler model family from selected TACs; for some points the error bars are tiny and not visible. Red and green dots and lines represent lower and upper sections of ROIs, respectively.

3.3.2 Differences of transport velocity between radial zones of sugar beet taproot

A possible explanation for the high transport velocity in the lower section of the taproot could be that the velocity is highest in the central core which forms the main part of the lower section. To test this

hypothesis, a radial zone analysis was performed. The taproot was partitioned into two zones: an inner zone, comprising the area covered by the central core until the 2nd cambial ring, and a mid zone, comprising the area covering from the 2nd until the 4th ring (Fig. 3.5A). The ROIs for radial zone analysis were restricted to a 4 cm portion of the taproot beginning from directly below the pith (mostly thickest part of the taproot, depicted by green rectangle in Fig. 3.5B). Exact positions of the ROIs varied over the development of the taproots and from sample to sample due to heterogeneities in taproot geometry. To obtain accurate radii of the ROIs for the radial zones analysis, the diameter of each ROI was determined based on cross-sectional cambium rings anatomical features obtained by MRI (Fig. 3.5). The data obtained (i.e., detector radius as listed in Supplementary Table B. 1-2) was used as a guide to define the ROIs to generate TACs. Leading or trailing TACs were not included in the analysis if the signal was very noisy or incompatible with the model. Remaining TACs were analyzed by using model M02 of the Bühler model family. Diseased samples D1-2 (see Fig. 2.6 and Supplementary Fig. A. S3) could not be analyzed, because the tracer signal was not distributed homogenously among the radial sections.

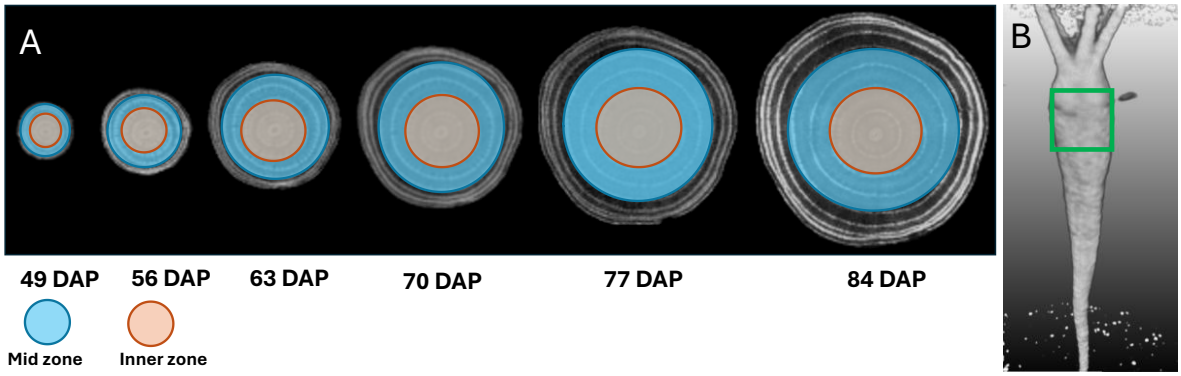

Figure 3.5. Schematic of radial partitioning analysis. (A) Inner and mid zone partitioning as overlays on 2D cross-section from MRI of a developing sugar beet taproot and (B) an example of PET image of sugar beet taproot indicating portion of the PET signal in the sugar beet taproot (marked in green shape) considered for radial sectioning analysis. DAP = days after planting.

The estimated flow velocity ranged between 1.4 and 8.1 mm/min for all measured samples. Comparatively, flow velocities for the inner zone were higher than in the mid zone of the taproot (Fig. 3.6). The temporal pattern and values recorded were similar to the vertical analysis, except that in some samples (C2-C4; Fig. 3.6), an initial increase in velocity was observed at 56 DAP. Again, a reduction in transport velocity as the sugar beet taproot developed was observed. There was an average reduction of approximately 60% in the inner zones and 49% in the lower sections when the initial and final measurements were compared.

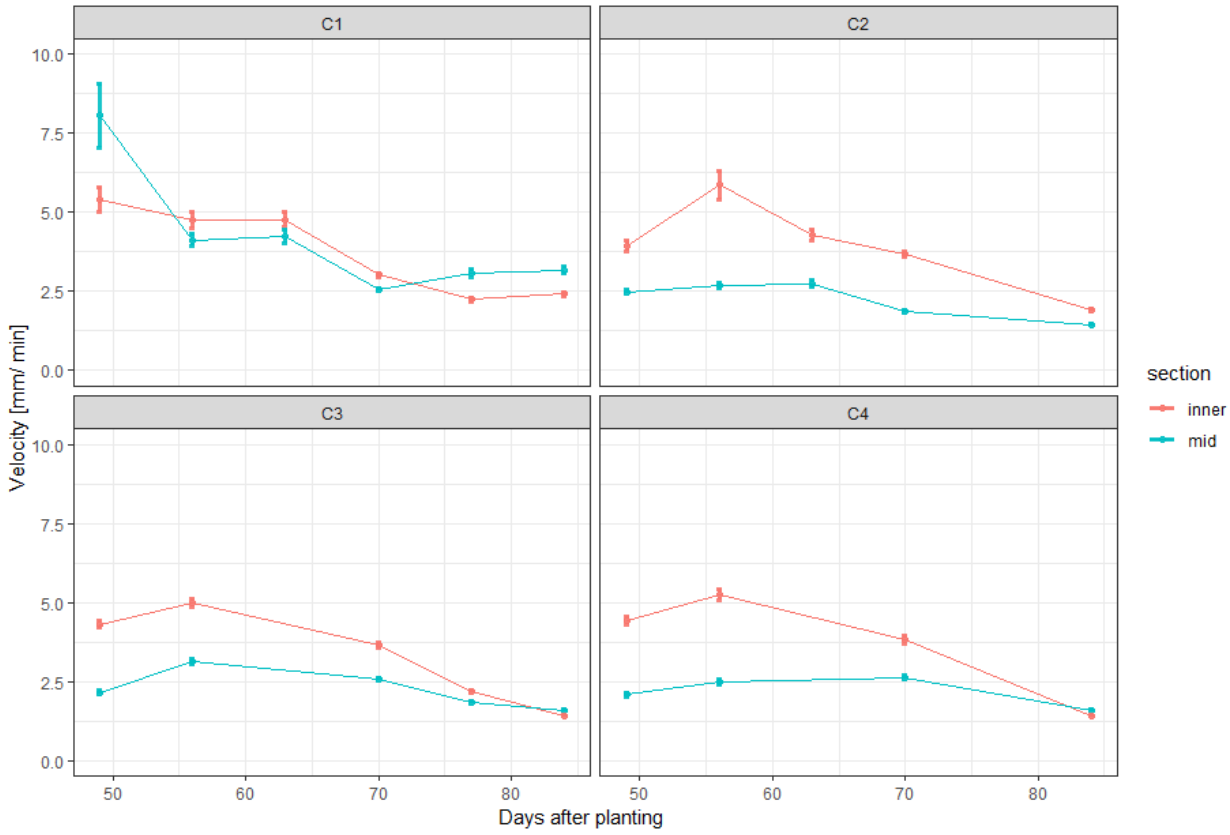

Figure 3.6. Tracer transport velocities over taproot development, separated between radial inner and mid zones of taproots. Each facet represents dynamics in an individual measured sugar beet taproot sample, i.e., control samples C1-C4. Diseased samples D1-D2 could not be analyzed. Each point represents tracer transport velocity and standard errors estimated with model M02 of the Bühler model family from selected TACs; for some points the error bars are tiny and not visible. Red and blue dots and lines represent inner and mid zones, respectively.

3.3.3 Tracer transport velocity in SBR diseased sugar beet taproot

Because radial zone analysis was not possible in diseased samples, the effect of SBR disease on tracer transport velocity could be evaluated only with the vertical sectioning analysis. In both the upper and lower sections, transport velocities in diseased samples were comparable to those in controls. As in control samples, tracer movement within the taproot of diseased plants slowed as the taproot developed (Fig. 3.7).

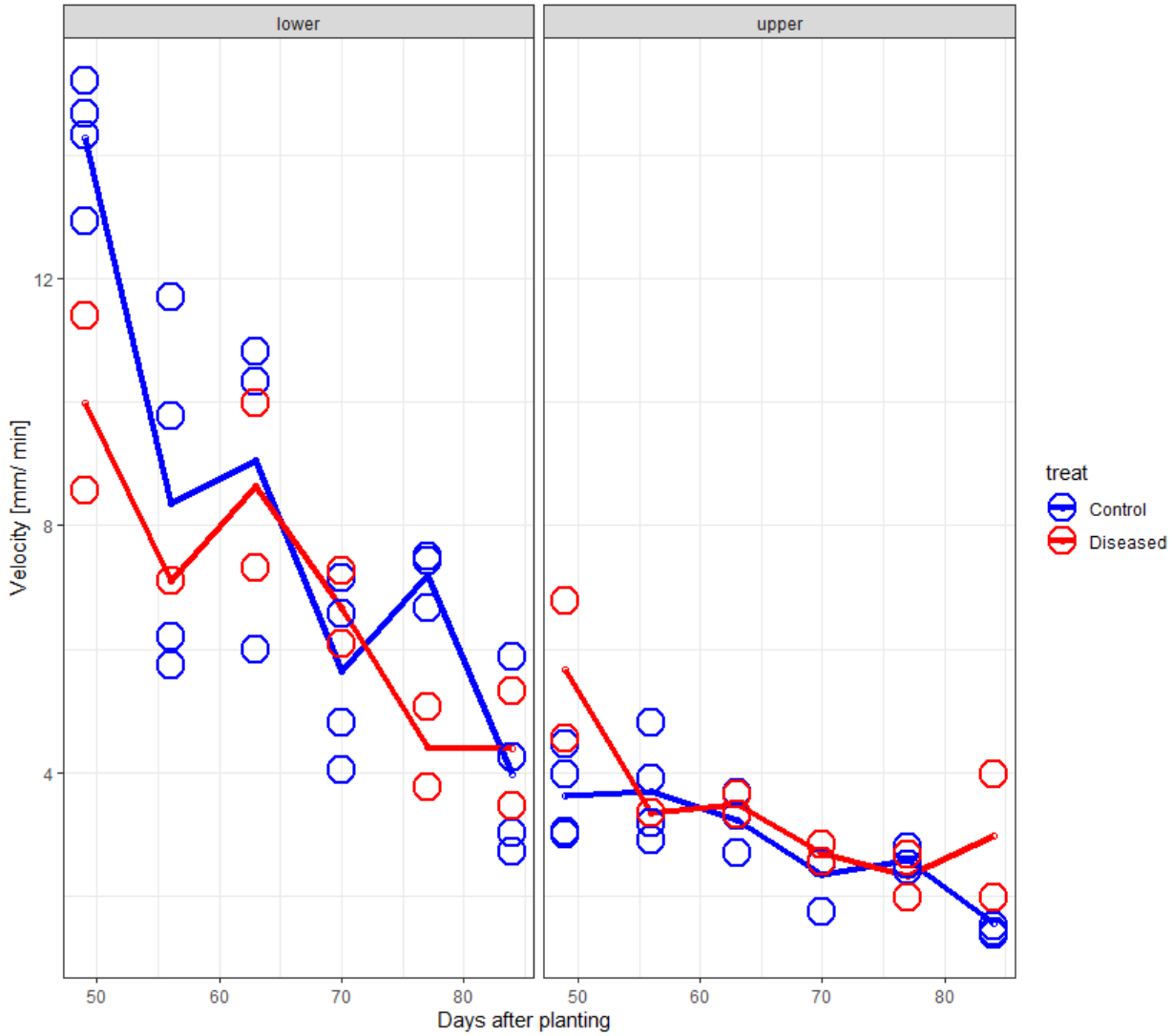

Figure 3.7. Comparison of dynamics in tracer transport velocity for control and diseased taproot samples. Facets represent lower and upper sections for control (blue) and diseased (red) samples. Circles represent values per taproot section and lines represent their means. n = 4 for control at 56, 70 and 84 DAP; n = 3 for control at 63 and 77 DAP; n = 2 for diseased at 63, 70, 77 and 84 DAP; n = 1 for diseased at 56 DAP. The data shown here are the same data presented in Fig.4 but sorted according to treatment.

3.3.4 Temporal rate of storage of photoassimilates within the sugar beet taproot

The loss of tracer as it travelled along the vertical axis of the sugar beet taproot represents the storage rate and was estimated from the TACs using compartmental model M02. Tracer loss was estimated solely in radial sectioning analysis. This is because ROIs positioning for vertical sectioning analysis captured part of the tracer signal in soil, which could result in biased estimations. This was avoided in the radial zones analysis, which excluded the outer part of the taproot (Fig. 3.5). Estimates of tracer storage ranged

between 3 and 35 % per cm for all measured samples and throughout the experimental period. There was no clear trend in the variation of tracer storage as the taproot developed (Fig. 6.8) and there was also no systematic difference between tracer storage for inner and mid zone of the taproots (Fig. 6.8).

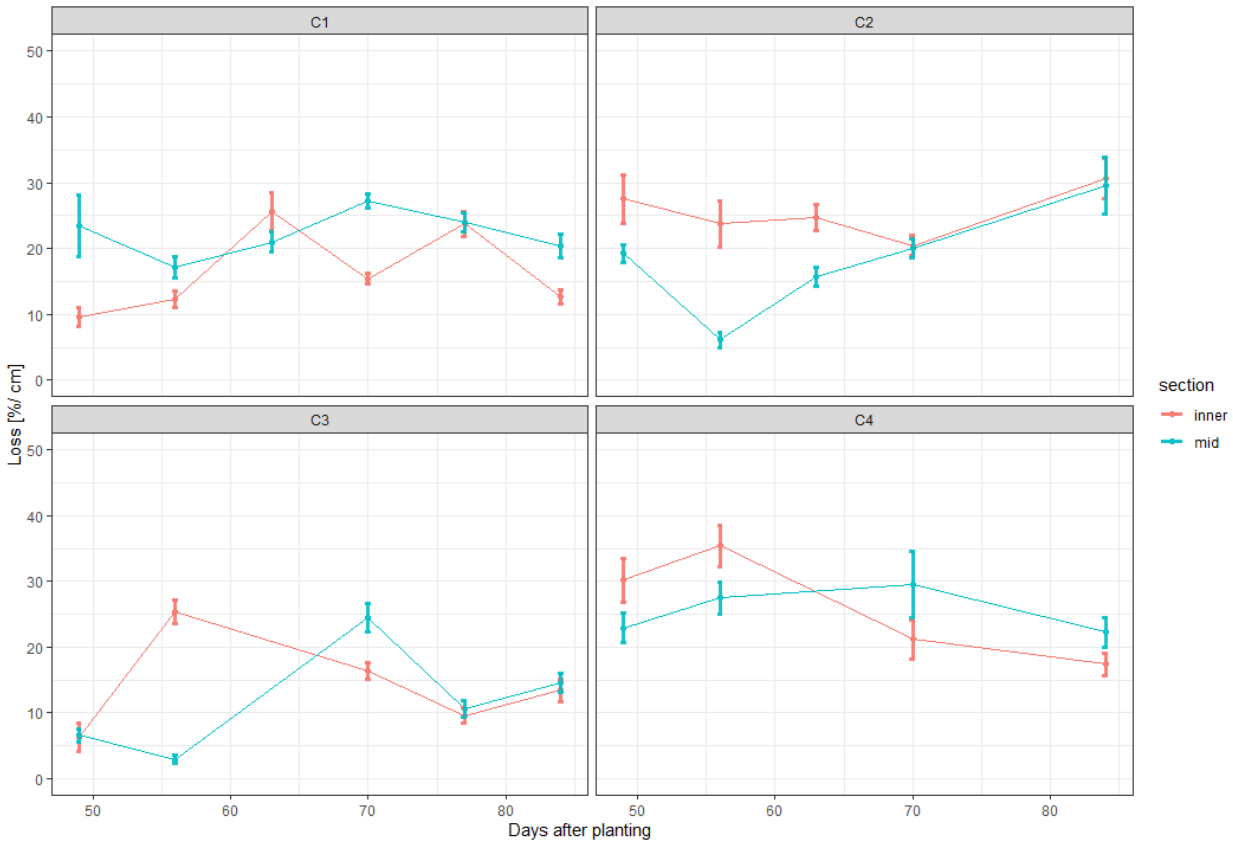

Figure 3.8. Tracer storage over taproot development for control samples C1-C4. Each facet represents dynamics in an individual measured sugar beet taproot sample. Each point represents the loss percentage and standard errors estimated with model M02 of the Bühler model family from selected TACs. Diseased samples D1-D2 could not be analyzed. Red and green dots and lines represent the inner and mid zones, respectively.

3.3.5 Temporal assimilation rates for the developing sugar beet

As indicated in subsection 2.2.6 of **Chapter 2**, the gas exchange system embedded in *pheno*PET enabled gas exchange measurements during each PET imaging. Assimilation rates were measured for the entire shoot enclosed in cuvette; therefore, the reported values represent whole shoot assimilation rates (µmol s^{-1}) rather than normalized area-based assimilation rates (µmol m^{-2} s^{-1}). Assimilation rates were logged every 5 min during the PET imaging period, with each value representing the integrated rate over that interval. The data obtained was averaged for each measurement (Fig. 3.9). The mean assimilation rates

ranged from 0.04 and 0.14 µmol/shoot. No clear trend was observed for assimilation rates for the developing plants at early stages (specifically from 49 to 70 DAP). A slight increase or decrease in assimilation rate was observed for different sampling dates, and there was some variation in assimilation rate from sample to sample. Overall, assimilation rates tended to decline in the second half of the measurement period (Fig. 3.9).

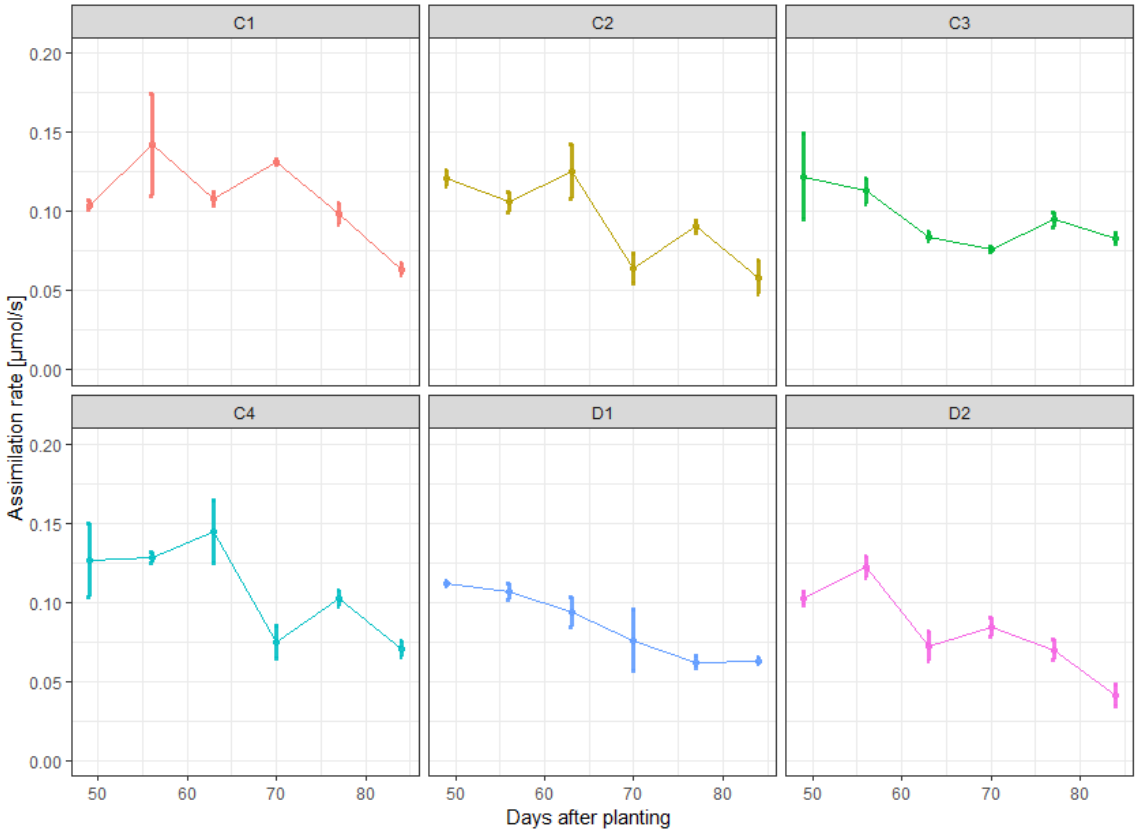

Figure 3.9. Assimilation rates for each plant sample during PET acquisition. Assimilation rates were logged every 5 min during the period of PET acquisition period, with each value representing the integrated rate over that interval. The data presented here is the mean of integral assimilation rates. Error bars represent standard deviation.

3.4 Discussion

This chapter estimated transport velocities and rates of storage of recently fixed photoassimilates within sugar beet taproot, based on PET quantitative data obtained by repeated ^{11}C labelling during early stages of sugar beet taproot development. To determine temporal and spatial differences in flow velocities, analysis was based on vertical sections or radial zones of the taproot. Within these configurations,

differences in transport velocities among vertical sections or radial zones and for the developing taproot were identified. For the rate of storage of recently fixed photoassimilates, no clear trend was identified. Moreover, as a buildup to **Chapter 2**, this current chapter tested whether SBR disease influences tracer transport velocity along the axial transport pathway of sugar beet taproot growing in natural soils. From the model results, the presence of SBR disease did not affect transport velocity. The effect of SBR disease on the storage rate could not be tested due to high noise-to-signal ratio in radial zones analysis.

3.4.1 PET data acquisition and extraction from regions of interest: current improvements

The data analysed in this chapter were obtained from the vertically oriented plant dedicated PET platform "pheno*PET*" (Hinz et al., 2024); hence potential gravitropic effects resulting from employing horizontally oriented commercial PET systems such as that of Karve et al. (2015), were avoided entirely. Unlike previous measurements by Jahnke et al. (2009) with "PlanTIS" PET system (Beer et al., 2010), the current pheno*PET* set-up incorporates the possibility for transmission scans of individual plants to correct the effects of attenuation and scattering (Hinz et al., 2024). As stated by Karve et al. (2015), individual transmission scans of belowground crop organs improve the accuracy of PET quantitative data. Based on this it can be assumed that employing scatter and attenuation corrections improved the quantitative accuracy of the data presented in this chapter.

The variable geometry along the vertical axis of the sugar beet taproot complicates the placement of ROIs for TAC analysis. Previously, the TAC analysis tool assumed the taproot as a straight structure, with ROIs aligned along the vertical axis of the sugar beet taproot (Jahnke et al., 2009). In that case, when the shape of the taproot varied along the vertical axis, ROIs could be mispositioned, capturing a greater volume of soil instead of the taproot. Also, a curvature in the taproot geometry, when not properly tracked, will lead to underestimating the length of the transport pathway. The current improvement in TAC analysis (Schmidt et al., 2024) offers a flexibility in the positioning of ROIs along the taproot based on the geometry and orientation of the taproot. This limits the risk of mispositioning of the ROIs.

3.4.2 Dynamics in tracer transport properties within different sections: upper vs lower sections; inner vs mid taproot zones

Transport velocities ranged between 1.4 to 15.2 and 1.4 to 8.1 mm/min for vertical section and radial zones analysis, respectively. It is common to have such a wide range for transport velocities, depending on plant species, specific organ (Karve et al., 2015; Schepper et al., 2013; Windt et al., 2006), or whether a stressor has been imposed (Schepper et al., 2013). The relatively broader range recorded in vertical section

analysis compared to radial zones analysis suggests that transport velocities vary more along the vertical axis of the taproot than radially. This variation may reflect axial heterogeneity in tissue properties or flow pathways. Moreover, velocity estimates for the upper section in vertical sectioning analysis were within the range of the estimates in radial sectioning analysis. This was expected since the portion of the taproot considered for radial sectioning analysis were restricted to upper 4 cm of the taproot (Fig. 3.5B) and were close to same position as the upper section. Velocity estimates at 84 DAP were comparable to the estimate of 1.24 mm/min obtained by Bühler et al. (2014) for sugar beet taproot similar in size as those measured at 84 DAP in this study. For vertical analysis, transport velocities were slower in upper taproot sections than in lower taproot sections. Compared to the lower section, the upper section encompassed the thickest portion of the sugar beet taproot. The lower apparent transport velocities observed in the upper section likely coincide with regions of intense phloem unloading. Although unloading itself does not directly reduce the modeled transport velocity, strong unloading may have masked tracer exchange out of and back into the translocation stream. Consequently, intense unloading may contribute indirectly to an apparent slowing of transport in this region.

As depicted in Fig. 3.10, radial sectioning analysis revealed that transport velocities were slower in the mid zone compared to the inner zone. Likewise, the upper section, the mid zone may be a zone characterized with intense exchange processes than in the inner zone. Owing to this, it is proposed that slower velocities in the mid zone are likely due to tracer exchange out of and back into the transport pathway, thereby slowing down the transport.

It was expected that the speed at the inner zone will be same as the lower section since the inner zone and lower section comprise the central core and up to two inner rings (Fig. 3.9). Even though there was a tendency of faster velocities in the inner zone like that of the lower section, this was not sufficient. Froelich et al. (2011), indicated that agglomerates can fill significant portions of the phloem tube diameter at, or close to, the sieve plate, thereby reducing the sieve element cross-sectional area. Considering the sieve tube in a very simplified way as a cylindrical pathway, a reduction in phloem cross-sectional area by agglomeration will lead to an increased pressure differential, thereby increasing phloem sap flow velocity (Froelich et al., 2011; Jensen et al., 2011). Thus, a plausible explanation of the higher transport velocities in the lower part of the taproot would be that the phloem area decreases along the vertical axis of the taproot. Whether agglomeration (e.g. P protein agglomerates) occurs and vary among the sections and zones defined in this study, and for the developing taproot should be tested.

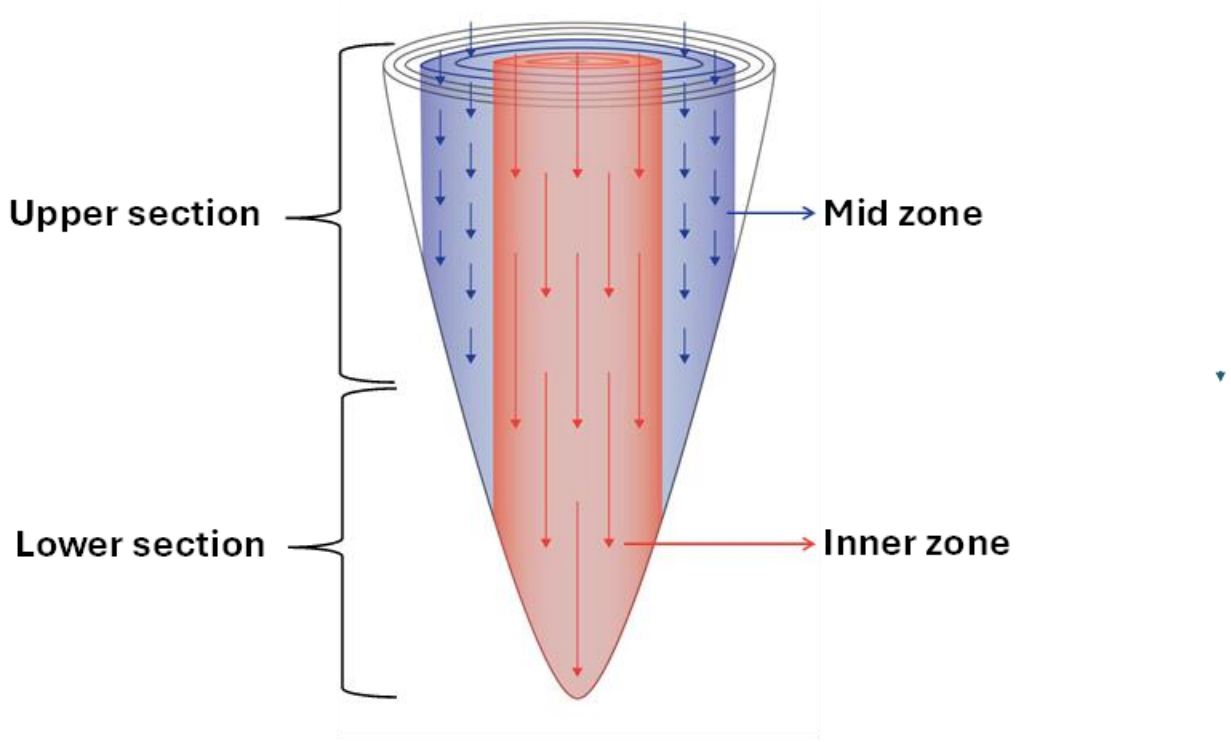

Figure. 3.10. Sketch depicting differences in transport velocities among different taproot zones and sections. The defined inner zone comprises an area encompassing the central core and two innermost rings (marked in orange color). Mid zone includes the area covered by third to fourth cambium rings (marked in blue color). Arrow length depicts the speed at which phloem sap travels along the axial pathway of the taproot (Long = fast, Short = slow). Even though transport velocities were not determined at the taproot periphery, assumptions point to very slow transport velocities at these sections.

In both analyses, transport velocities decreased as the taproot developed. The early stages of sugar beet taproot development have been categorized into three distinctive phases (Jammer et al., 2020; Zhang et al., 2017), namely prestorage, transition and sucrose storage stages (Jammer et al., 2020) or initial, transition and rapid growth stages (Zhang et al., 2017). Sucrose-metabolic enzyme activities, sucrose storage and growth rate become dominant after 60 days (Jammer et al., 2020; Zhang et al., 2017). The trend of reduced transport velocities could be linked to the growth stage of dominant sucrose accumulation in sugar beet taproots, as the decline in transport velocities was evident at 60 DAP for most samples. Also the systematic differences in tracer transport velocities observed among different sections in this study can be linked to the assumption made by Jammer et al. (2020) that sucrose-metabolic enzymes distribution within sugar beet taproot is non-homogenous and may depend on location or cell type.

Lateral exchange and redistribution of photoassimilates is likely to be prominent as the taproot develops, which can increase the axial transport resistance and, in turn, cause a slower phloem pathway (Schepper et al., 2013). In both vertical sectioning and radial zones analysis velocities were lowest at the last measurement time point at 84 d for most of the samples. It is likely that transport speed could stabilize as the taproot developed further. This would be in accordance with the speculation that the phloem is regulated to maintain a constant and relatively slow flow of sap (Windt et al., 2006). Further investigation will be required to confirm if phloem sap flow velocity stabilizes as the taproot continues to develop.

Given that secondary growth and sucrose storage are dominating activities after 60 days (Jammer et al., 2020) and that stronger than linear increase in sizes over time was observed (Fig. 2.4A; Metzner et al., 2014; Schmittgen et al., 2015; Trebbi & McGrath, 2009), it was expected that the rate of storage of photoassimilates would increase for the developing taproot from 60 until 84 DAP. An increase in tracer storage would have confirmed the suggested tradeoff between secondary thickening and transport speed. However, there was no clear pattern of increase in the rate of storage as the taproot developed and transitioned through different stages and hence, the suggested tradeoff cannot be confirmed from the present measurements. It doesn't seem easy to estimate the storage rate in plant organs. Storage rate estimates have shown high variability and inconsistency in a previous study, making it challenging to draw a definite conclusion based on such data (Schepper et al., 2013). In contrast, Karve et al. (2015) reported a clear pattern of change in the percentage of photoassimilates allocated from source leaf to different organs of sorghum during different stages of development. The observed varied allocation pattern by Karve et al. (2015) is likely due to PET sampling being conducted at two very distinct phases of sorghum development, i.e. vegetive and reproductive stages when plants were 40 and 70 days old respectively. Therefore, the detailed and complex temporal dynamics may not have been fully captured in the study by Karve et al. (2015).

In general, CO_2 assimilation rates tended to decrease at the later stages of the experiment. Even though higher CO_2 assimilation rates have been linked to a higher bulk flow velocity (Zierer et al., 2025). Unlike in the study of Zierer et al. (2025) where assimilation rates were normalized by leaf area, in this study assimilation rates were not normalized by leaf area, and hence difficult to conclude whether assimilation rates had effects on loading, transport and rate of storage of recently fixed photoassimilates.

3.4.3 SBR disease effects on tracer transport dynamics and model analysis

In **Chapter 2** (see Fig. 2.6), a non-homogeneous distribution of photoassimilates within the taproot was reported in the presence of SBR disease. To gain deeper understanding of how SBR manipulates the

phloem sap, this chapter aimed to determine the effects of SBR disease on transport velocity. Based on the model results, no marked differences were observed in transport velocity for SBR diseased and control samples. This is likely due to the localized effects of SBR pathogen within some specific sectors of the taproot (see Figs. 2.3 and 2.6), hence the unaffected sectors maintained phloem sap flow velocity. The low or missing PET signal upon SBR disease, especially in the inner zone of the taproot (see Fig. 2.6) leads to a low-signal-to-noise ratio, thereby increasing error levels during model application for TACs obtained by radial zones analysis. Therefore, flow velocity based on radial zones could not be reliably estimated for SBR diseased samples.

CHAPTER 4

Effects of partial defoliation and partial shading on photoassimilates distribution in sugar beet taproot.

4 Effects of partial defoliation and partial shading on photoassimilates distribution in sugar beet taproot

4.1 Background

By repeated $^{11}CO_2$ labelling and PET imaging complimented with MR imaging, this chapter investigated how shoot architecture and experimental manipulations, through partial defoliation or shading of a single leaf of the sugar beet shoot, influence the dynamics of photoassimilates distribution within the taproot. The chapter addresses the following questions:

- How does a mature single-source leaf distribute its photoassimilate resource within the taproot sink?
- Assuming recently fixed photoassimilates resources are redistributed during partial shading or defoliation: how fast does the redistribution occur?
- Does partial defoliation and partial shading induce different responses with respect to the distribution pattern of recently fixed photoassimilates?

Despite extensive research on how shoot manipulations affect the distribution of both recent and non-recent photoassimilates (Ferrieri et al., 2013; Joy, 1964; Schmitt et al., 2013; Schwachtje et al., 2006), the effect of shading on the distribution dynamics of recently fixed photoassimilates in plants has not been reported so far. In particular, no in vivo studies have examined the temporal dynamics of photoassimilate allocation to belowground storage organs under conditions of partial defoliation or shading. This information is relevant for further interpretation of the observations made in **Chapter 2** (i.e. whether the observed sectoral distribution upon SBR is source or sink driven). Based on the findings by Schmitt et al. (2013) (see **Chapter 1**; section 1.4 for details), it is assumed that partial defoliation and partial shading will induce distinct short-term allocation patterns of photoassimilates.

4.2 Materials and Methods

4.2.1 Plant materials used

Sugar beet (*Beta vulgaris*) genotype BTS 8750 (Betaseed GmbH, Frankfurt, Germany) was cultivated for 63 days in the same soil and under the same climate conditions described in chapter 2 (Sections 2.2.2 and 2.2.3). Except that in this experiment, plants were cultivated exclusively under climate chamber conditions at FZJ as described in chapter 2 (Section 2.2.3).

4.2.2 PET and MRI acquisition routines

PET measurements were performed for four different samples of a 63-day-old sugar beet plant. Three plants were dedicated to partial defoliation experiments, and one plant to a partial shading experiment (details of both manipulations are highlighted in sections 4.2.4 and 4.2.5). For each plant sample, either the whole shoot or one single (fully expanded) leaf was labelled with $^{11}CO_2$ (Fig. 4.1) and the belowground taproot was imaged with *pheno*PET. Single leaf labelling (SLL) was performed by confining a fully expanded leaf of an intact plant in a leaf labelling cuvette (Fig. 4.1D). During the SLL process, a plastic zip was placed at the petiole base to mark the architectural position of the labelled leaf. This allowed consistent identification of the leaf's position relative to the taproot. For whole shoot labelling (WSL, Fig. 4.1C), the whole shoot of either an intact plant or experimentally manipulated plant (either by excising or shading a single leaf) was confined in a shoot cuvette. Models and dimensions of the cuvettes used for administering $^{11}CO_2$ are shown in Fig. 4.1. PET acquisition was performed for a period of 150 min per measurement. Assimilation rates were logged every 5 min during the PET imaging period, with each value representing the integrated rate over that interval. PET imaging was performed in the morning, midday and afternoon on four consecutive days on the same plant (Fig. 4.2). MR image was obtained once for each taproot sample before or after the last PET imaging for partial defoliation and partial shading manipulation experiments, respectively (Fig. 4.2). The details of the sequence for MRI and PET imaging for each manipulation experiment are presented in Fig. 2. Details of PET and MRI protocols used in this study have been described in **Chapter 2** (sections 2.2.3 until 2.2.6).

4.2.3 MRI and PET image analysis

Reconstructed MRI and PET images were analyzed using MeVisLab software (version 3.6.1, MeVis Medical Solutions AG, Bremen, Germany). Similar to **Chapter 2**, scatter and attenuation were not employed during PET reconstruction. All PET images were co-registered with corresponding MR images. MRI-PET analysis was based on maximum and intra-measurement intensity PET projections. MRI-PET cross-sections of sugar beet taproot presented in the results section of this chapter are sections of the taproot directly below the pith. This section was selected due to its clearly defined anatomical structures, coupled with good PET signal, especially for intra-measurement projection analysis.

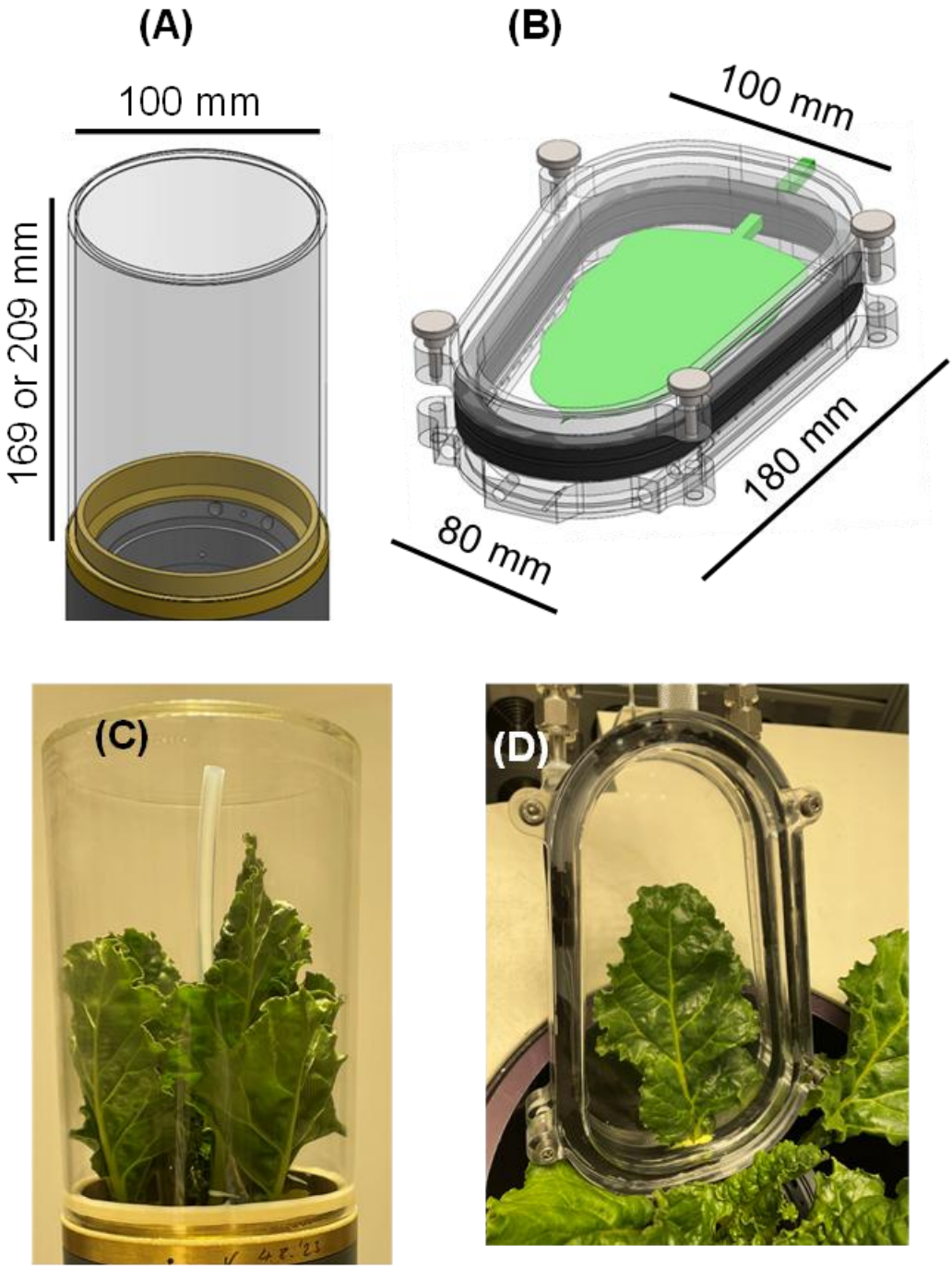

Figure 4.1. Models of $^{11}CO_2$ labelling cuvettes and examples of whole shoot or single leaf of sugar beet plants enclosed in $^{11}CO_2$ labelling cuvettes. (A) Whole shoot labelling (WSL) cuvette, (B) Single leaf labelling (SLL) cuvette, (C) whole shoot of sugar beet plant enclosed in WSL cuvette and (D) single leaf of sugar beet plant enclosed in SLL cuvette. The dimensions shown in (A) and (B) indicate the interior cuvette sizes.

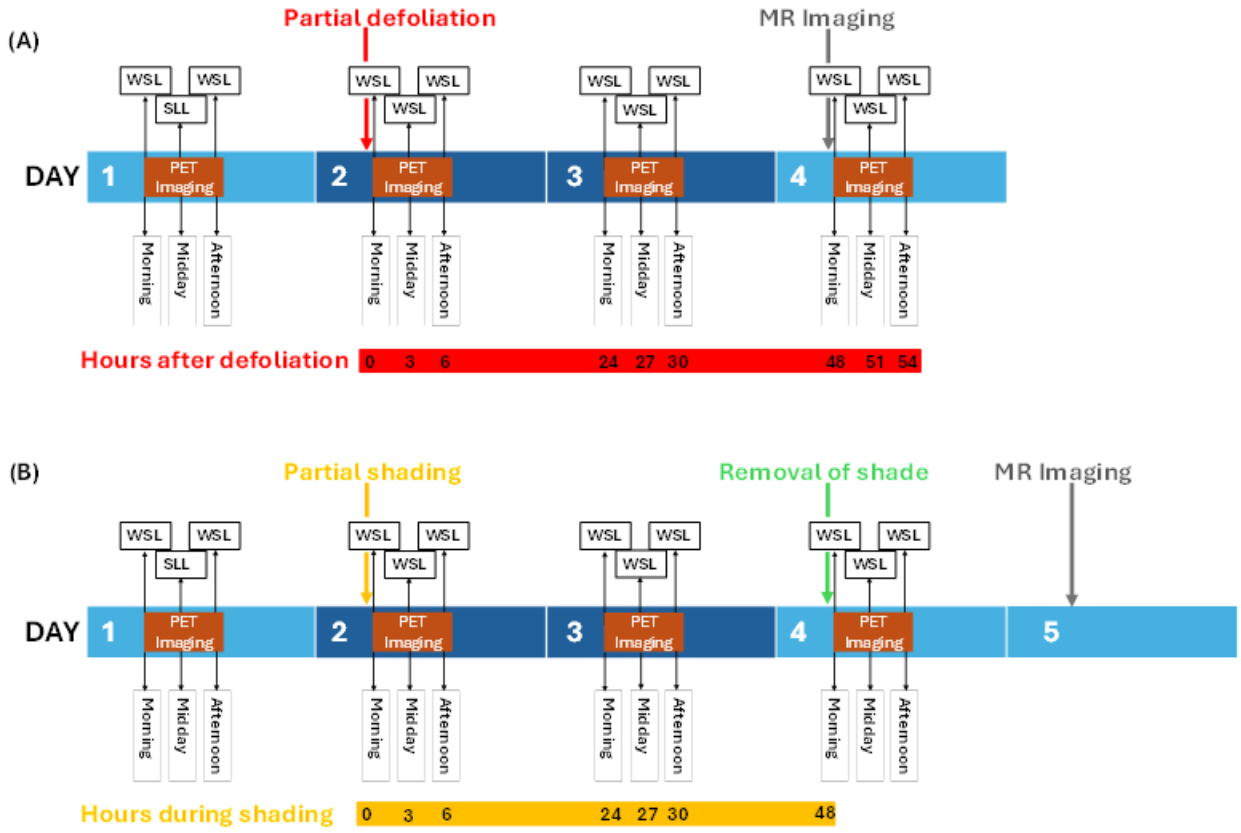

Figure 4.2. PET and MRI acquisition routines during partial defoliation and shading experiments on 63-day-old sugar beet. (A) PET and MRI routine for partial defoliation experiment, indicating PET acquisition period before and after partial defoliation, coupled with a one-time MR imaging; (B) PET and MRI routine for partial shading experiment, indicating PET imaging period before, during and after partial shading, coupled with a one-time MR imaging. WSL = whole shoot labelling, SLL = single leaf labelling.

4.2.4 Partial defoliation experiments

A single, fully expanded leaf that had previously been labelled was excised with a sharp cutting edge. Subsequently, the whole shoot of the partially pruned plant was labelled (Fig. 4.3C), and the taproot was imaged with *pheno*PET to determine ^{11}C distribution patterns across the taproot cross-section. PET measurements were done several times after excising a single leaf in a period of c. 54 hours. The PET and MRI routine (Fig. 4.2A) was repeated for three different partially defoliated sugar beet plants of the same age.

4.2.5 Partial shading experiment

A single, fully expanded leaf that had previously been labelled was wrapped in aluminum foil to induce partial shading by preventing incidental radiation to the selected leaf. The whole shoot of the partially shaded plant was labelled, and the taproot was imaged with *pheno*PET to determine ^{11}C distribution patterns across the taproot cross-section (Figs. 4.2B and 4.3C). PET measurements were performed several times over a 30-hour period partial shading (Fig. 4.2B). After 48 hours of consistent partial shading, the aluminum foil was removed from the leaf to reverse the partial shading. PET measurements were performed after removing the aluminum foil from the single leaf (Fig. 4.2B).

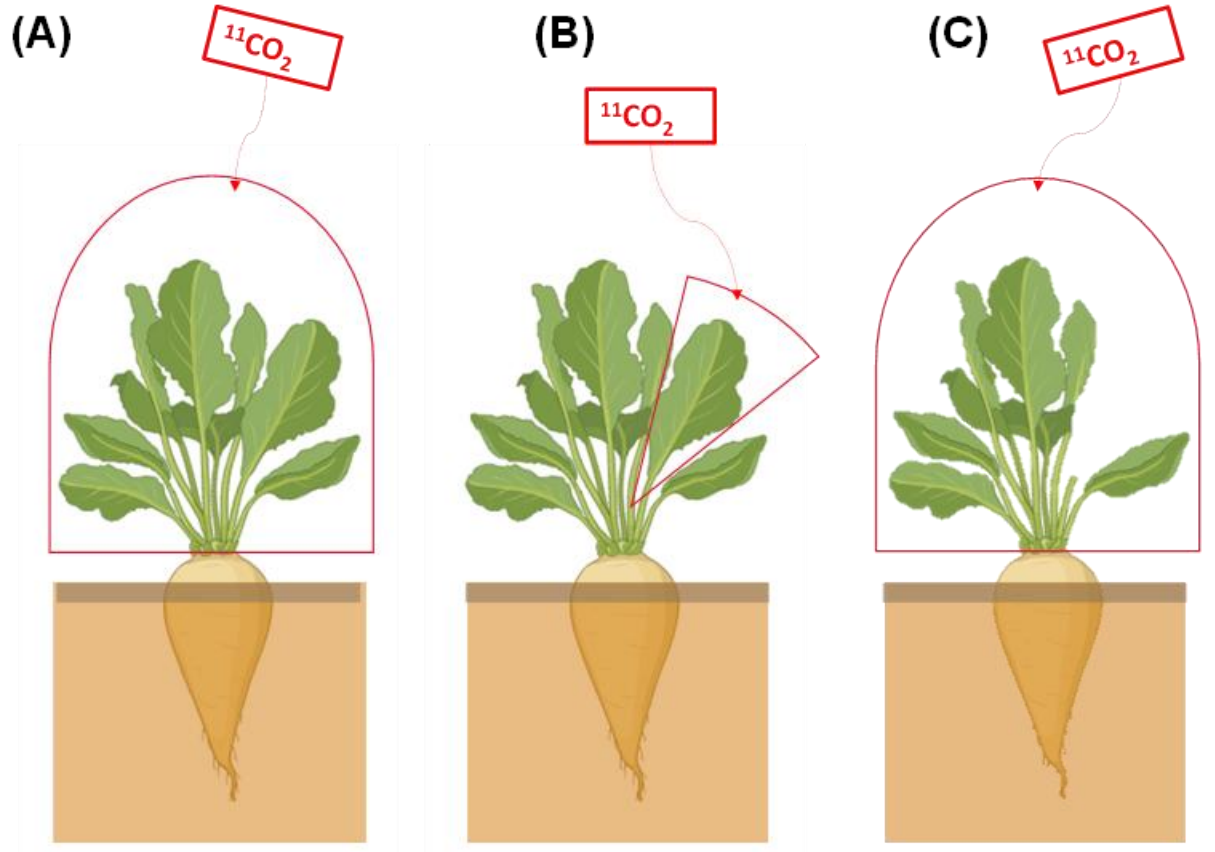

Figure 4.3. Labelling approaches for different experimental scenarios tested in this study. (A) WSL of an intact plant, (B) SLL of an intact sugar beet plant and (C) WSL of either partially defoliated or shaded sugar beet plant.

4.3 Results

As mentioned above, three plants were dedicated for partial defoliation experiments, and one plant to a partial shading experiment. In the following, samples for partial defoliation experiments are numbered as

P1-3 and sample for partial shading experiment is numbered as H1. Two types of projection images were generated from the PET data to visualize tracer distribution at different stages of the measurement process: Maximum intensity projection (MIP) and intra-measurement intensity projection (IIP). MIP images were generated at the end of each PET acquisition and provide an overall visualization of tracer distribution integrated over the entire scan duration. IIP images correspond to an image generated at selected time points within the full scan period.

4.3.1 Distribution patterns of recently fixed photoassimilates from a specific leaf

The distribution pattern of recently fixed photoassimilates for a specific leaf was determined by MRI-PET coregistration. The ^{11}C tracer translocated from a single leaf was mainly confined to a certain sector of the taproot corresponding to the architectural position of the labelled leaf (Fig. 4.4B,D and Supplementary Fig. C. S1). Considering the taproot cross-section as a pie chart, the overall tracer distribution for a single leaf of an intact sugar beet plant covered approximately a quarter of the whole cross-sectional area (Fig. 4.4B,D and Supplementary Fig. C. S1). The position of this quarter shifted slightly, assuming a helical-like trend as the tracer moved down on the vertical axis of the taproot (Supplementary Video C. S1). The distribution of ^{11}C tracer assumed a V-like shape with the ^{11}C tracer extending from the area covered by the central core of the taproot to mostly the inner four cambial rings, followed by an abrupt decline in ^{11}C tracer signal intensity for outer and periphery cambial rings (Fig 4.4B,D).

4.3.2 Effect of partial defoliation on the distribution pattern of recently fixed photoassimilates

After removal of a single leaf, the ^{11}C tracer from whole shoot labelling was distributed throughout the whole cross-section of the taproot. Thus, no pronounced differences in tracer distribution were observed before and after defoliation. Even though the distribution pattern was similar, it seems the overall ^{11}C tracer intensity was slightly reduced after partial defoliation (Fig. 4.5) compared to before partial defoliation (Fig. 4.4A). IIP coregistered with MR images (Fig. 4.6) revealed that the tracer arrived earliest after 45 min during PET imaging. Comparing measurements obtained prior to (Fig. 4.6A) and after partial defoliation (Fig. 4.6 B,C), there were no marked differences in tracer intensity throughout each PET imaging period at the sections where the excised leaf previously supplied its recently fixed photoassimilates as seen in Fig. 4.4B. Tracer distribution was quite homogenous for images obtained before and after partial

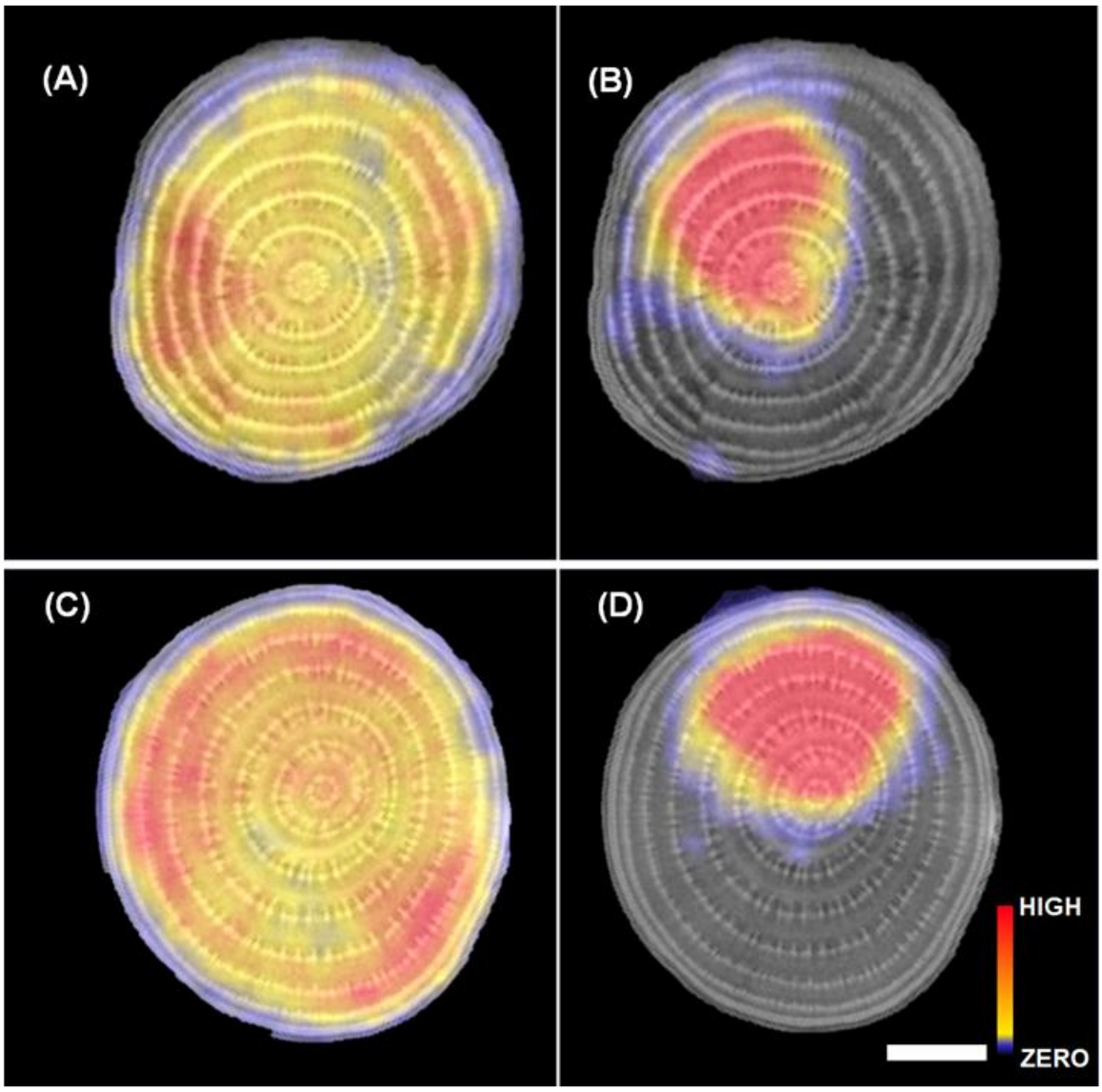

Figure 4.4. MIP of MRI-PET cross-sections of sugar beet taproot indicating distribution patterns of ^{11}C tracer over a cross-section of sugar beet taproot for different labelling approaches prior to defoliation or shading manipulation. (A,C) distribution of ^{11}C tracer within the taproot for whole shoot $^{11}CO_2$ labelling prior to defoliation and shading, respectively (WSL, morning) and (B,D) distribution of ^{11}C tracer within the taproot for a single leaf $^{11}CO_2$ labelling prior to defoliation and shading, respectively (SLL, midday). Among the three plants analyzed for partial defoliation experiment, representative example P1, which exhibited typical distribution patterns consistent with the other samples (P2 and P3, see Supplementary Figs. C. S1-3) is shown. Colored image parts represent PET, while grey image parts represent MRI. Areas with cooler colors (grey and blue) indicate a low ^{11}C tracer signal, while areas with warmer colors (yellow and red) indicate a high ^{11}C tracer signal. White bar, 0.5 cm.

defoliation, with subtle variations in tracer intensity across the taproot cross-section, regardless of the quarter where the excised leaf previously supplied its photoassimilates and even for an intact plant (Fig. 4.6). Moreover, the overall tracer intensity was higher throughout the measurement (i.e. 45-, 75-, 90- and 135-min during PET acquisition) for images obtained prior to defoliation (Fig. 4.6A), than for images obtained after defoliation (Fig. 4.6 B,C).

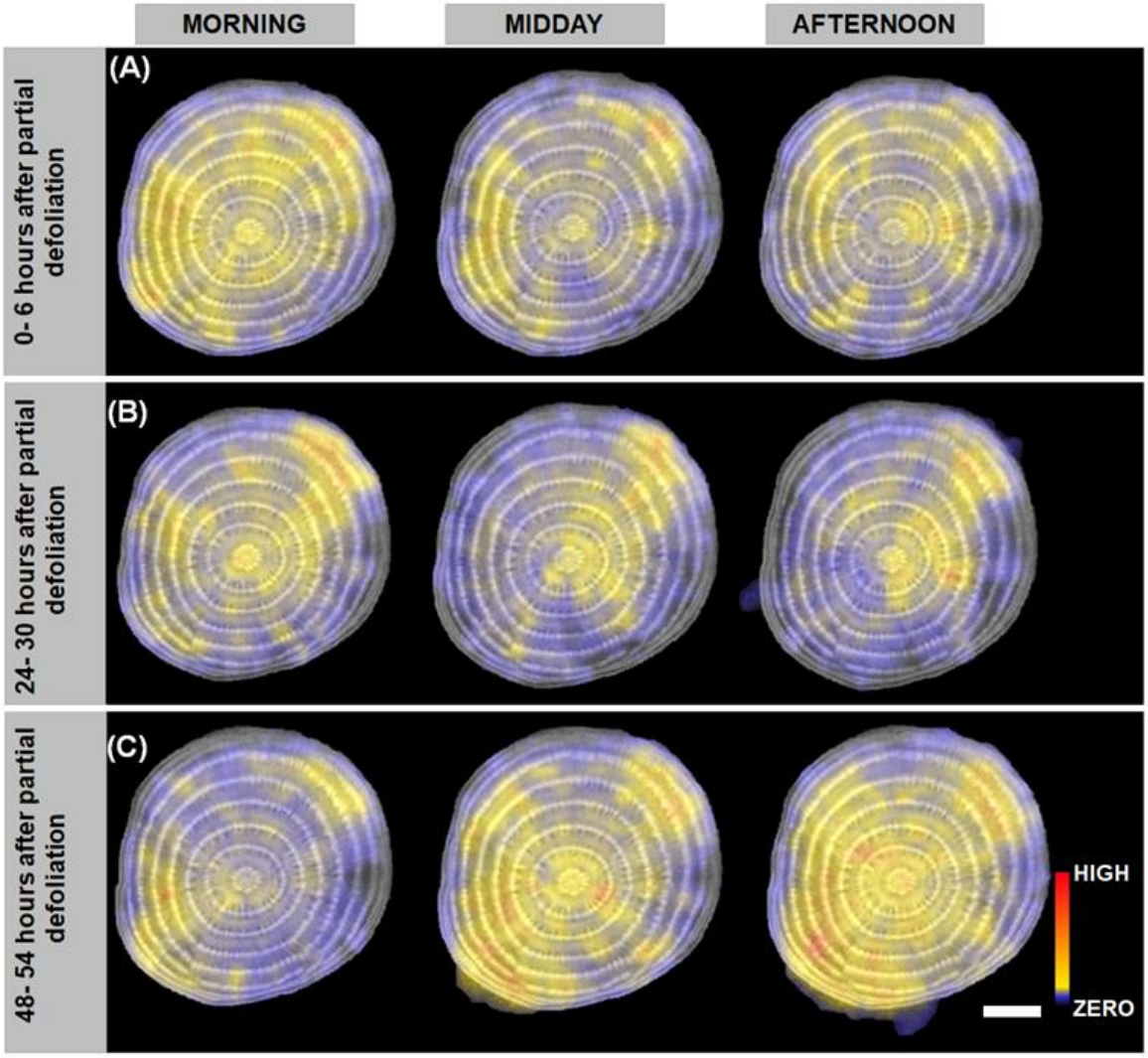

Figure 4.5. MIP of MRI-PET cross-sections of sugar beet taproot, indicating the distribution pattern of ^{11}C tracer over a cross-section of sugar beet taproot for partially defoliated sugar beet plant. The distribution pattern of ^{11}C tracer over a cross-section of sugar beet taproot (A) at 0-6 hours after partial defoliation, (B) at 24-30 hours after partial defoliation and (C) at 48-54 hours after partial defoliation. Colored image parts represent PET, while grey image parts represent MRI. Areas with cooler colors (grey and blue) indicate a low ^{11}C tracer activity while areas with warmer colors (yellow and red) indicate a high ^{11}C tracer activity. Measurements were obtained in the morning, midday and afternoon. White bar, 0.5 cm.

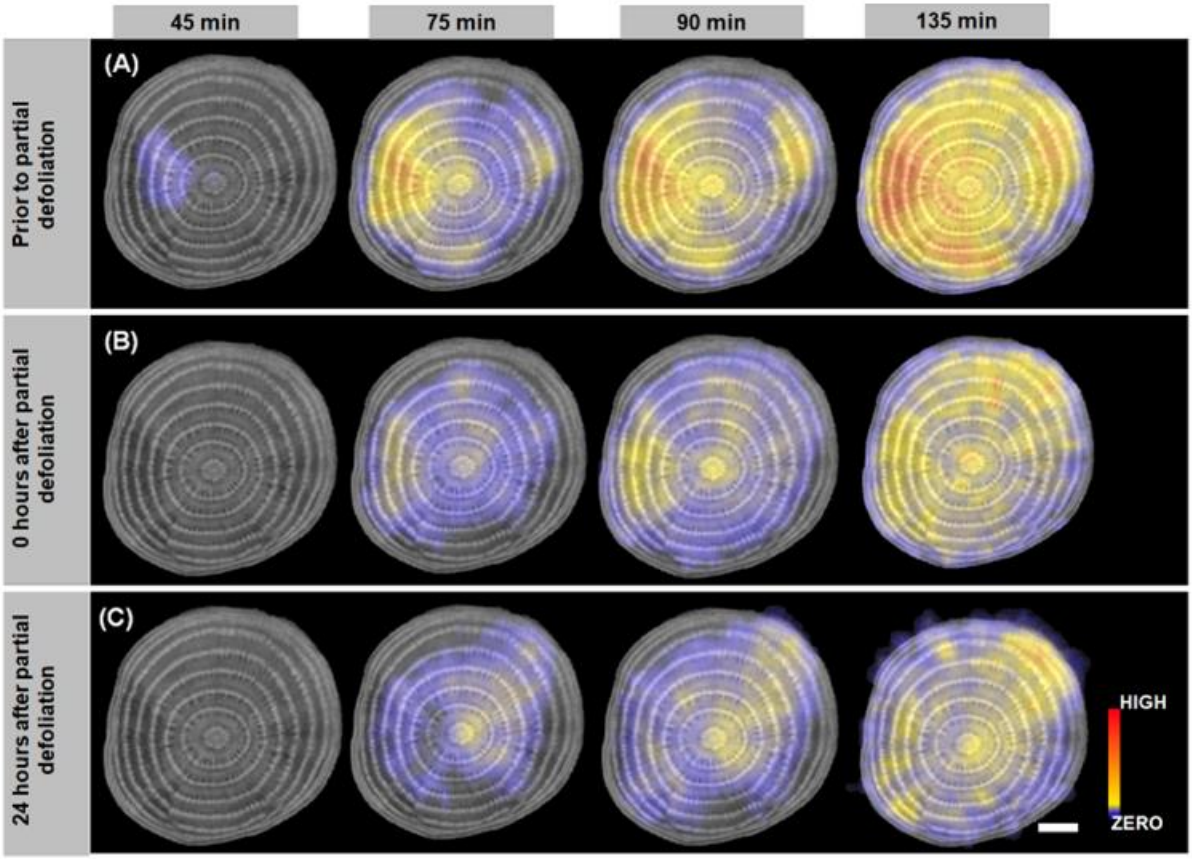

Figure 4.6. IIP of MRI-PET of intact and partially defoliated sugar beet taproot showing temporal ^{11}C tracer distribution over a cross-section of sugar beet taproot. Temporal projections at 45-, 75-, 90- and 135-min of PET imaging for whole shoot labelling in (A) the morning before defoliation, (B) at zero hours after defoliation and (C) at 24 hours after defoliation. Colored image parts represent PET, while grey image parts represent MRI. Areas with cooler colors (grey and blue) indicate a low ^{11}C tracer signal while areas with warmer colors (yellow and red) indicate a high ^{11}C tracer signal. Measurements presented here are the temporal intensity projections of "Morning" images shown in Figs. 4.4 A and 4.6 A,B. White bar, 0.5 cm.

4.3.3 Effect of partial shading on the distribution pattern of recently fixed photoassimilates

Similar to the partial defoliation experiment (section 4.3.2), the analysis of ^{11}C tracer distribution over a cross-section of sugar beet taproot determined how partial shading affects temporal distribution patterns of recently fixed photoassimilates. Observations from MRI-PET images indicated that shading a specific leaf induces a heterogeneous distribution of recently fixed photoassimilates (Fig. 4.7). The intensity of the ^{11}C tracer was reduced at a specific sector of the taproot cross-section. This effect was particularly pronounced for the first three measurements obtained during partial shading (i.e. 0-6 hours, Fig. 4.7A, see also Fig. 4.2B for measurement sequence). The sector of the taproot cross-section exhibiting less ^{11}C tracer

signal (Fig. 4.7A) was in congruence with the sector where the shaded leaf previously supplied ^{11}C tracer (Fig. 4.4D). This sectorality was not as pronounced anymore 24-30 hours after the beginning of shading. This indicated changes in the temporal pattern of photoassimilates distribution between measurements obtained at 0-6 hours of shading and 24-30 hours of shading. Similar to partial defoliation experiments, IIP of ^{11}C tracer distribution were further investigated (Fig. 4.8). Here, the IIP of PET obtained for an unshaded plant (morning; day one, Fig. 4.8A), the first measurement during shading (morning; day 2; 0 hours during shading, Fig. 4.8B) and the fourth measurement during shading (morning; day 3; 24 hours during shading, Fig. 4.8C) were compared. IIP were investigated at 55, 90 and 135 min during each measurement. In an unshaded sugar beet plant, the tracer distribution was homogenous (Fig. 4.8A). However, tracer arrived earliest (at about 55 min) within the area covering the inner four to five rings and later (after 90-135 min) spread to outer rings and the periphery (Fig. 4.8A). At zero hours during shading, a pronounced heterogeneity in tracer distribution was observed at 55- and 90-min, but at 135 min the overall distribution pattern tended to be homogenous (Fig. 4.8B). A similar pattern was observed for temporal ^{11}C profiles recorded 24 hours after the beginning of shading (Fig. 4.8C). But unlike observation made from measurements obtained at zero hours during shading, the tracer distribution tended to be homogeneous before 90 min during the PET imaging (Fig. 4.8C).

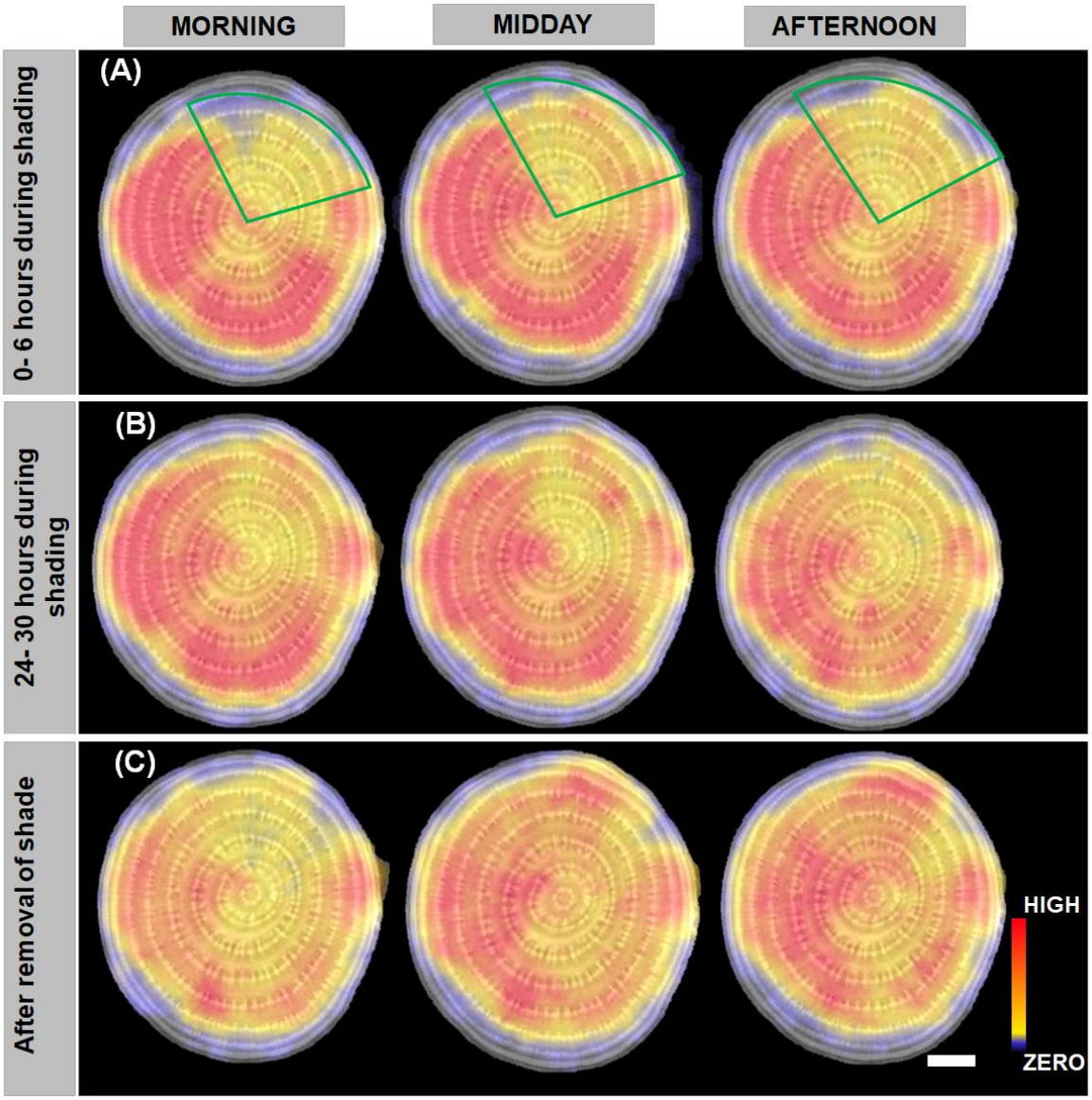

Figure 4.7. MIP of MRI-PET cross-sections of sugar beet taproot, indicating the distribution pattern of ^{11}C tracer over a cross-section of sugar beet taproot for a partially shaded and after removal of shade on the sugar beet plant. The distribution pattern of ^{11}C tracer over a cross-section sugar beet taproot (A) during 0-6 hours of shading, (B) for 24-30 hours during shading and (C) after removal of shade. Colored image parts represent PET, while grey image parts represent MRI. Areas with cooler colors (grey and blue) indicate a low ^{11}C tracer activity while areas with warmer colors (yellow and red) indicate a high ^{11}C tracer activity. Green shape indicates a sector with a relatively low ^{11}C tracer signal (covering most sections where the shaded leaf previously supplied most of the ^{11}C tracer as shown in Fig 4.4D). White bar, 0.5 cm.

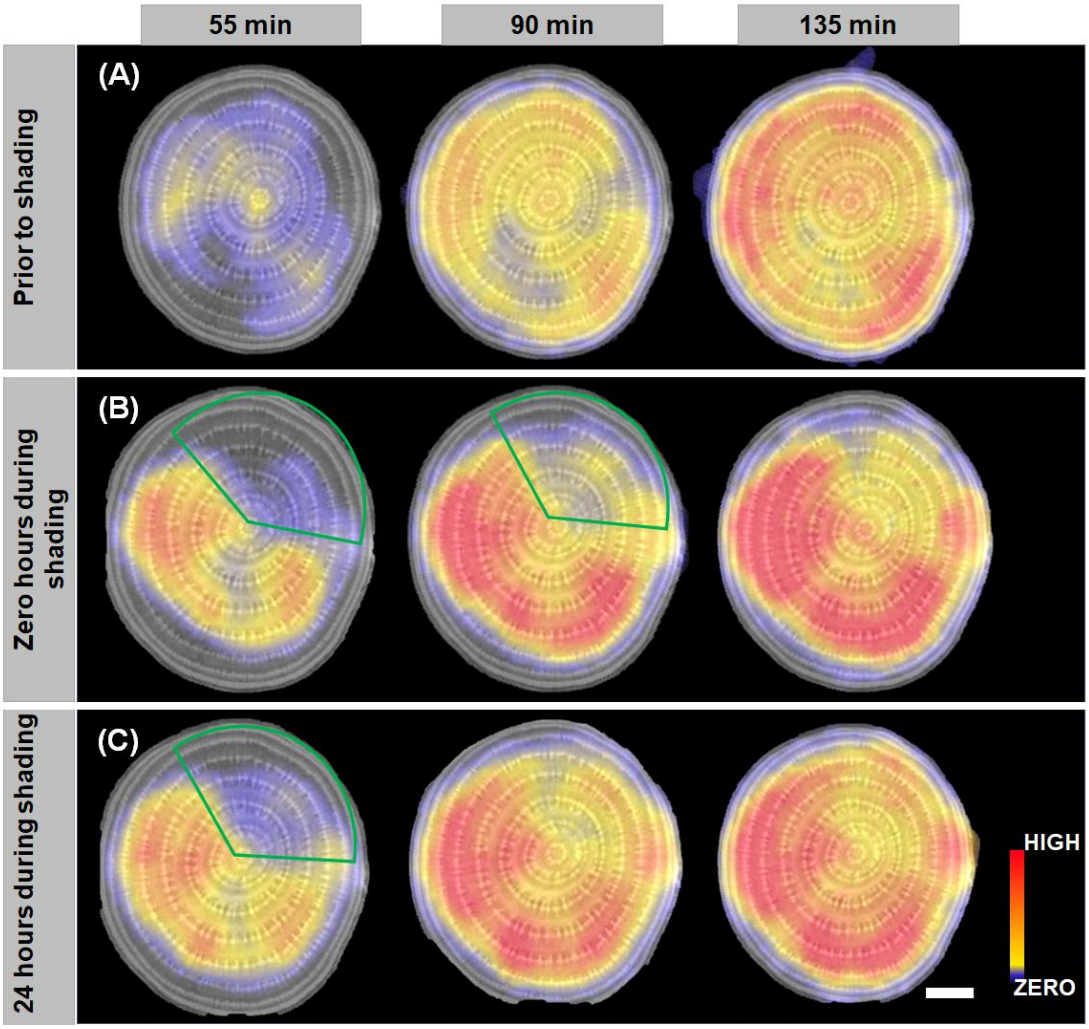

Figure 4.8. IIP of MRI-PET of intact and partially shaded sugar beet taproot showing temporal ^{11}C tracer distribution over a cross-section of sugar beet taproot cross-sections. (A) Temporal projections at 55-, 90- and 135-min of PET imaging for WSL in the morning before shading, (B) temporal projections at 55-, 90- and 135-min of PET imaging for WSL in the morning at zero hours during shading and (C) temporal projections at 55-, 90- and 135-min of PET imaging for WSL in the morning at 24 hours during shading. Colored image parts represent PET, while grey image parts represent MRI. Areas with cooler colors (grey and blue) indicate a low ^{11}C tracer signal while areas with warmer colors (yellow and red) indicate a high ^{11}C tracer signal. Green shape indicates sector with a relatively low ^{11}C tracer signal (covering most sections where the shaded leaf previously supplied most of the ^{11}C tracer, as shown in Fig. 4.4D). Measurements presented here are the temporal intensity projections of "Morning" images shown in Figs. 4.4D and 4.7A,B. White bar, 0.5 cm.

4.4 Discussion

4.4.1 Photoassimilates distribution within sugar beet taproot follows a restricted pathway and is dominant at some sectors

The finding of single leaf labelling leading to sectorial distribution of recently fixed photoassimilates in the taproot is consistent with evidence provided by Joy (1964) and Jahnke et al. (2009). Both reports showed that the translocation of labelled photoassimilates from source to sink follows an orthostichous pathway. The observed slight shift in position of the ^{11}C tracer distribution when moving down the vertical taproot axis is attributable to the spiral arrangement of the sugar beet vascular system (Artschwager, 1926; Stieber & Beringer, 1984; Zamski & Azenkot, 1981), which influences the trajectory of photoassimilates (Stieber & Beringer, 1984).

Apart from the transport pathway or the sectorial distribution, differences in signal intensity among different sections of the taproot cross-section indicate that photoassimilates are likely to arrive earliest at the inner section of the taproot. This observation can be linked to faster transport velocities recorded for inner section in **Chapter 3** (see Fig. 3.6). Together, this suggests that the flow of photoassimilates follows a dominant pathway, prioritizing inner zones of the taproot cross-section at the expense of the outer cambium zones towards the periphery. Probable mechanisms underlying this observation are elaborated in **Chapter 5**.

Although the ^{11}C tracer distribution within sugar beet taproot cross sections appeared homogeneous in intact and partially defoliated plants (Figs. 4.4A and 4.8A), subtle differences in tracer arrival time and signal intensity among different sectors of the cross-section were observed. These likely reflect source-sink dynamics, where certain leaves act as dominant sources, exporting more recently fixed photoassimilates to orthostichous taproot sectors. Leaf age influences this process: mature leaves primarily supply sinks, while maturing leaves retain some assimilates for growth (Joy, 1964). Thus, dominance of specific source leaves, channelling assimilates via orthostichy (Stieber & Beringer, 1984; Zamski & Azenkot, 1981), may explain the slight variations in ^{11}C tracer arrival and distribution.

4.4.2 Partial defoliation has limited effects on resource distribution homogeneity.

Because of the sectoral distribution of photoassimilates by a single leaf, it was expected that removing the source leaf that initially supplied tracer to a sector of the taproot (as shown for SLL in Fig. 4.4B) would deprive that sector of receiving ^{11}C tracer during subsequent WSL. However, no sector-specific limitation in the ^{11}C tracer signal intensity was observed. This suggests that the sugar beet plant has the capacity to

override commonly preferred phloem sap transport pathway by orthostichy, particularly in situations where vascular connections are mechanically disrupted (Joy, 1964; Schepper et al., 2013). This is similar to the observations made by Joy (1964), who noted that defoliation led to a homogeneous spread of photoassimilates from a single mature source leaf to young sink leaves. Moreover, Schepper et al. (2013) reported a breakdown in sectorality upon girdling the stem of an oak tree and further suggested that arrival of assimilates at the root is due to change in transport route towards undamaged phloem tissues. The direct attachment of the leaves of sugar beet plant to the crown, composed of complex vascular anastomoses (Zamski & Azenkot, 1981), could aid flexibility for a diverting resource in translocation (Joy, 1964). Another explanation for the homogeneous ^{11}C tracer distribution is that the treatment was not strong enough to induce heterogeneity. Such experimental simulations typically involve defoliating multiple source leaves (Castrillón-Arbeláez et al., 2012; Danckwerts & Gordon, 1987; Ferrieri et al., 2013; Schmitt et al., 2013; Schwachtje et al., 2006; Vargas-Ortiz et al., 2013).

4.4.3 Partial shading induces a sequential redistribution of recently fixed photoassimilates

In the previous paragraph, it was indicated that partial defoliation did not have any pronounced temporal effects on the distribution of recently fixed photoassimilates. On the contrary, for shading experiment, it was observed that some sectors of the taproot which aligned to the area in which the shaded leaf previously supplied photoassimilates, showed comparatively lower ^{11}C tracer signal (Figs. 4.7 and 4.8). Keller et al. (unpublished) made similar observations by performing shading experiments that closely resembled those described in this chapter. Such heterogeneity in resource distribution was expected, as shading was confined to a single source leaf (Orians & Jones, 2001). Even though clear sectorality was observed during early phase of shading (i.e. 0-6 hours), photoassimilates distribution became homogenous over the taproot cross-section at approximately 24 hours of shading (Fig. 4.7B). However, before the resource distribution became homogenous, a sectoral distribution pattern was observed for IIP at 55 min into the measurement during 24 hours of shading (Fig. 4.8C). This transient pattern may reflect continued export of stored (non-recent) photoassimilates from the shaded leaf (Schmitt et al., 2013; Danckwerts & Gordon, 1986). Because these pre-existing carbon pools could temporarily sustain phloem export along established pathways, reorganization of phloem flow to permit lateral redistribution of newly assimilated carbon was delayed. This suggests that unlike in a complete removal of a source leaf, the sugar beet plant requires some time to sense shading effects on the distribution of photoassimilates within the taproot. Plants' response to carbon distribution during shading or defoliation manipulation experiments

are highly dependent on the amount of damage done, the method of manipulation and sink priorities (Vargas-Ortiz et al., 2013)

Moreover, the temporal variations in levels of sectorality and subsequent homogeneity in tracer distribution indicate a possible lateral distribution of recently fixed photoassimilates, driven by localized shifts in sink strength (Fig. 4.8B,C). The initial reduction in ^{11}C tracer concentration at the sector where the shaded leaf previously supplied its recently fixed photoassimilates is likely to generate osmotic and pressure gradients that facilitate active, lateral transfer at the sites with little to no recently fixed photoassimilates (Patrick & Offer, 1996). Also, post-sieve element transport of photoassimilates in sink regions (Patrick & Offler, 1996) could be a mechanism driving the lateral distribution of recently fixed photoassimilates. This could be mediated by a diffusion of photoassimilates via the interconnecting plasmodesmata (Patrick & Offler, 1996).

CHAPTER 5

General Discussion

5 General discussion

This thesis characterized the effect of the biotic stressor SBR on structural development of sugar beet taproot and the distribution and transport dynamics of recently fixed photoassimilates within sugar beet taproot. The present chapter will discuss the major findings of this thesis, aiming to propose mechanisms regarding photoassimilates transport and distribution for the cases studied (summarized in Fig. 5.1). Further, this chapter will highlight the opportunities and challenges posed by the main methods employed. In the end, perspectives for future studies based on the results presented will be proposed.

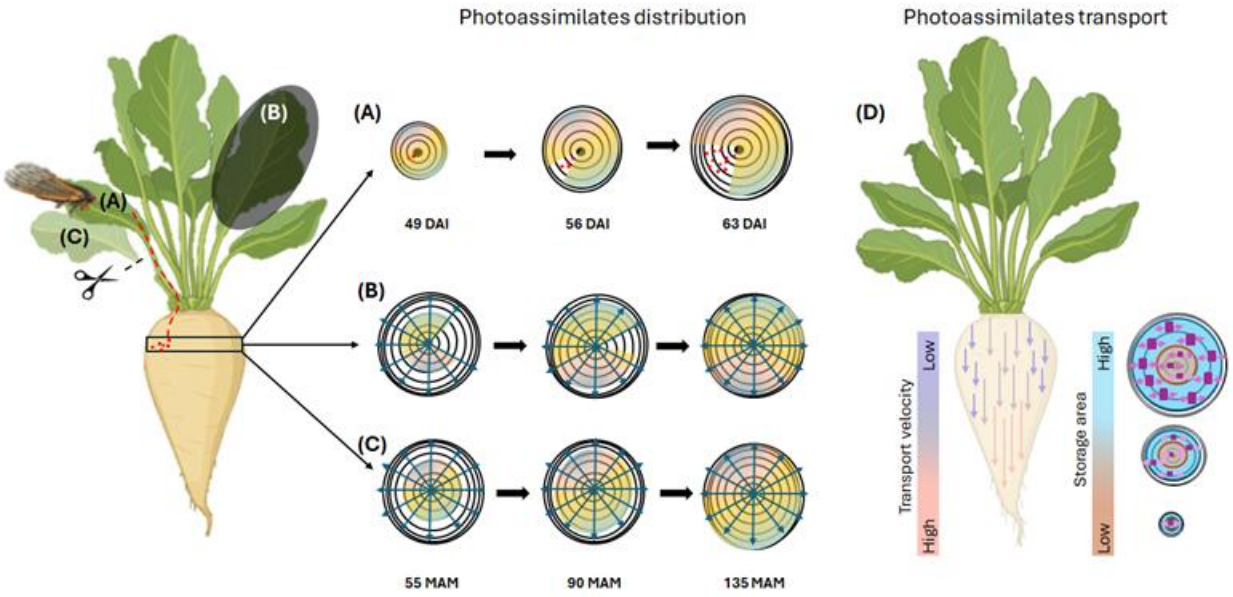

Figure 5.1. Summary of phloem sap distribution and transport in sugar beet taproots observed in this thesis. (A) Sector-specific transmission of SBR pathogens (red spheres) by *P. leporinus*, causing localized sectors with pathogen abundance and little or no recent photoassimilate accumulation. (B) Sectorial distribution after shading a single mature leaf, with gradual homogenization of phloem sap achieved by lateral distribution through phloem pathways (blue arrows), in contrast to (C) homogeneous distribution after excision of a mature leaf due to rapid rerouting of phloem sap. (D) Transport velocities across taproot regions: slower in upper sections and mid zones with high exchange processes with surrounding tissue (purple rectangles with arrows), and faster in lower and inner sections; arrow length indicates velocity (long = fast, short = slow). DAI = days after inoculation, MAM = minutes after manipulation.

5.1 SBR pathogen dissemination in the taproot and the resulting morpho-physiological effects

The findings obtained in **Chapters 2 and 4** suggest that shoot architecture, together with orthostichy and vascular anastomoses, determines the distribution of phloem sap in sugar beet plant. Phloem-restricted pathogens utilize phloem sap as a transmission medium during vector feeding (Christensen et al., 2004; Tatineni et al., 2008) and spread within the sugar beet taproot via orthostichous pathways. This thesis proposes that the transmission of the SBR pathogens by *P leporinus* is shoot-sector specific (Fig 5.1A, i.e. depending on which leaf the vector feeds on during transmission). Therefore, pathogen abundance and their resulting anatomical and physiological alterations will be localized to specific sector or patchy among different sectors. This depends on whether the vector feeds on phloem sap of a single or several leaves and transmits the bacterium. As demonstrated in **Chapter 3**, SBR disease had no effects on phloem sap flow velocity (see Fig. 3.7). The localized effects of the SBR pathogen within certain taproot sectors as observed in **Chapter 2** (see Figs. 2.3 and 2.6) help to explain why phloem sap velocity remained stable in the unaffected sectors. Typically, the strength of receiving sink organs is a major determinant of how resources are distributed within sugar beet taproot. This implies that the tissues surrounding the diseased tissues (Figs 2.3 and 2.6) remained healthy, so that they could maintain transport velocities of the phloem sap.

5.2 What drives photoassimilates transport in sugar beet taproots?

Early sugar beet taproot development is marked by distinct metabolic phases that influence photoassimilates transport and partitioning (Jammer et al., 2020; Zhang et al., 2017). According to Jammer et al. (2020), elevated extracellular invertase activity and subsequent high hexose-to-sucrose ratios during the pre-storage (earliest) phase of taproot development can generate steep concentration gradients and create “high” source and “low” sink pressure differentials. Per the Münch (1930) hypothesis, such pressure differentials drive faster bulk flow of the phloem sap. Consistent with this, the data presented in **Chapter 3** (see Figs. 3.5, 3.6 and 3.7) show that transport velocities are highest during earliest phase (i.e. before 60 d) but decline as the taproot matures. This reduction reflects both developmental and spatial shifts in sink activity. Initially, the lower sections act as strong sinks, sustaining long-distance pressure gradients and fast transport. As sucrose storage intensifies in the upper taproot sections, exchange processes (Fig. 5.1D) occur closer to the phloem entry points, reducing the pressure differential along the transport pathway resulting in reduced transport velocity toward distal regions. Conversely, sink strength remains

concentrated in the lower sections due to lower exchange processes, thereby maintaining pressure gradient to support fast velocities. These observations indicate that phloem transport velocity is closely linked to both developmental stage and the spatial distribution of sink activity, consistent with the phase-specific metabolic and enzymatic patterns described by Jammer et al. (2020).

The findings obtained in **Chapters 3 and 4** (see Figs. 3.6, 3.10, 4.6 and 4.8) consistently indicate that tracer transport velocities and arrival times vary radially over the taproot cross-section, with photoassimilates arriving earliest at the inner zones, followed by mid and the periphery zones. This suggests that the flow of photoassimilates follows a dominant pathway, prioritizing inner zones of the taproot cross-section at the expense of the outer cambium zones towards the periphery. Several reasons could account for this observation. Firstly, the peripheral areas are mostly composed of undifferentiated cambial rings (Zamski & Azenkot, 1981). Innermost rings are initiated during early stages of the development of sugar beet taproot (Artschwager, 1926; Jammer et al., 2020). Moreover, the innermost rings have the broadest band of storage parenchyma (Artschwager, 1926; Zamski & Azenkot, 1981). These render the innermost sectors as dominant spots for sucrose accumulation and hence prioritized for photoassimilates distribution.

Apart from bulk flow, sink metabolism and compartmentation is likely to influence post-sieve element transport (Patrick & Offler, 1995). According to Patrick & Offler (1995), plasmodesmata driven diffusion of photoassimilate resources is likely to occur especially when there are turgor differences among radial regions within the receiving sink cells. Radial turgor differences may drive lateral redistribution of photoassimilates. In **Chapter 4** (see Figs. 4.6 and 4.8), it was reported that recently fixed photoassimilates arrive earliest in the inner zone and later diffuse to the mid and outer zones. Such lateral transport might be dominant in the upper section and mid zone when compared to lower section and inner zone, respectively, since lower section and inner zone share a similar trajectory. This is likely to impede longitudinal phloem sap movement and hence, lead to a reduced flow momentum.

5.3 Effects of metabolic and vascular constraints on photoassimilates distribution within sugar beet taproot

The sectorial distribution of phloem sap by a single source leaf (see Fig. 4.4 and Supplementary Fig. C. S1) supports the argument that orthostichy determines the sectors where fixed photoassimilates are distributed in taproot sink (Jahnke et al., 2009; Joy, 1964). However, vascular anastomosis may enable the distribution of photoassimilates, especially when orthostichous pathways are missing (Joy, 1964). This thesis demonstrated that the redistribution of recently fixed photoassimilates occurs when orthostichous

pathways are disrupted, for example, by shading a single source leaf (see Fig. 4.8B,C). Therefore, it is suggested that a healthy sugar beet taproot seems to attain homogeneity in resource distribution through lateral redistribution of photoassimilates via subtle vascular pathways (Fig. 5.1B,C). Owing to the observed redistribution and homogenization of phloem sap distribution upon disruption of orthostichous pathways, the missing recently fixed photoassimilates within sectors of the sugar beet taproot upon SBR disease (see Fig. 2.7) is due to reduced sink capacity. The abundance of the SBR pathogens at a specific sector of the taproot (Fig. 5.1A) renders these sectors weak receiving sink cells, thereby prioritizing the supply of recently fixed photoassimilates to a certain "healthier" sectors over "infected" sectors within the taproot.

5.4 Opportunities and challenges in employing MRI-PET to monitor photoassimilates distribution during sugar beet-disease interactions

This thesis combined MRI and PET to obtain multimodal image data for a comprehensive analysis of a plant-pathogen interaction. This permitted the analysis of functional and morphological parameters related to SBR disease incidence and progression on sugar beet taproot temporally and spatially. The results of this thesis demonstrate that combined MRI-PET can be adopted for dissecting the mechanisms of plant-pathogen interactions and elucidating the functional and morphological aspects of plant susceptibility to diseases. An advantage is the early detection of disease related changes in belowground plant organs before aboveground symptoms become visually apparent. Such early assessments of plant organ reactions are critical during investigating plant-pathogen interaction (Simko et al., 2017). The non-invasive nature of this approach allows direct monitoring of disease progression on individual plants, eliminating otherwise invasive and labor-intensive sampling to achieve such temporal data. Hence, the utility of this unique approach should be extended to other storage root organs and other pathosystems.

From the observed differences in phenotypic plasticity, it can be assumed that the sugar beet plant reprograms its gene expression profiles when faced with the scenarios tested in this thesis. Similar changes in gene expression profiles have been reported by Kebrom (2024) in sorghum plants upon defoliation and shading. Temporal regulation of sucrose transporter genes in relation to the observed temporal distribution pattern of recently fixed photoassimilates may provide clearer clues on molecular mechanisms regulating photoassimilates distribution in sugar beet taproot under such experimental manipulation. Hence the results obtained from MRI-PET imaging could be used as a guide for sampling taproot for further molecular analysis (Schultes et al., 2025). This will allow analysis of gene expression and enzyme synthesis over time courses in the regions of interest (Castrillón-Arbeláez et al., 2012; Kebrom, 2024).

Even though the potency in employing combined MRI-PET as a tool for studying plant-pathogen interactions has been well established in this thesis, several bottlenecks are associated with enabling these technologies for studying plant-disease interactions. In general, MRI and PET are rarely used for evaluating plant-disease interactions due to the high complexity and nonportability of both technologies (Simko et al., 2017). These methods have so far only been applicable to plants grown in pots and under climate-controlled conditions (Simko et al., 2017), so that its use benefits deep plant phenotyping, enabling capturing traits of the hidden belowground crop organs.

When exposed to stressors, plants preferentially allocate carbohydrates to their root system (Ferrieri et al., 2013; Jackson & Caldwell, 1992; Schwachtje et al., 2006), possibly to maintain the uptake of soil nutrients (Jackson & Caldwell, 1992). Whether sugar beet prioritizes photoassimilates to the belowground sink organ at the expense of young sink leaves was not ascertained in this thesis. Comparing the allocation between above-and-below-ground sink organs and their phloem sap metabolome may reveal detailed insights regarding dynamics and regulation of photoassimilate distribution among these organs. Hence future studies should consider capturing allocation dynamics and the phloem sap metabolome of both young sink leaves and belowground sink. This will give a comprehensive overview of dynamics in photoassimilates distribution patterns for healthy and diseased samples, or prior to and after manipulation of source organs (Broussard et al., 2023; Imada et al., 2017).

The short half-life of the ^{11}C tracer allowed monitoring the dynamics of the distribution pattern of recently fixed photoassimilates, providing information on short-term (re)distribution patterns. However, the data presented in this thesis did not capture the total carbon pool, because changes in the distribution of non-recent photoassimilates were not investigated. This limits information regarding the remobilization of stored carbon resources upon SBR or shoot manipulations. The integration of additional carbon isotopes, such as the stable tracer ^{13}C (Kakouridis et al., 2024; Schultes et al., 2025) or the long-lived ^{14}C (Joy, 1964; Rodrigues et al., 2020; Schmitt et al., 2013), alongside ^{11}C (Schultes et al. 2025) provides a powerful approach for concurrently resolving short- and long-term carbon dynamics and could complement the data presented in this thesis and hence should be considered for future experiments.

Per the standard protocol of *pheno*PET, each PET scan takes about 150 min, so that a maximum of four plants can be measured by PET per day (Hinz et al., 2024). The very low throughput of the *pheno*PET system limits the number of plant samples that can be measured per batch of experiment. Unlike the PET system, the plant dedicated MRI platform overcomes the challenge of the very limited number of plant scans per batch of experiment, thereby enabling measurements of relatively larger number of plant

samples. The spatial resolution of both MRI and PET limits the detection level and hence it is difficult to detect very fine root structures. For example, van Dusschoten et al. (2016) recorded MRI detection limit between 200 and 300 µm. Since the primary focus of this thesis was on the storage organ, this limitation did not affect the current analysis. Nevertheless, incorporating information on fine roots could provide valuable insights into plant-pathogen interactions. For instance, revealing whether fine root plasticity occurs in response to infection. Recent advances in image analysis, such as the application of 3D convolutional neural networks for tomographic data, have shown promise in denoising and enhancing image quality (Pfaehler et al., 2025; Schaefferkoetter et al., 2020), especially for line-like structures in MR images (Pfaehler et al., 2025). Applying such methods could aid extracting fine root information from datasets obtained in this thesis or in future experiments and hence, this potential should be explored. Even though rapid screening of genotypes can be hindered by the low throughput of ^{11}C labelling and PET imaging, the early detection of SBR related disease effects by MRI will benefit the testing of preselected superior genotype candidates for future breeding programs.

The whole shoot cuvette is small and hence the shoot of maturing plants are somehow squeezed in the cuvette when enclosing the shoot into the cuvette system. This restraining may lead to perturbation of shoot as well as reduced exposure to incident radiation and could have some effects on assimilation rates of plants. Also, assimilation rates were estimated per µmol s^{-1} and were not normalized by leaf area. This is because assimilation rates were estimated for whole shoot without estimating total leaf area of the shoot of the plant. Recently, higher assimilation rates were linked to higher transport velocities but for normalized values estimated per µmol m^{-2} s^{-1} (Zierer et al., 2025). The perturbations posed by restraining shoot in the cuvette system and the unnormalized assimilation rates make it difficult to link assimilation rates to transport properties but rather, used as an index to monitor active uptake of labeled photoassimilates like in the studies of Metzner et al. (2022) and Karve et al. (2015). Approaching these problems will require improving the cuvette system to accommodate the whole shoot of the plant without restraining the shoot. Moreover, determining shoot area prior to or during PET acquisition by parallel non-invasive shoot imaging with 3D scanners or integrating 3D scanners in the current *pheno*PET setup will enable area-based normalization of assimilation rates (i.e. per µmol m^{-2} s^{-1}). These will improve accuracy of assimilation rates data and enable precise interpretations of plant performance based on assimilation rates when recorded for whole shoot.

5.5 Summary and Outlook

The thesis studied the effects of SBR biotic stressor, partial defoliation and partial shading on photoassimilates distribution in sugar beet taproot growing under climate chamber conditions. By linking spatial-temporal photoassimilates allocation patterns and phloem transport properties, complemented with taproot structural development and its anatomical features, the thesis provides mechanistic understanding of how exogenous factors alter source-sink dynamics in sugar beet taproots.

A sectorial distribution of recently fixed photoassimilates within the taproot, altered cross-sectional tissue organization and reduction in taproot development was observed during SBR-sugar beet interaction, highlighting how biotic stress disrupts source-sink allocation patterns.

A detailed characterization of photoassimilates transport within the taproot was achieved by quantifying tracer transport velocities and storage among vertical sections and radial zones in the developing taproot. A major finding is the variation in transport velocities between taproot sections or zones and for the developing taproot.

Effects of single leaf shading and removal were compared to gain deeper understanding on how shoot architecture and manipulation of shoot parts affect the distribution of recently fixed photoassimilates within sugar beet taproot. An early arrival of photoassimilates at the innermost taproot zones was observed, indicating that these sections become a priority in terms of sucrose accumulation. Under different manipulation scenarios, distinct distribution patterns of recently fixed photoassimilates were observed within the cross-section of sugar beet taproots. It seems that the photoassimilates are laterally (re)distributed within the taproot when parts of connecting shoot vasculature is disturbed or rendered transport inactive. But when the vasculature of belowground taproot is disturbed by biotic stressor (as in the case of SBR), photoassimilates distribution becomes limited at the infected sectors, thereby affecting sink capacity and the development of taproot sink organ.

The variation in flow velocities and tracer arrival times among taproot sections and zones open several questions about spatial and temporal differences in phloem structure and function for maintaining efficient photoassimilates transport within the sugar beet storage organ. Future studies should aim to quantify changes in sieve element conductivity, osmotic potential, and turgor pressure along the vertical axis to better link anatomical development with transport performance. Integrating high-resolution microscopy (e.g., confocal or electron microscopy), tracer studies (Lanzrath et al., 2025; Zierer et al., 2025), and model-based analysis (Bühler et al., 2014) like those applied in this thesis could further elucidate how

the phloem architecture adapts to meet the changing metabolic demands of the taproot during storage and development.

Linking the data from different experiments presented in this thesis, it can be clearly established that sink strength limitation is a major factor affecting photoassimilates distribution within the sugar beet taproot upon SBR disease. Several questions regarding how sugar beet plants coordinate their inducible defense responses to sense the presence of SBR pathogens and mount effective defense responses remain unanswered. It is still speculative that the brownish discoloration of vascular bundles in the taproot after SBR pathogens infection reflects an innate defense response, such as programmed cell death or callose deposition to limit pathogens spread (Gatineau et al., 2022). Whether the brownish discoloration of vascular bundles plays further roles in SBR pathogenesis and plant immunity should be investigated.

Building on the insights gained from this thesis, the tomographic image data (especially MR images), when linked to optical sensor data like that of Detring et al. (2025) using machine learning-driven image analysis and computational modeling, will provide a holistic overview of functional and structural relationships among above-and below-ground organs of sugar beet during SBR disease pathogenesis. Future research should investigate the combined effects of SBR biotic stressor and abiotic constraints such as drought, or nutrient limitations on belowground photoassimilates partitioning. The utility of MRI-PET to characterize vascular dysfunction should be extended to other key belowground economic species (e.g., potato, cassava, carrot and yam) facing vascular pathogens. This will help reveal source-sink dynamics that can benefit future breeding programs aiming for improved yield and stress resilience.

References

Artschwager, E. (1926). Anatomy of the vegetative organs of the sugar beet. *Journal of Agricultural Resource*, *33*(2), 143–176.

Artschwager, E. (1930). A Study of the Structure of Sugar Beets in Relation to Sugar Content and Type. *Journal of Agricultural Resource*, 867–915. https://naldc.nal.usda.gov/catalog/IND43967866

Babst, B. A., Ferrieri, R. A., Thorpe, M. R., & Orians, C. M. (2008). Lymantria dispar herbivory induces rapid changes in carbon transport and partitioning in Populus nigra. *Entomologia Experimentalis Et Applicata*, *128*(1), 117–125. https://doi.org/10.1111/j.1570-7458.2008.00698.x

Babst, B.A., Ferrieri, R., Schueller, M. (2019). Detecting Rapid Changes in Carbon Transport and Partitioning with Carbon-11 (11C). In *Phloem: Methods and protocols* (pp. 163–176) https://doi.org/10.1007/978-1-4939-9562-2

Beer, S., M., Hombach, T., Bühler, J., Jahnke, S., Khodaverdi, M., Larue, H., Minwuyelet, S., Parl, C., Roeb, G., Schurr, U., & Ziemons, K. (2010). Design and initial performance of PlanTIS: A high-resolution positron emission tomograph for plants. *Physics in Medicine and Biology*, *55*(3), 635–646. https://doi.org/10.1088/0031-9155/55/3/006

Behrmann, S. C., Rinklef, A., Lang, C., Vilcinskas, A., & Lee, K.-Z. (2023). Potato (Solanum tuberosum) as a New Host for Pentastiridius leporinus (Hemiptera: Cixiidae) and Candidatus Arsenophonus Phytopathogenicus. *Insects*, *14*(3), 281. https://doi.org/10.3390/insects14030281

Behrmann, S. C., Witczak, N., Lang, C., Schieler, M., Dettweiler, A., Kleinhenz, B., Schwind, M., Vilcinskas, A., & Lee, K.-Z. (2022). Biology and Rearing of an Emerging Sugar Beet Pest: The Planthopper Pentastiridius leporinus. *Insects*, *13*(7), 656. https://doi.org/10.3390/insects13070656

Bendix, C., & Lewis, J. D. (2018). The enemy within: Phloem-limited pathogens. *Molecular Plant Pathology*, *19*(1), 238–254. https://doi.org/10.1111/mpp.12526

Bosco, D., & Tedeschi, R. (2013). Insect vector transmission assays. *Phytoplasma*, *938*, 73–85. https://doi.org/10.1007/978-1-62703-089-2_7

Bové, J., & Garnier, M. (2003). Phloem-and xylem-restricted plant pathogenic bacteria. *Plant Science*, *164*(3), 423–438. https://doi.org/10.1016/S0168-9452(03)00033-5

Braun, D. M. (2022). Phloem Loading and Unloading of Sucrose: What a Long, Strange Trip from Source to Sink. *Annual Review of Plant Biology*, *73*(1), 553–584. https://doi.org/10.1146/annurev-arplant-070721-083240

Braun, D. M., Wang, L., & Ruan, Y.-L. (2014). Understanding and manipulating sucrose phloem loading, unloading, metabolism, and signalling to enhance crop yield and food security. *Journal of Experimental Botany*, *65*(7), 1713–1735. https://doi.org/10.1093/jxb/ert416

Bressan, A. (2009). Agronomic practices as potential sustainable options for the management of Pentastiridius leporinus (Hemiptera: Cixiidae) in sugar beet crops. *Journal of Applied Entomology*, *133*(9-10), 760–766. https://doi.org/10.1111/j.1439-0418.2009.01407.x

Bressan, A., Moral García, F. J., & Boudon-Padieu, E. (2011). The prevalence of 'Candidatus Arsenophonus phytopathogenicus' infecting the planthopper Pentastiridius leporinus (Hemiptera: Cixiidae) increase nonlinearly with the population abundance in sugar beet fields. *Environmental Entomology*, *40*(6), 1345–1352. https://doi.org/10.1603/EN10257

Bressan, A. (2014). Emergence and evolution of Arsenophonus bacteria as insect-vectored plant pathogens. *Infection, Genetics and Evolution : Journal of Molecular Epidemiology and Evolutionary Genetics in Infectious Diseases*, *22*, 81–90. https://doi.org/10.1016/j.meegid.2014.01.004

Bressan, A., Moral García, F. J., Sémétey, O., & Boudon-Padieu, E. (2010). Spatio-temporal pattern of Pentastiridius leporinus migration in an ephemeral cropping system. *Agricultural and Forest Entomology*, *12*(1), 59–68. https://doi.org/10.1111/j.1461-9563.2009.00450.x

Bressan, A., Sémétey, O., Nusillard, B., Clair, D., & Boudon-Padieu, E. (2008). Insect Vectors (Hemiptera: Cixiidae) and Pathogens Associated with the Disease Syndrome “Basses Richesses” of Sugar Beet in France. *Plant Disease*, *92*(1), 113–119. https://doi.org/10.1094/PDIS-92-1-0113

Bressan, A., Terlizzi, F., & Credi, R. (2012). Independent origins of vectored plant pathogenic bacteria from arthropod-associated Arsenophonus endosymbionts. *Microbial Ecology*, *63*(3), 628–638. https://doi.org/10.1007/s00248-011-9933-5

Broussard, L., Abadie, C., Lalande, J., Limami, A. M., Lothier, J., & Tcherkez, G. (2023). Phloem Sap Composition: What Have We Learnt from Metabolomics? *International Journal of Molecular Sciences*, *24*(8). https://doi.org/10.3390/ijms24086917

Bühler, J., Lieres, E. von, & Huber, G. (2014). A class of compartmental models for long-distance tracer transport in plants. *Journal of Theoretical Biology*, *341*, 131–142. https://doi.org/10.1016/j.jtbi.2013.09.023

Castrillón-Arbeláez, P. A., Martínez-Gallardo, N., Arnaut, H. A., Tiessen, A., & Délano-Frier, J. P. (2012). Metabolic and enzymatic changes associated with carbon mobilization, utilization and replenishment triggered in grain amaranth (Amaranthus cruentus) in response to partial

defoliation by mechanical injury or insect herbivory. *BMC Plant Biology*, *12*(1), 163. https://doi.org/10.1186/1471-2229-12-163

Chen, L.-Q., Hou, B.-H., Lalonde, S., Takanaga, H., Hartung, M. L., Qu, X.-Q., Guo, W.-J., Kim, J.-G., Underwood, W., Chaudhuri, B., Chermak, D., Antony, G., White, F. F., Somerville, S. C., Mudgett, M. B., & Frommer, W. B. (2010). Sugar transporters for intercellular exchange and nutrition of pathogens. *Nature*, *468*(7323), 527–532. https://doi.org/10.1038/nature09606

Christensen, N. M., Nicolaisen, M., Hansen, M., & Schulz, A. (2004). Distribution of Phytoplasmas in Infected Plants as Revealed by Real-Time PCR and Bioimaging. *Molecular Plant-Microbe Interactions : MPMI*, *17*(11), 1175–1184.

Danckwerts, J. E., & Gordon, A. J. (1987). Long-term Partitioning, Storage and Re-mobilization of 14C Assimilated by Lolium perenne (cv. Melle). *Annals of Botany*, *59*(1), 55–66. https://doi.org/10.1093/oxfordjournals.aob.a087285

Demmig-Adams, B., Stewart, J. J., & Adams, W. W. (2014). Multiple feedbacks between chloroplast and whole plant in the context of plant adaptation and acclimation to the environment. *Philosophical Transactions of the Royal Society of London. Series B, Biological Sciences*, *369*(1640), 20130244. https://doi.org/10.1098/rstb.2013.0244

Detring, J., Bömer, J., Gupta, A., Eini, O., & Mahlein, A.-K. (2025). Phenotyping of Syndrome "Basses Richesses" in Sugar Beet by Morphological and Spectral Traits. *Phytopathology.* Advance online publication. https://doi.org/10.1094/PHYTO-07-25-0239-R

Duduk, B., Ćurčić, Ž., Stepanović, J., Böhm, J. W., Kosovac, A., Rekanović, E., & Kube, M. (2023). Prevalence of a 'Candidatus Phytoplasma solani'-Related Strain Designated as New 16SrXII-P Subgroup over 'Candidatus Arsenophonus phytopathogenicus' in Sugar Beet in Eastern Germany. *Plant Disease*, *107*(12), 3792–3800. https://doi.org/10.1094/PDIS-04-23-0613-RE

Duduk, B., Stepanović, J., Fránová, J., Zwolińska, A., Rekanović, E., Stepanović, M., Vučković, N., Duduk, N., & Vico, I. (2024). Geographical variations, prevalence, and molecular dynamics of fastidious phloem-limited pathogens infecting sugar beet across Central Europe. *PLOS ONE*, *19*(7), e0306136. https://doi.org/10.1371/journal.pone.0306136

Duduk, N., Ivana V., Andrea K., Jelena S., Živko Ć., Nina V., Emil R., & Bojan D. (2023). A biotroph sets the stage for a necrotroph to play:‘Candidatus Phytoplasma solani’infection of sugar beet facilitated Macrophomina phaseolina root rot. *Frontiers in Microbiology 14*: 1164035. https://doi.org/10.3389/fmicb.2023.1164035

European and Mediterranean Plant Protection Organization. (2025). 'Candidatus Arsenophonus phytopathogenicus' World distribution. *EPPO Global Database*. https://gd.eppo.int/taxon/ARSEPH/distribution

Ferrieri, A. P., Agtuca, B., Appel, H. M., Ferrieri, R. A., & Schultz, J. C. (2013). Temporal changes in allocation and partitioning of new carbon as (11)C elicited by simulated herbivory suggest that roots shape aboveground responses in Arabidopsis. *Plant Physiology*, *161*(2), 692–704. https://doi.org/10.1104/pp.112.208868

Froelich, D. R., Mullendore, D. L., Jensen, K., Ross-Elliott, T. J., Anstead, J. A., Thompson, G. A., Pélissier, H. C., & Knoblauch, M. (2011). Phloem ultrastructure and pressure flow: Sieve-Element-Occlusion-Related agglomerations do not affect translocation. *The Plant Cell*, *23*(12), 4428–4445. https://doi.org/10.1105/tpc.111.093179

Gatineau, F., Jacob N., Vautrin S., Larrue J., Lherminier, J., Richard-Molard, M., & Boudon-Padieu, E. (2002). Association with the Syndrome “Basses Richesses” of Sugar Beet of a Phytoplasma and a Bacterium-Like Organism Transmitted by a Pentastiridius sp. *Phytopathology*, *92*(4), 384–392. https://doi.org/10.1094/PHYTO.2002.92.4.384

Godt, D., & Roitsch, T. (2006). The developmental and organ specific expression of sucrose cleaving enzymes in sugar beet suggests a transition between apoplasmic and symplasmic phloem unloading in the tap roots. *Plant Physiology and Biochemistry*, *44*(11-12), 656–665. https://doi.org/10.1016/j.plaphy.2006.09.019

Gottwald, J. R., Krysan, P. J., Young, J. C., Evert, R. F., & Sussman, M. R. (2000). Genetic evidence for the in planta role of phloem-specific plasma membrane sucrose transporters. *Proceedings of the National Academy of Sciences of the United States of America*, *97*(25), 13979–13984. https://doi.org/10.1073/pnas.250473797

Greenberg, J. T., & Yao, N. (2004). The role and regulation of programmed cell death in plant-pathogen interactions. *Cellular Microbiology*, *6*(3), 201–211. https://doi.org/10.1111/j.1462-5822.2004.00361.x

Gummerson, R. J. (1986). The Effect of Constant Temperatures and Osmotic Potentials on the Germination of Sugar Beet. *Journal of Experimental Botany*, *37*(6), 729–741. https://doi.org/10.1093/jxb/37.6.729

Hardtke, C. S. (2023). Phloem development. *New Phytologist, 293*(3)*, 852–867*. https://doi.org/10.1111/nph.19003

Hennion, N., Durand, M., Vriet, C., Doidy, J., Maurousset, L., Lemoine, R., & Pourtau, N. (2019). Sugars en route to the roots. Transport, metabolism and storage within plant roots and towards microorganisms of the rhizosphere. *Physiologia Plantarum*, *165*(1), 44–57. https://doi.org/10.1111/ppl.12751

Hillnhütter, C., Sikora, R. A., Oerke, E.-C., & van Dusschoten, D. (2012). Nuclear magnetic resonance: A tool for imaging belowground damage caused by Heterodera schachtii and Rhizoctonia solani on sugar beet. *Journal of Experimental Botany*, *63*(1), 319–327. https://doi.org/10.1093/jxb/err273

Hinz, C., Jahnke, S., Metzner, R., Pflugfelder, D., Scheins, J. J., Streun, M., & Koller, R. (2024). Setup and characterisation according to NEMA NU 4 of thephenoPET scanner, a PET system dedicated for plant sciences. *Physics in Medicine and Biology*. 69(5), 055019. https://doi.org/10.1088/1361-6560/ad22a2

Hoffmann, C. M. (2010). Sucrose Accumulation in Sugar Beet Under Drought Stress. *Journal of Agronomy and Crop Science*, *196*(4), 243–252. https://doi.org/10.1111/j.1439-037X.2009.00415.x

Hoffmann, C. M., Koch, H.-J., & Märländer, B. (2021). Sugar beet. In *Crop Physiology Case Histories for Major Crops* (pp. 634–672). Academic Press. https://doi.org/10.1016/B978-0-12-819194-1.00020-7

Imada, S., Tako, Y., Tani, T., Takaku, Y., & Hisamatsu, S. (2017). Translocation and distribution of photosynthetically assimilated ^{13}C to 'Tsugaru' apple fruits. *Journal of Agricultural Meteorology*, *73*(4), 187–194. https://doi.org/10.2480/agrmet.D-17-00014

Jackson, R. B., & Caldwell, M. M. (1992). Shading and the capture of localized soil nutrients: Nutrient contents, carbohydrates, and root uptake kinetics of a perennial tussock grass. *Oecologia*, *91*(4), 457–462. https://doi.org/10.1007/BF00650316

Jahnke, S., Menzel, M. I., van Dusschoten, D., Roeb, G. W., Bühler, J., Minwuyelet, S., Blümler, P., Temperton, V. M., Hombach, T., Streun, M., Beer, S., Khodaverdi, M., Ziemons, K., Coenen, H. H., & Schurr, U. (2009). Combined MRI-PET dissects dynamic changes in plant structures and functions. *The Plant Journal*, *59*(4), 634–644. https://doi.org/10.1111/j.1365-313X.2009.03888.x

Jammer, A., Albacete, A., Schulz, B., Koch, W., Weltmeier, F., van der Graaff, E., Pfeifhofer, H. W., & Roitsch, T. G. (2020). Early-stage sugar beet taproot development is characterized by three distinct physiological phases. *Plant Direct*, *4*(7), e00221. https://doi.org/10.1002/pld3.221

Jensen, K. H., Lee, J., Bohr, T., Bruus, H., Holbrook, N. M., & Zwieniecki, M. A. (2011). Optimality of the Münch mechanism for translocation of sugars in plants. *Journal of the Royal Society, Interface*, *8*(61), 1155–1165. https://doi.org/10.1098/rsif.2010.0578

Joy, K. W. (1964). Translocation in sugar beet: I. Assimilation of 14CO2, and distribution of materials from leaves. *Journal of Experimental Botany*, *15*(45), 485–494.

Jung, B., Ludewig, F., Schulz, A., Meißner, G., Wöstefeld, N., Flügge, U.-I., Pommerrenig, B., Wirsching, P., Sauer, N., Koch, W., Sommer, F., Mühlhaus, T., Schroda, M., Cuin, T. A., Graus, D., Marten, I., Hedrich, R., & Neuhaus, H. E. (2015). Identification of the transporter responsible for sucrose accumulation in sugar beet taproots. *Nature Plants, 1*(1), 1–6. https://doi.org/10.1038/nplants.2014.1

Kais, B., Köhler, J., Werner, P., & Gross, J. (2023). Does the causative agent of Syndrome Basses Richesses (SBR), Candidatus Arsenophonus phytopathogenicus, alter sugar beet phloem composition or plant-emitted volatiles? *IOBC-WPRS Bulletin*, *166*(166), 128–133.

Kaiser, C., Kilburn, M. R., Clode, P. L., Fuchslueger, L., Koranda, M., Cliff, J. B., Solaiman, Z. M., & Murphy, D. V. (2015). Exploring the transfer of recent plant photosynthates to soil microbes: Mycorrhizal pathway vs direct root exudation. *New Phytologist*, *205*(4), 1537–1551. https://doi.org/10.1111/nph.13138

Kakouridis, A., Yuan, M., Nuccio, E. E., Hagen, J. A., Fossum, C. A., Moore, M. L., Estera-Molina, K. Y., Nico, P. S., Weber, P. K., Pett-Ridge, J., & Firestone, M. K. (2024). Arbuscular mycorrhiza convey significant plant carbon to a diverse hyphosphere microbial food web and mineral-associated organic matter. *The New Phytologist. 242*(4), 1661–1675. https://doi.org/10.1111/nph.19560

Karve, A. A., Alexoff, D., Kim, D., Schueller, M. J., Ferrieri, R. A., & Babst, B. A. (2015). In vivo quantitative imaging of photoassimilate transport dynamics and allocation in large plants using a commercial positron emission tomography (PET) scanner. *BMC Plant Biology*, *15*(1), 273. https://doi.org/10.1186/s12870-015-0658-3

Kebrom, T. H. (2024). Shade signals activate distinct molecular mechanisms that induce dormancy and inhibit flowering in vegetative axillary buds of sorghum. *Plant Direct*, *8*(8), e626. https://doi.org/10.1002/pld3.626

Keller I., Metzner R., Huber G., Pflugfelder D., & Koller R. (unpublished). Plasticity of carbon distribution in sugar beet (Beta vulgaris) taproots using combined MRI and PET-approach [Unpublished project report]. Enabling Technologies, IBG-2, Forschungszentrum Jülich

Kenter, C., Hoffmann, C. M., & Märländer, B. (2006). Effects of weather variables on sugar beet yield development (Beta vulgaris L.). *European Journal of Agronomy*, *24*(1), 62–69. https://doi.org/10.1016/j.eja.2005.05.001

Kim, D., Alexoff, D. L., Schueller, M., Babst, B., Ferrieri, R., Fowler, J. S., & Schlyer, D. J. (2014). The design and performance of a portable handheld (11)CO2 delivery system. *Applied Radiation and Isotopes : Including Data, Instrumentation and Methods for Use in Agriculture, Industry and Medicine*, *94*, 338–343. https://doi.org/10.1016/j.apradiso.2014.09.008

Kleuker, G., & Hoffmann, C. M. (2021). Tissue strength of sugar beet root genotypic variation and environmental impact. *Crop Science*, *61*(4), 2478–2488. https://doi.org/10.1002/csc2.20523

Kreitzer, C., Stepanović, J., Stanojević, N., Rohringer, A., Seiter, M., Rekanović, E., & Duduk, B. (2025). Dominant cixiid vector and transmission of 'Candidatus Arsenophonus phytopathogenicus' and 'Candidatus Phytoplasma solani'-related strain 16SrXII-P in sugar beet in Austria. *Scientific Reports*, *15*(1), 22526. https://doi.org/10.1038/s41598-025-07035-0

Lang, C., Dettweiler, A., Benaouda, S., Kreimer, D., Löffler, D., Glaser, E., Adam, H., Bojanowicz, S. L., Schall, E., Stohl, J., Göbbels, H., Lenz, M., Witczak, N., Ritz, J., & Pfitzner, H. (2025). Pentastiridius leporinus as a plant disease vector: The practical state of knowlege and derived research objectives. *Sugar Industry International*, 105–120. https://doi.org/10.36961/si33023

Lanzrath, H., Lieres, E. von, Metzner, R., & Huber, G. (2025). Analyzing time activity curves from spatio-temporal tracer data to determine tracer transport velocity in plants. *Mathematical Biosciences*, 109430. https://doi.org/10.1016/j.mbs.2025.109430

Launay, M., Graux, A.-I., Brisson, N., & Guerif, M. (2009). Carbohydrate remobilization from storage root to leaves after a stress release in sugar beet (Beta vulgaris L.): experimental and modelling approaches. *The Journal of Agricultural Science*, *147*(6), 669–682. https://doi.org/10.1017/S0021859609990116

Lazar, T. (2003). In: Taiz, L. & Zeiger, E. Plant physiology. 3rd edn. *Annals of Botany*, *91*(6), 750–751. https://doi.org/10.1093/aob/mcg079

Lewis, J. D., Knoblauch, M., & Turgeon, R. (2022). The Phloem as an Arena for Plant Pathogens. *Annual Review of Phytopathology*, *60*, 77–96. https://doi.org/10.1146/annurev-phyto-020620-100946

Liu, D. D., Chao, W. M., & Turgeon, R. (2012). Transport of sucrose, not hexose, in the phloem. *Journal of Experimental Botany*, *63*(11), 4315–4320. https://doi.org/10.1093/jxb/ers127

Mahillon, M., Bussereau, F., Dubuis, N., Brodard, J., Debonneville, C., & Schumpp, O. (2025). First Detection of Arsenophonus in Potato Crop in Switzerland: A Threat for the Processing Industry? *Potato Research*, 1–12. https://doi.org/10.1007/s11540-024-09840-y

Mahillon, M., Groux, R., Bussereau, F., Brodard, J., Debonneville, C., Demal, S., Kellenberger, I., Peter, M., Steinger, T., & Schumpp, O. (2022). Virus Yellows and Syndrome "Basses Richesses" in Western

Switzerland: A Dramatic 2020 Season Calls for Urgent Control Measures. *Pathogens*, *11*(8), 885. https://doi.org/10.3390/pathogens11080885

Malinowski, R., Singh, D., Kasprzewska, A., Blicharz, S., & Basińska-Barczak, A. (2024). Vascular tissue - boon or bane? How pathogens usurp long-distance transport in plants and the defence mechanisms deployed to counteract them. *The New Phytologist*, *243*(6), 2075–2092. https://doi.org/10.1111/nph.20030

Märländer, B., Hoffmann, C., Koch, H.-J., Ladewig, E., Merkes, R., Petersen, J., & Stockfisch, N. (2003). Environmental Situation and Yield Performance of the Sugar Beet Crop in Germany: Heading for Sustainable Development. *Journal of Agronomy and Crop Science*, *189*(4), 201–226. https://doi.org/10.1046/j.1439-037X.2003.00035.x

Metzner, R., Chlubek, A., Bühler, J., Pflugfelder, D., Schurr, U., Huber, G., Koller, R., & Jahnke, S. (2022). In Vivo Imaging and Quantification of Carbon Tracer Dynamics in Nodulated Root Systems of Pea Plants. *Plants*, *11*(5), 632. https://doi.org/10.3390/plants11050632

Metzner, R., van Dusschoten, D., Bühler, J., Schurr, U., & Jahnke, S. (2014). Belowground plant development measured with magnetic resonance imaging (MRI): Exploiting the potential for non-invasive trait quantification using sugar beet as a proxy. *Frontiers in Plant Science*, *5*, 469. https://doi.org/10.3389/fpls.2014.00469

Milford, G.F.J. (1973). The growth and development of the storage root of sugar beet. *Annals of Applied Biology*(75), 427–438.

Minchin, P. E. H., & Thorpe, M. R. (2003). Using the short-lived isotope 11C in mechanistic studies of photosynthate transport. *Functional Plant Biology*, *30*(8), 831–841. https://doi.org/10.1071/FP03008

Misra, V., & Shrivastava, A. K. (2022). Understanding the sugar beet crop and its physiology. In: *Sugar Beet Cultivation, Management and Processing* (pp. 11-25). Singapore: Springer Nature Singapore. https://doi.org/10.1007/978-981-19-2730-0_2

Miyoshi, Y., Soma, F., Yin, Y.-G., Suzui, N., Noda, Y., Enomoto, K., Nagao, Y., Yamaguchi, M., Kawachi, N., Yoshida, E., Tashima, H., Yamaya, T., Kuya, N., Teramoto, S., & Uga, Y. (2022). Rice immediately adapts the dynamics of photosynthates translocation to roots in response to changes in soil water environment. *Frontiers in Plant Science*, *13*, 1024144. https://doi.org/10.3389/fpls.2022.1024144

Muller, O., Cohu, C. M., Stewart, J. J., Protheroe, J. A., Demmig-Adams, B., & Adams, W. W. (2014). Association between photosynthesis and contrasting features of minor veins in leaves of summer

annuals loading phloem via symplastic versus apoplastic routes. *Physiologia Plantarum*, *152*(1), 174–183. https://doi.org/10.1111/ppl.12155

Münch, E. (1930). Die Stoffbewegungen in der Pflanze.

Nieberl, P., Ehrl, C., Pommerrenig, B., Graus, D., Marten, I., Jung, B., Ludewig, F., Koch, W., Harms, K., Flügge, U.-I., Neuhaus, H. E., Hedrich, R., & Sauer, N. (2017). Functional characterisation and cell specificity of BvSUT 1, the transporter that loads sucrose into the phloem of sugar beet (*Beta vulgaris* L.) source leaves. *Plant biology*, *19*(3), 315-326. https://doi.org/10.1111/plb.12546

OECD/ FAO. (2025). *OECD-FAO agricultural outlook 2025–2034,* Paris and Rome. https://doi.org/10.1787/601276cd-en

Orians, C. M., & Jones, C. G. (2001). Plants as resource mosaics: a functional model for predicting patterns of within-plant resource heterogeneity to consumers based on vascular architecture and local environmental variability. *Oikos*, *94*(3), 493–504. https://doi.org/10.1034/j.1600-0706.2001.940311.x

Paine, C. E. T., Stenflo, M., Philipson, C. D., Saner, P., Bagchi, R., Ong, R. C., & Hector, A. (2012). Differential growth responses in seedlings of ten species of Dipterocarpaceae to experimental shading and defoliation. *Journal of Tropical Ecology*, *28*(4), 377–384. https://doi.org/10.1017/S0266467412000326

Patrick, J. W., & Offler, C. E. (1996). Post-sieve element transport of photoassimilates in sink regions. *Journal of Experimental Botany*, *47*, 1165–1177. https://doi.org/10.1093/jxb/47.Special_Issue.1165

Pfaehler, E., Pflugfelder, D., & Scharr, H. (2025). Untrained perceptual loss for image denoising of line-like structures in MR images. *PLOS ONE*, *20*(2), e0318992. https://doi.org/10.1371/journal.pone.0318992

Pfitzer, R., Rostás, M., Häußermann, P., Häuser, T., Rinklef, A., Detring, J., Schrameyer, K., Voegele, R. T., Maier, J., & Varrelmann, M. (2024). Effects of succession crops and soil tillage on suppressing the syndrome 'basses richesses' vector Pentastiridius leporinus in sugar beet. *Pest Management Science*, *80*(7), 3379– 3388. https://doi.org/10.1002/ps.8041

Pfitzer, R., Varrelmann, M., Schrameyer, K., & Rostás, M. (2022). Life history traits and a method for continuous mass rearing of the planthopper Pentastiridius leporinus, a vector of the causal agent of syndrome 'basses richesses' in sugar beet. *Pest Management Science*, *78*(11), 4700–4708. https://doi.org/10.1002/ps.7090

Pflugfelder, D., Metzner, R., van Dusschoten, D., Reichel, R., Jahnke, S., & Koller, R. (2017). Non-invasive imaging of plant roots in different soils using magnetic resonance imaging (MRI). *Plant Methods*, *13*(1), 102. https://doi.org/10.1186/s13007-017-0252-9

Qu, W., Robert, C. A. M., Erb, M., Hibbard, B. E., Paven, M., Gleede, T., Riehl, B., Kersting, L., Cankaya, A. S., Kunert, A. T., Xu, Y., Schueller, M. J., Shea, C., Alexoff, D., Lee, S. J., Fowler, J. S., & Ferrieri, R. A. (2016). Dynamic Precision Phenotyping Reveals Mechanism of Crop Tolerance to Root Herbivory. *Plant Physiology*, *172*(2), 776–788. https://doi.org/10.1104/pp.16.00735

Reyer, A., Bazihizina, N., Jaślan, J., Scherzer, S., Schäfer, N., Jaślan, D., Becker, D., Müller, T. D., Pommerrenig, B., Neuhaus, H. E., Marten, I., & Hedrich, R. (2024). Sugar beet PMT5a and STP13 carriers suitable for proton-driven plasma membrane sucrose and glucose import in taproots. *The Plant Journal. 118*(6), 2219–2232. https://doi.org/10.1111/tpj.16740

Rinklef, A., Behrmann, S. C., Löffler, D., Erner, J., Meyer, M. V., Lang, C., Vilcinskas, A., & Lee, K.-Z. (2024). Prevalence in Potato of 'Candidatus Arsenophonus Phytopathogenicus' and 'Candidatus Phytoplasma Solani' and Their Transmission via Adult Pentastiridius leporinus. *Insects*, *15*(4), 275. https://doi.org/10.3390/insects15040275

Rodrigues, C. M., Müdsam, C., Keller, I., Zierer, W., Czarnecki, O., Corral, J. M., Reinhardt, F., Nieberl, P., Fiedler-Wiechers, K., Sommer, F., Schroda, M., Mühlhaus, T., Harms, K., Flügge, U.-I., Sonnewald, U., Koch, W., Ludewig, F., Neuhaus, H. E., & Pommerrenig, B. (2020). Vernalization Alters Sink and Source Identities and Reverses Phloem Translocation from Taproots to Shoots in Sugar Beet. *The Plant Cell*, *32*(10), 3206–3223. https://doi.org/10.1105/tpc.20.00072

Ross-Elliott, T. J., Jensen, K. H., Haaning, K. S., Wager, B. M., Knoblauch, J., Howell, A. H., Mullendore, D. L., Monteith, A. G., Paultre, D., Yan, D., Otero, S., Bourdon, M., Sager, R., Lee, J.-Y., Helariutta, Y., Knoblauch, M., & Oparka, K. J. (2017). Phloem unloading in *Arabidopsis* roots is convective and regulated by the phloem–pericycle. *eLife, 6*, e24125. https://doi.org/10.7554/eLife.24125.002

Rossi, V., Meriggi, P., Biancardi, E. & Rosso, F. (2000). Effect of Cercospora leaf spot on sugar beet growth, yield and quality. In: M. J. C. Asher, B. Holtschulte, M. R. Molard, F. Rosso, G. Steinrücken, & R. Beckers (Eds), *IIRB Advances in Sugar Beet Research 2: Cercospora beticola Sacc*. *– Biology, agronomic influence and control measures in sugar beet*. (pp. 49-76) Advances in Sugar beet Research.

Santi, S., Marco, F. de, Polizzotto, R., Grisan, S., & Musetti, R. (2013). Recovery from stolbur disease in grapevine involves changes in sugar transport and metabolism. *Frontiers in Plant Science*, *4*, 171. https://doi.org/10.3389/fpls.2013.00171

Schaefferkoetter, J., Yan, J., Ortega, C., Sertic, A., Lechtman, E., Eshet, Y., Metser, U., & Veit-Haibach, P. (2020). Convolutional neural networks for improving image quality with noisy PET data. *EJNMMI Research*, *10*(1), 105. https://doi.org/10.1186/s13550-020-00695-1

Schepper, V. de, Bühler, J., Thorpe, M., Roeb, G., Huber, G., van Dusschoten, D., Jahnke, S., & Steppe, K. (2013). (11)C-PET imaging reveals transport dynamics and sectorial plasticity of oak phloem after girdling. *Frontiers in Plant Science*, *4*, 200. https://doi.org/10.3389/fpls.2013.00200

Schepper, V. de, Swaef, T. de, Bauweraerts, I., & Steppe, K. (2013). Phloem transport: A review of mechanisms and controls. *Journal of Experimental Botany*, *64*(16), 4839–4850. https://doi.org/10.1093/jxb/ert302

Schmidt, M., Bühler, J., Habbel, D., & Metzner, R. (2024). FZJ TAC-ROI-TOOL. 10.5281/zenodo.12664701

Schmitt, A., Pausch, J., & Kuzyakov, Y. (2013). Effect of clipping and shading on C allocation and fluxes in soil under ryegrass and alfalfa estimated by 14C labelling. *Applied Soil Ecology*, *64*, 228–236. https://doi.org/10.1016/j.apsoil.2012.12.015

Schmittgen, S., Metzner, R., van Dusschoten, D., Jansen, M., Fiorani, F., Jahnke, S., Rascher, U., & Schurr, U. (2015). Magnetic resonance imaging of sugar beet taproots in soil reveals growth reduction and morphological changes during foliar Cercospora beticola infestation. *Journal of Experimental Botany*, *66*(18), 5543–5553. https://doi.org/10.1093/jxb/erv109

Schultes, S. R., Rüger, L., Niedeggen, D., Freudenthal, J., Frindte, K., Becker, M. F., Metzner, R., Pflugfelder, D., Chlubek, A., Hinz, C., van Dusschoten, D., Bauke, S. L., Bonkowski, M., Watt, M., Koller, R., & Knief, C. (2025). Photosynthate distribution determines spatial patterns in the rhizosphere microbiota of the maize root system. *Nature Communications*, *16*(1), 7286. https://doi.org/10.1038/s41467-025-62550-y

Schwachtje, J., Minchin, P. E. H., Jahnke, S., van Dongen, J. T., Schittko, U., & Baldwin, I. T. (2006). Snf1-related kinases allow plants to tolerate herbivory by allocating carbon to roots. *Proceedings of the National Academy of Sciences of the United States of America*, *103*(34), 12935–12940. https://doi.org/10.1073/pnas.0602316103

Sémétey, O., Bressan, A., Richard-Molard, M., & Boudon-Padieu, E. (2007). Monitoring of proteobacteria and phytoplasma in sugar beets naturally or experimentally affected by the disease syndrome

'Basses richesses'. *European Journal of Plant Pathology*, *117*(2), 187–196. https://doi.org/10.1007/s10658-006-9087-3

Simko, I., Jimenez-Berni, J. A., & Sirault, X. R. R. (2017). Phenomic Approaches and Tools for Phytopathologists. *Phytopathology*, *107*(1), 6–17. https://doi.org/10.1094/PHYTO-02-16-0082-RVW

Statista. (2023). *Production of sugar beet worldwide from 2010 to 2022*. https://www.statista.com/statistics/264694/global-sugar-beet-production/

Stieber, J., & Beringer, H. (1984). Dynamic and structural relationships among leaves, roots, and storage tissue in the sugar beet. *Botanical Gazette*, *145*(4), 465–473.

Suwa, R., Fujimaki, S., Suzui, N., Kawachi, N., Ishii, S., Sakamoto, K., Nguyen, N. T., Saneoka, H., Mohapatra, P. K., Moghaieb, R. E., Matsuhashi, S., & Fujita, K. (2008). Use of positron-emitting tracer imaging system for measuring the effect of salinity on temporal and spatial distribution of 11C tracer and coupling between source and sink organs. *Plant Science*, *175*(3), 210–216. https://doi.org/10.1016/j.plantsci.2008.03.022

Tatineni, S., Sagaram, U. S., Gowda, S., Robertson, C. J., Dawson, W. O., Iwanami, T., & Wang, N. (2008). In Planta Distribution of 'Candidatus Liberibacter asiaticus' as Revealed by Polymerase Chain Reaction (PCR) and Real-Time PCR. *Phytopathology*, *98*(5), 592–599. https://doi.org/10.1094/PHYTO-98-5-0592

Therhaag, E., Schneider, B., Zikeli, K., Maixner, M., & Gross, J. (2024). Pentastiridius leporinus (Linnaeus, 1761) as a Vector of Phloem-Restricted Pathogens on Potatoes: 'candidatus Arsenophonus Phytopathogenicus' and 'Candidatus Phytoplasma Solani'. *Insects*, *15*(3), 189. https://doi.org/10.3390/insects15030189

Trebbi, D., & McGrath, J. M. (2009). Functional differentiation of the sugar beet root system as indicator of developmental phase change. *Physiologia Plantarum*, *135*(1), 84–97. https://doi.org/10.1111/j.1399-3054.2008.01169.x

van Bel, A. J. E. (1993). Strategies of Phloem Loading. *Annual Review of Plant Physiology. Molecular Biology*, *44*, 253–281.

van Dusschoten, D., Metzner, R., Kochs, J., Postma, J. A., Pflugfelder, D., Bühler, J., Schurr, U., & Jahnke, S. (2016). Quantitative 3D Analysis of Plant Roots Growing in Soil Using Magnetic Resonance Imaging. *Plant Physiology*, *170*(3), 1176–1188. https://doi.org/10.1104/pp.15.01388

Vargas-Ortiz, E., Espitia-Rangel, E., Tiessen, A., & Délano-Frier, J. P. (2013). Grain amaranths are defoliation tolerant crop species capable of utilizing stem and root carbohydrate reserves to

sustain vegetative and reproductive growth after leaf loss. *PLOS ONE*, *8*(7), e67879. https://doi.org/10.1371/journal.pone.0067879

Vaughn, M. W., Harrington, G. N., & Bush, D. R. (2002). Sucrose-mediated transcriptional regulation of sucrose symporter activity in the phloem. *Proceedings of the National Academy of Sciences*, *99*(16), 10876-10880. https://pmc.ncbi.nlm.nih.gov/articles/PMC125066/

White, A. C., Rogers, A., Rees, M., & Osborne, C. P. (2016). How can we make plants grow faster? A source-sink perspective on growth rate. *Journal of Experimental Botany*, *67*(1), 31–45. https://doi.org/10.1093/jxb/erv447

Windt, C. W., Vergeldt, F. J., Jager, P. A. de, & van As, H. (2006). Mri of long-distance water transport: A comparison of the phloem and xylem flow characteristics and dynamics in poplar, castor bean, tomato and tobacco. *Plant, Cell & Environment*, *29*(9), 1715–1729. https://doi.org/10.1111/j.1365-3040.2006.01544.x

Witczak, N., Benaouda, S., Wahl, F., Göbbels, H., Lang, C., Jarausch, B., & Maixner, M. (2025). Carrot (Daucus carota L.) as Host for Pentastiridius leporinus and Phloem-Restricted Pathogens in Germany. *Biology*, *14*(9), 1152. https://doi.org/10.3390/biology14091152

Wyse, R. (1980). Partitioning within the Taproot Sink of Sugarbeet: Effect of Photosaynthate Supply1. *Crop Science*, *20*(2), 256–258.

Yu, P., Li, C, Li, M., He, X., Wang, D., Li, H., Marcon, C., Li, Y., Perez-Limón, S., Chen, X., Delgado-Baquerizo, M., Koller, R., Metzner, R., van Dusschoten, D., Pflugfelder, D., Borisjuk, L., Plutenko, I., Mahon, A., Resende, M. F. R., . . . Hochholdinger, F. (2024). Seedling root system adaptation to water availability during maize domestication and global expansion. *Nature Genetics*, *56*(6), 1245–1256. https://doi.org/10.1038/s41588-024-01761-3

Zamski, E., & Azenkot, A. (1981). Sugarbeet Vasculature. I. Cambial Development and the Three-Dimensional Structure of the Vascular System. *Botanical Gazette*, *142*, 334–343.

Zhang, Y.-F., Li, G.-L., Wang, X.-F., Sun, Y.-Q., & Zhang, S.-Y. (2017). Transcriptomic profiling of taproot growth and sucrose accumulation in sugar beet (Beta vulgaris L.) at different developmental stages. *PLOS ONE*, *12*(4), e0175454. https://doi.org/10.1371/journal.pone.0175454

Zierer, W., Fritzler, M., Chiu, T. J., Anjanappa, R. B., Chang, S.-H., Metzner, R, Quiros, J., Lamm, C. E., Thieme, M., Koller, R., Huber, G., Muller, O., Rascher, U., Sonnewald, U., Neuhaus, H. E., Gruissem, W., & Bellin, L. (2025). A non-rectifying potassium channel increases cassava drought tolerance and storage root yield. *BioRxiv*, 2025.05.26.655271. https://doi.org/10.1101/2025.05.26.655271

Zübert, C., & Kube, M. (2021). Application of TaqMan Real-Time PCR for Detecting 'Candidatus Arsenophonus Phytopathogenicus' Infection in Sugar Beet. *Pathogens*, *10*(11). https://doi.org/10.3390/pathogens10111466

Appendix A: Supplementary materials for Chapter 2

Figure A. S1. Approximate positions for taproot cross-sectioning.

Figure A. S2-S12. Cross-sectional anatomical features of control taproot samples C2-C12.

Figure A. S13-S19. Cross-sectional anatomical features of diseased taproot samples D2-D8.

Figure A. S20-S22. Tracer distribution within taproot for control samples C2-C4.

Figure A. S23. Tracer distribution within taproot for diseased sample D2.

Table A. S1. Primers and probe for detection of 'Ca. A. phytopathogenicus'.

Table A. S2. Mean Cq values after qPCR.

Table A. S3. Heterogeneity of tracer distribution within taproots.

Table A. S4. Taproot diameter and fresh weight after harvest.

Video A. S1. Arrival and distribution of tracer in control taproot C1.

Video A. S2. Arrival and distribution of tracer in diseased taproot D1.

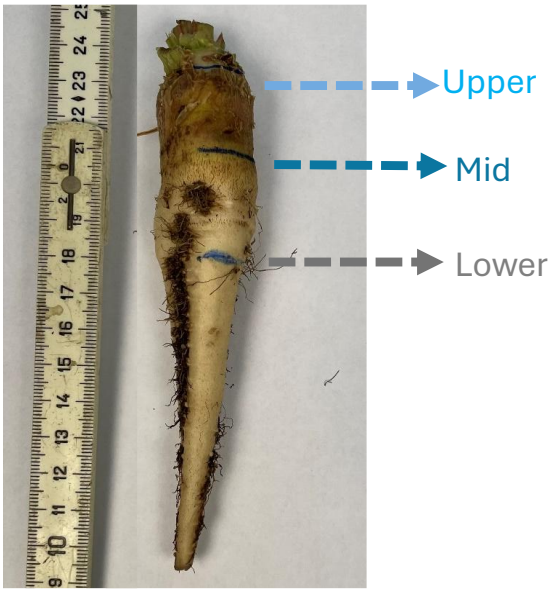

Figure A. S1. Approximate positions for cross-sectional slicing, RGB imaging and sample taking for qPCR during destructive analysis.

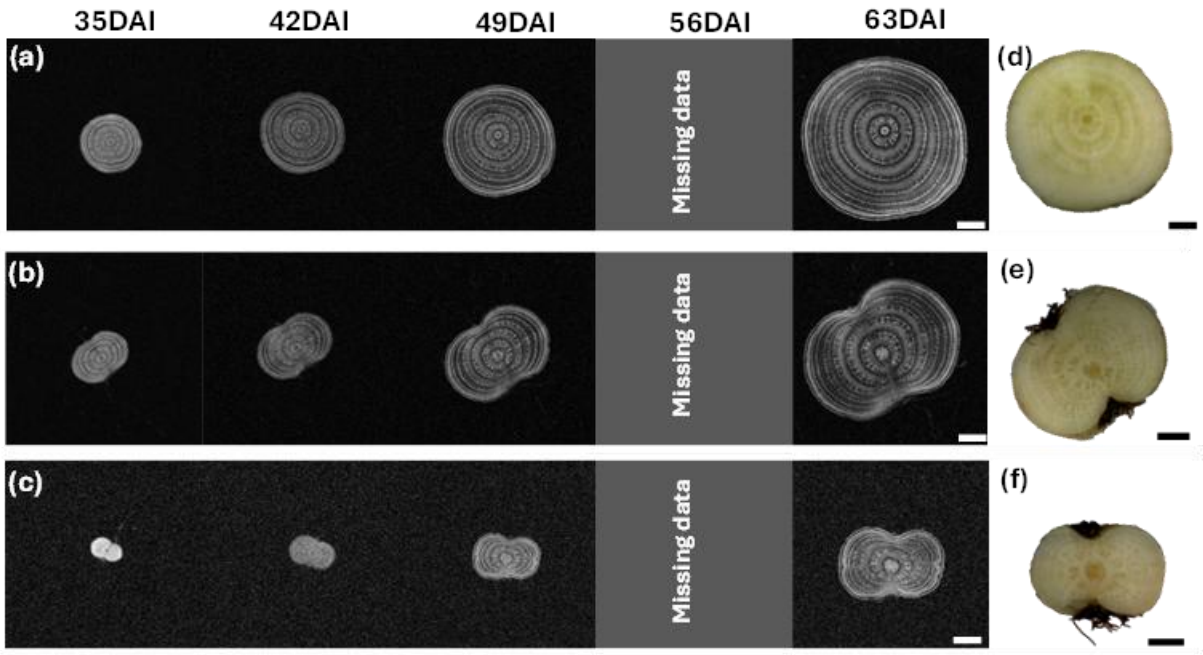

Figure A. S2. Cross-sectional anatomical features of control sample C2. (A-C) MRI and (D-F) RBG images for upper (A,D), middle (B,E) and lower (C,F) taproot slices. Scale bar, 0.5 cm.

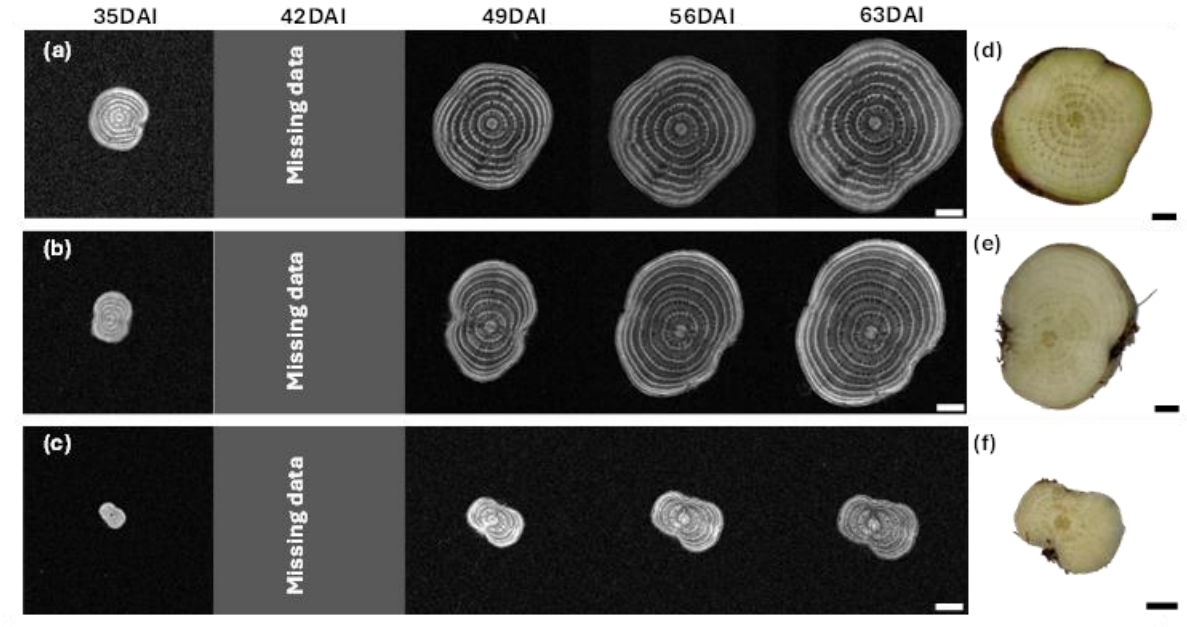

Figure A. S3. Cross-sectional anatomical features of control sample C3. (A-C) MRI and (D-F) RBG images for upper (A,D), middle (B,E) and lower (C,F) taproot slices. Scale bar, 0.5 cm.

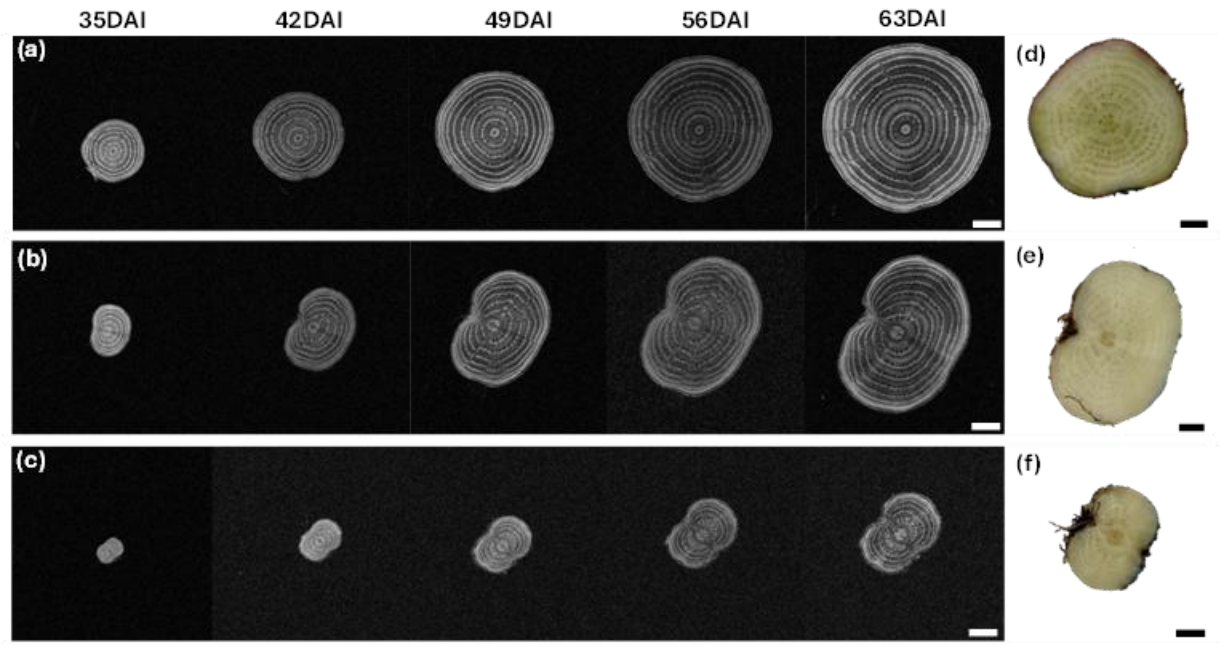

Figure A. S4. Cross-sectional anatomical features of control sample C4. (A-C) MRI and (D-F) RBG images for upper (A,D), middle (B,E) and lower (C,F) taproot slices. Scale bar, 0.5 cm.

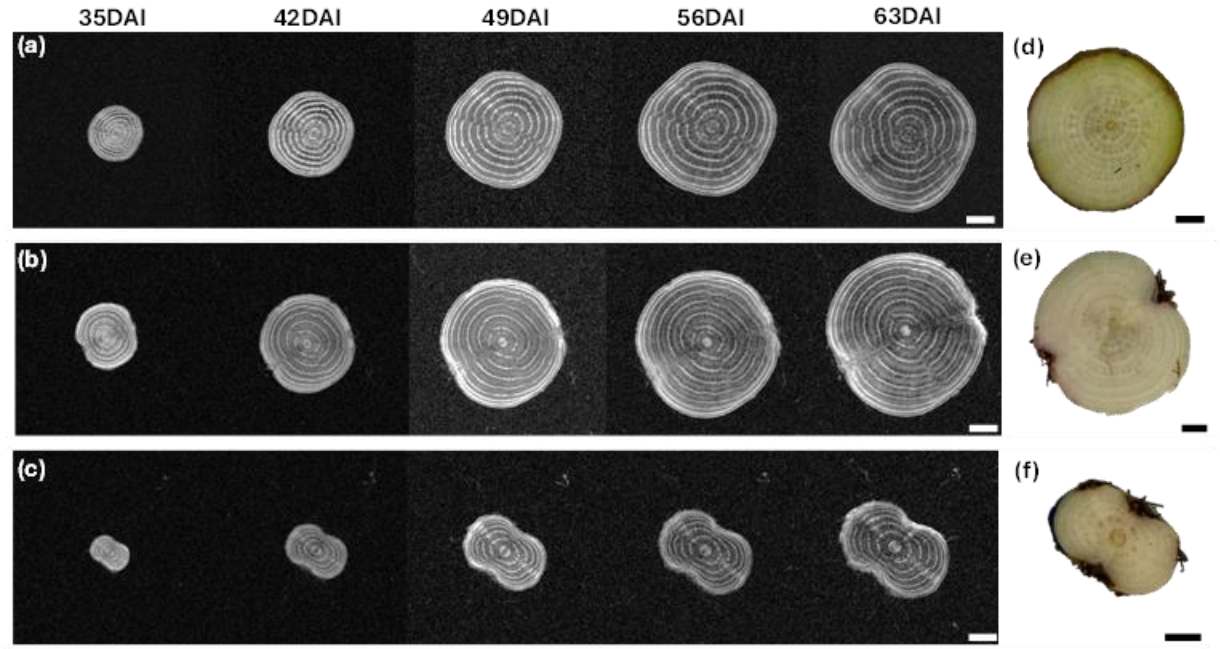

Figure A. S5. Cross-sectional anatomical features of control sample C5. (A-C) MRI and (D-F) RBG images for upper (A,D), middle (B,E) and lower (C,F) taproot slices. Scale bar, 0.5 cm.

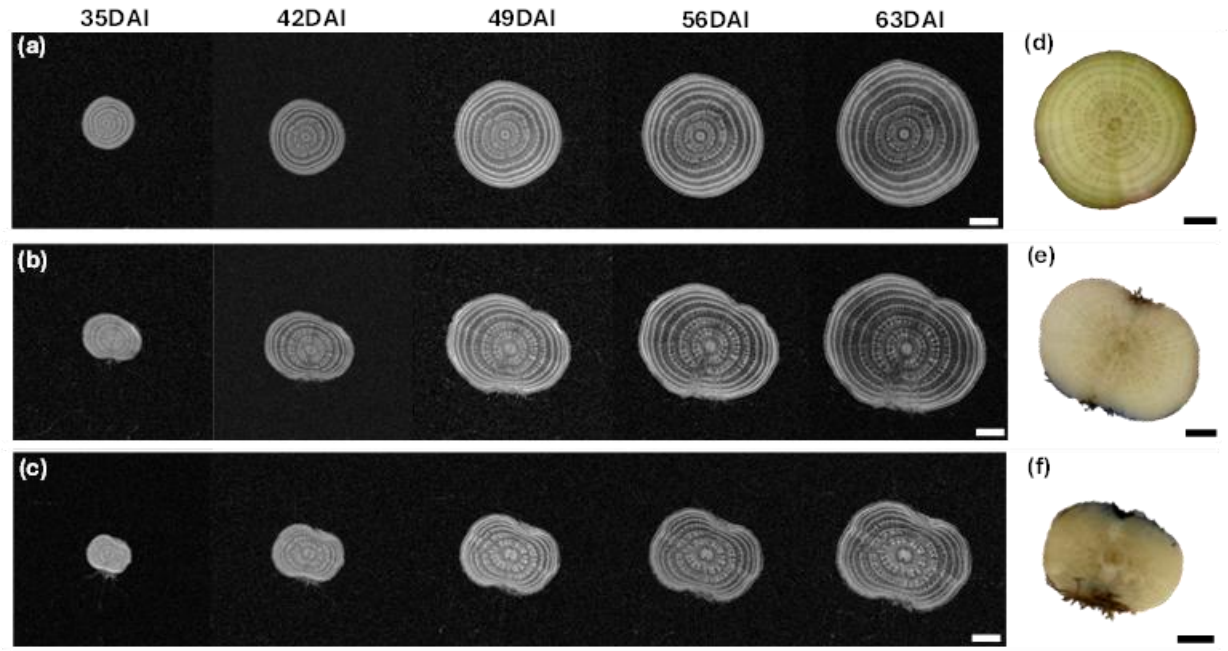

Figure A. S6. Cross-sectional anatomical features of control sample C6. (A-C) MRI and (D-F) RBG images for upper (A,D), middle (B,E) and lower (C,F) taproot slices. Scale bar, 0.5

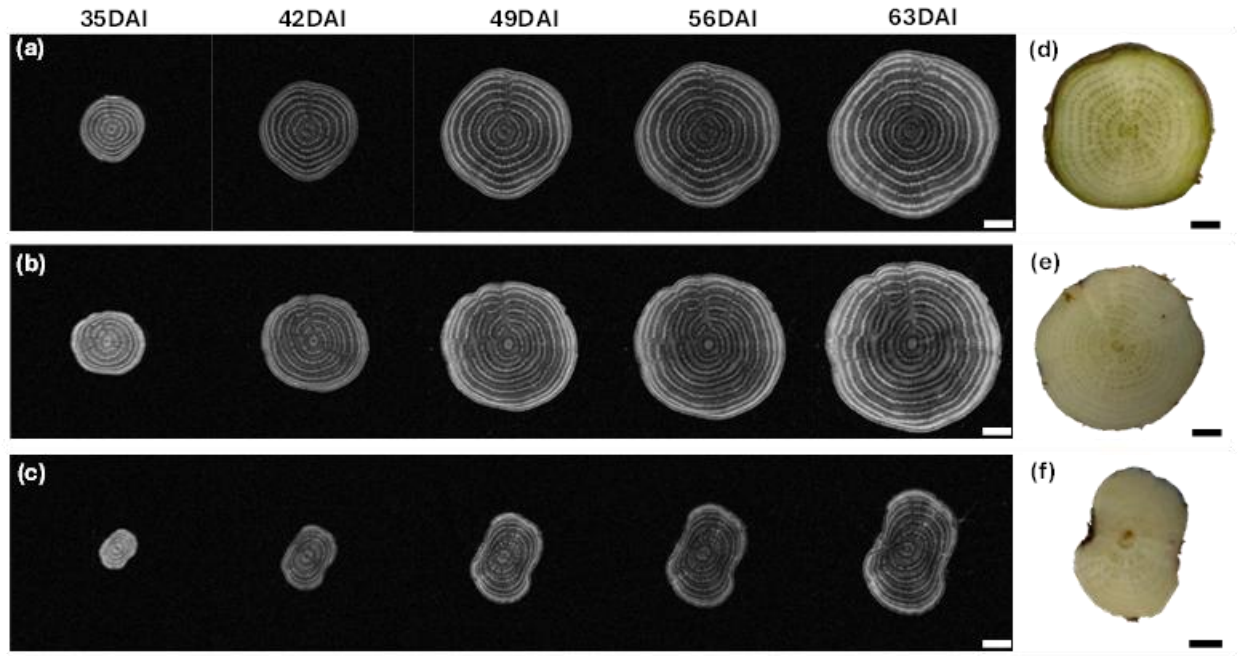

Figure A. S7. Cross-sectional anatomical features of control sample C7. (A-C) MRI and (D-F) RBG images for upper (A,D), middle (B,E) and lower (C,F) taproot slices. Scale bar, 0.5 cm.

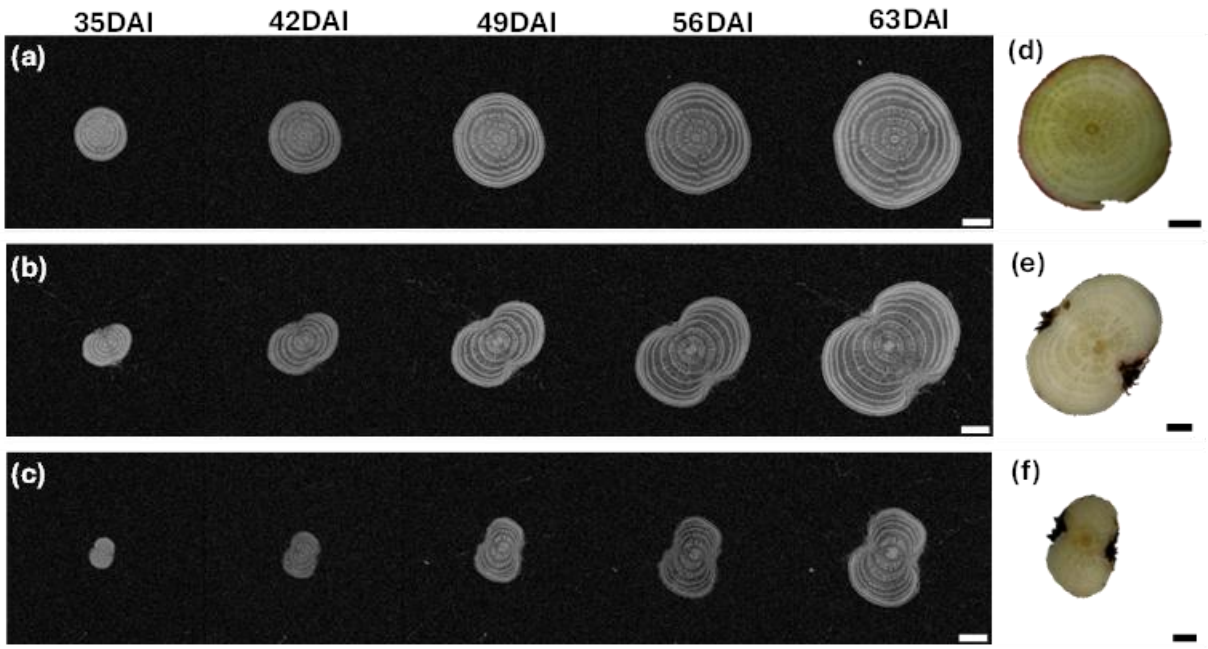

Figure A. S8. Cross-sectional anatomical features of control sample C8. (A-C) MRI and (D-F) RBG images for upper (A,D), middle (B,E) and lower (C,F) taproot slices. Scale bar, 0.5 cm.

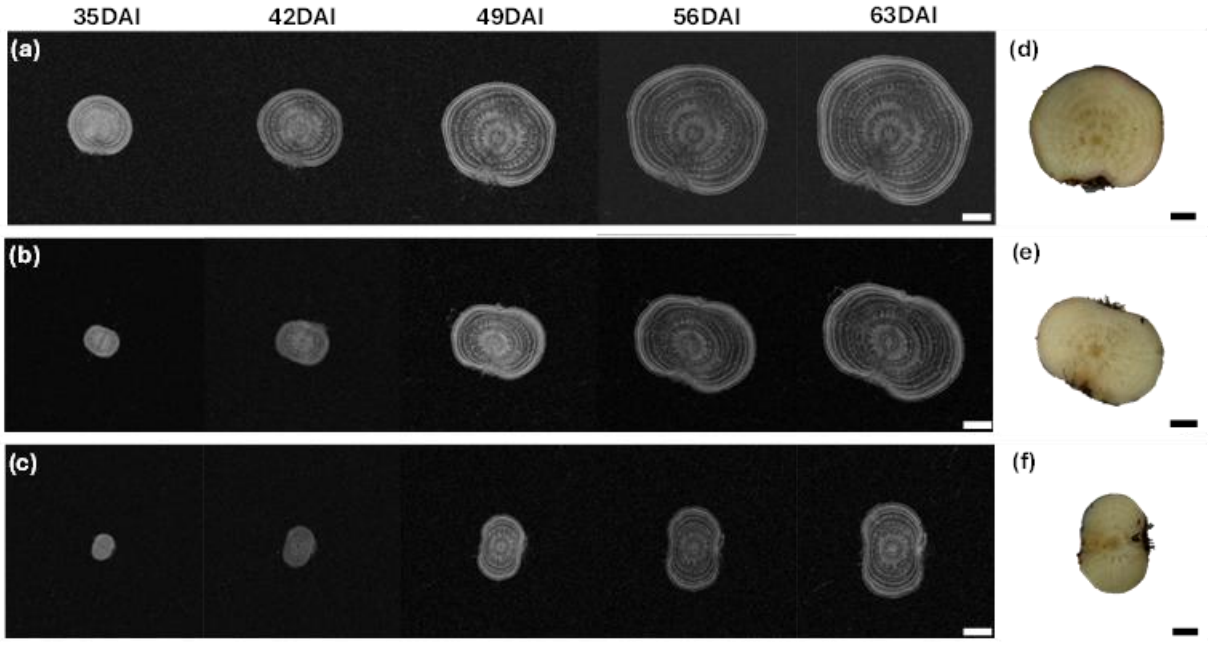

Figure A. S9. Cross-sectional anatomical features of control sample C9. (A-C) MRI and (D-F) RBG images for upper (A,D), middle (B,E) and lower (C,F) taproot slices. Scale bar, 0.5 cm.

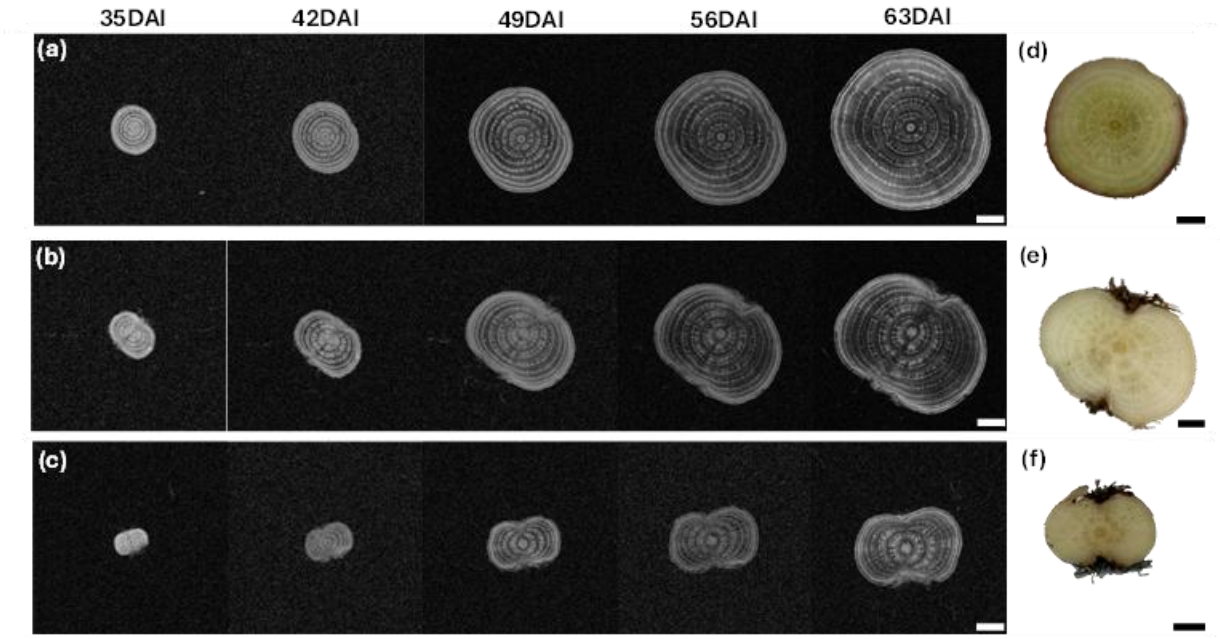

Figure A. S10. Cross-sectional anatomical features of control sample C10. (A-C) MRI and (D-F) RBG images for upper (A,D), middle (B,E) and lower (C,F) taproot slices. Scale bar, 0.5 cm.

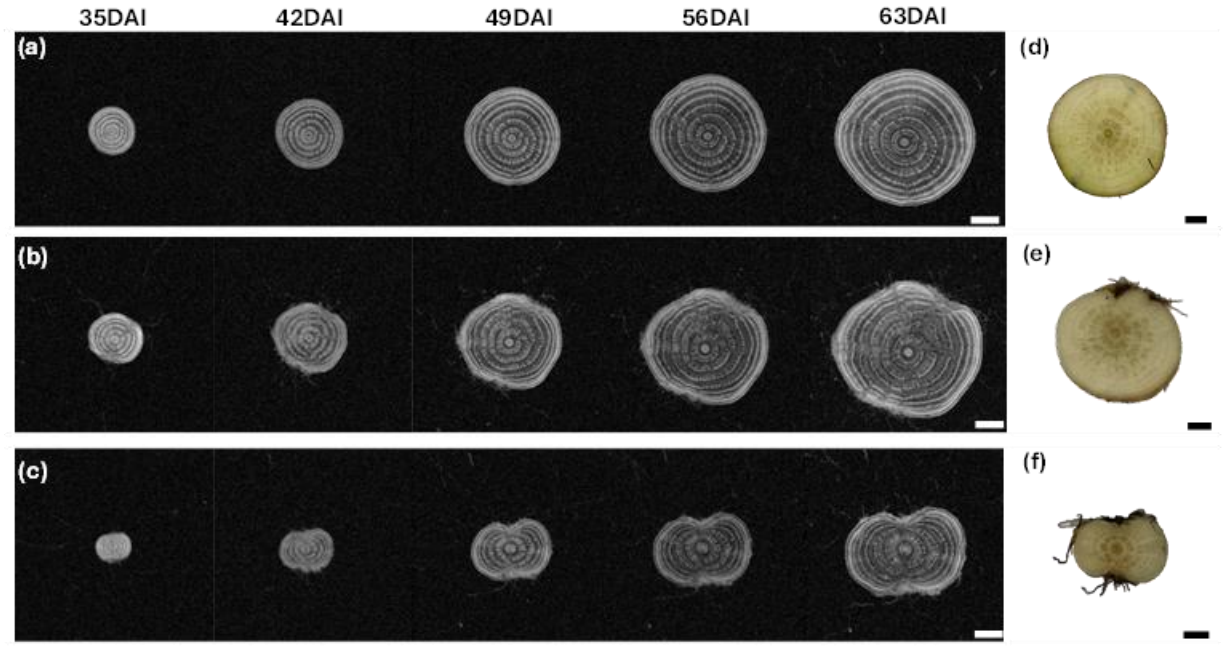

Figure A. S11. Cross-sectional anatomical features of control sample C11. (A-C) MRI and (D-F) RBG images for upper (A,D), middle (B,E) and lower (C,F) taproot slices. Scale bar, 0.5 cm

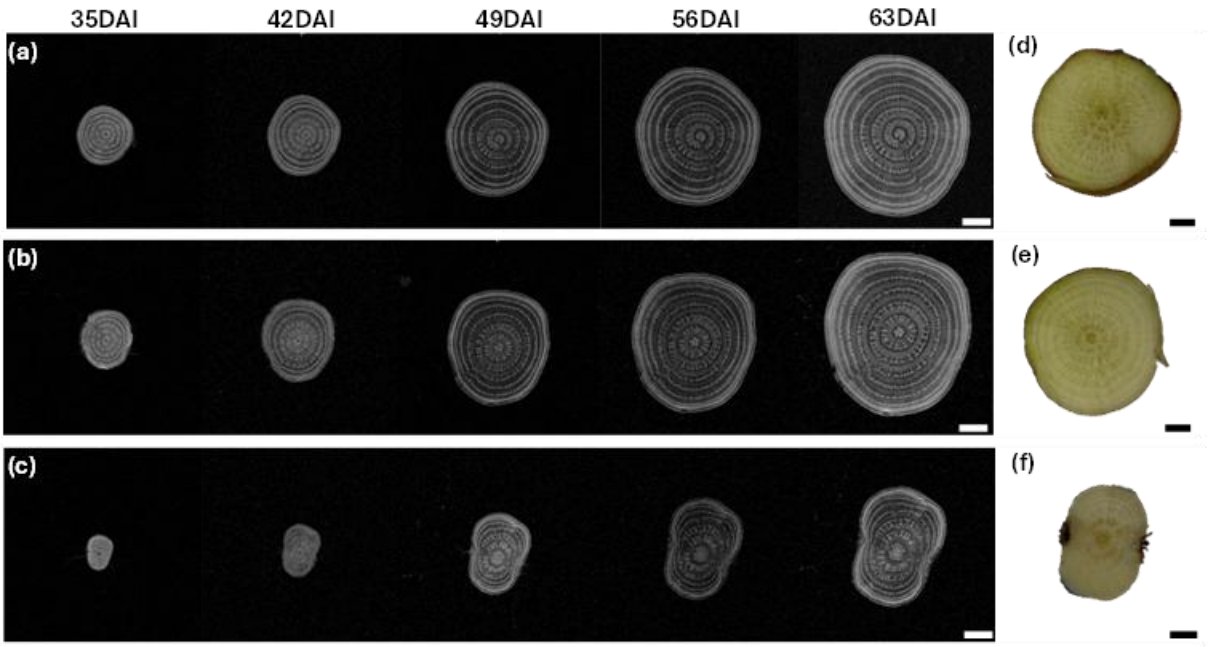

Figure A. S12. Cross-sectional anatomical features of control sample C12. (A-C) MRI and (D-F) RBG images for upper (A,D), middle (B,E) and lower (C,F) taproot slices. Scale bar, 0.5 cm.

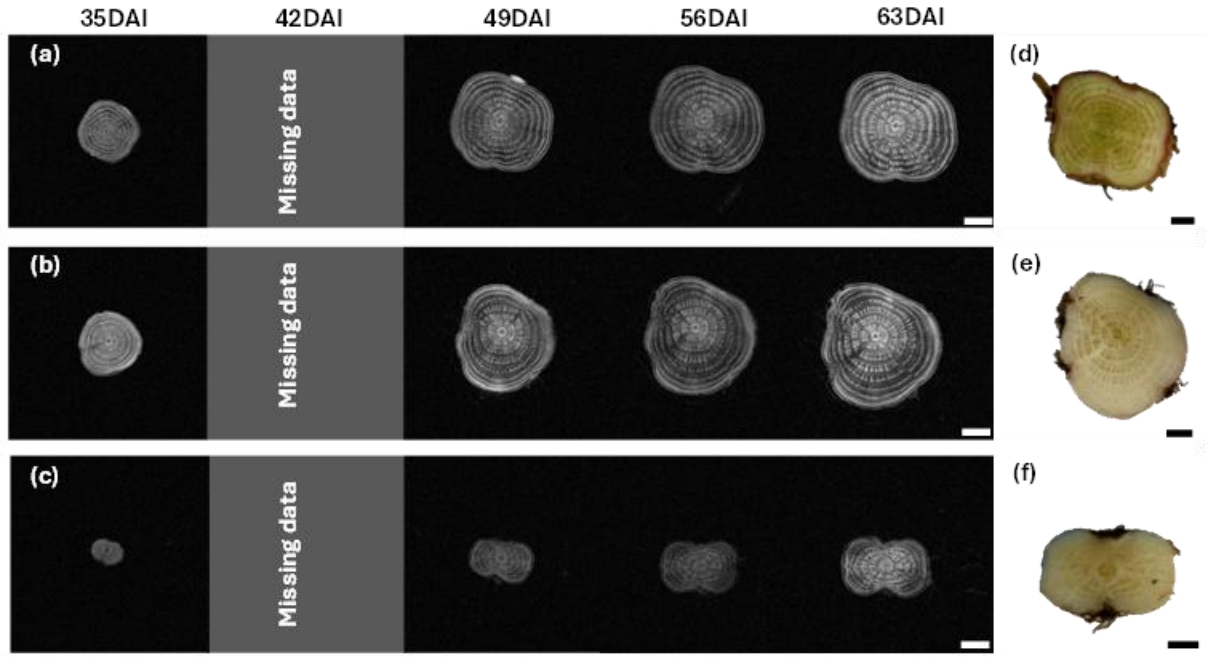

Figure A. S13. Cross-sectional anatomical features of diseased sample D2. (A-C) MRI and (D-F) RBG images for upper (A,D), middle (B,E) and lower (C,F) taproot slices. Scale bar, 0.5 cm.

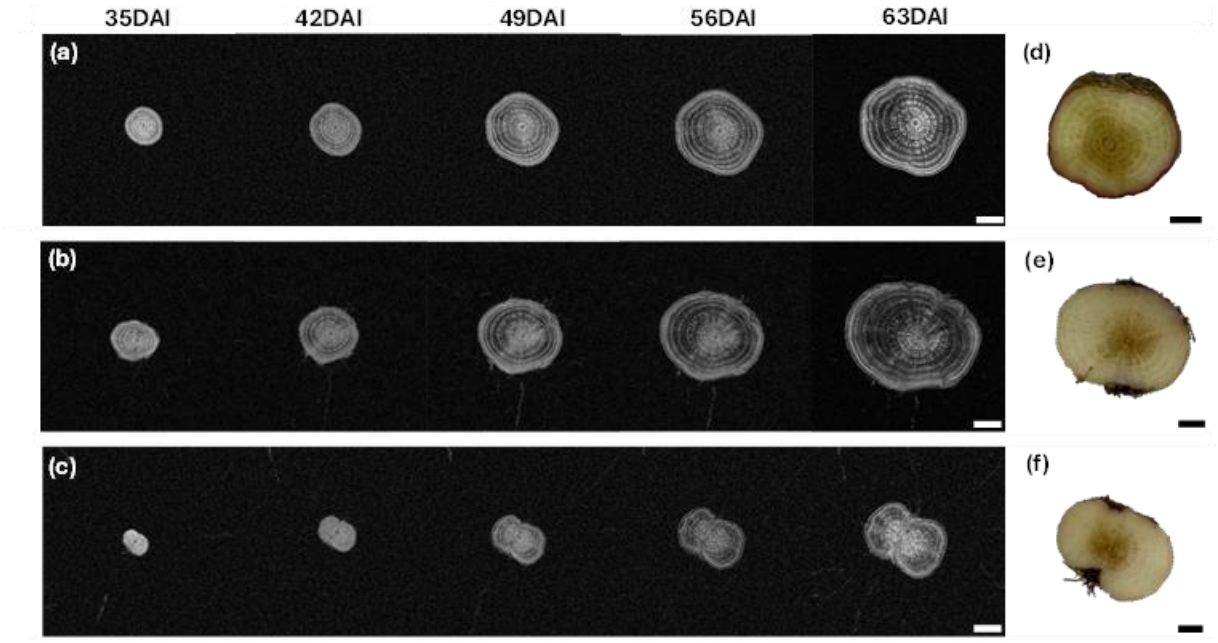

Figure A. S14. Cross-sectional anatomical features of diseased sample D3. (A-C) MRI and (D-F) RBG images for upper (A,D), middle (B,E) and lower (C,F) taproot slices. Scale bar, 0.5 cm.

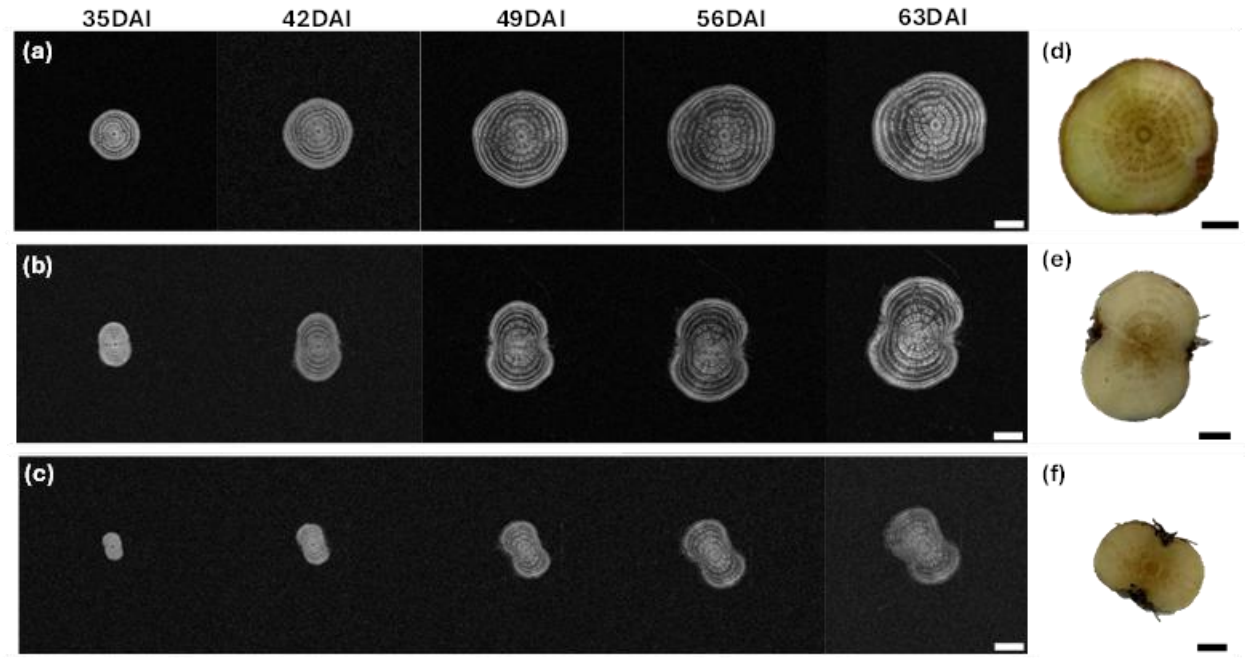

Figure A. S15. Cross-sectional anatomical features of diseased sample D4. (A-C) MRI and (D-F) RBG images for upper (A,D), middle (B,E) and lower (C,F) taproot slices. Scale bar, 0.5 cm.

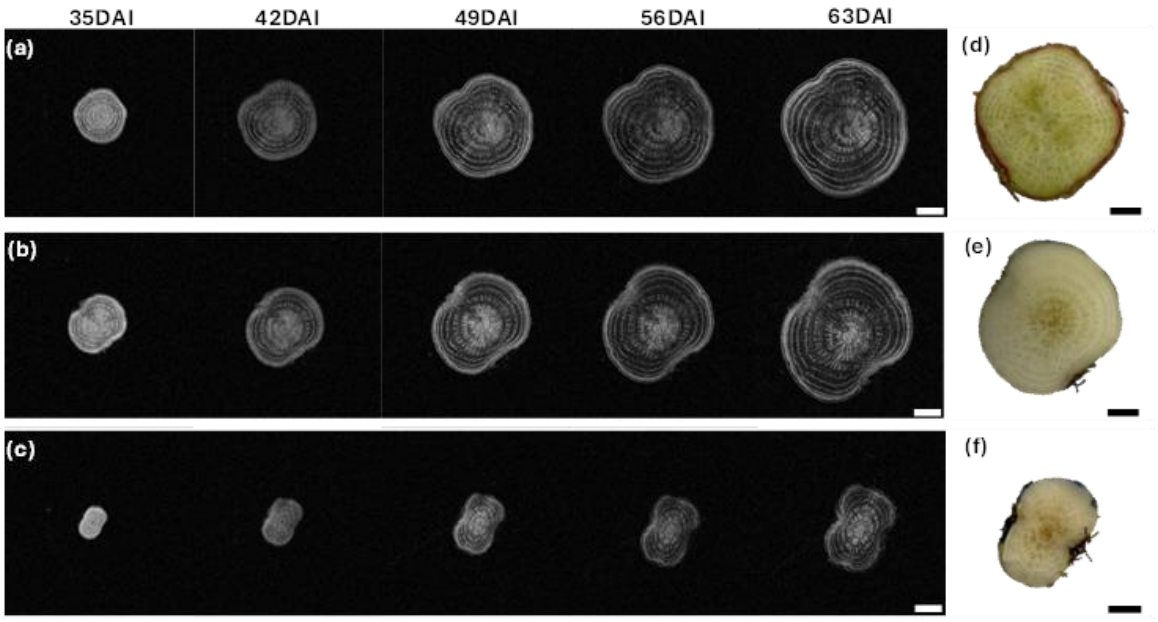

Figure A. S16. Cross-sectional anatomical features of diseased sample D5. (A-C) MRI and (D-F) RBG images for upper (A,D), middle (B,E) and lower (C,F) taproot slices. Scale bar, 0.5 cm.

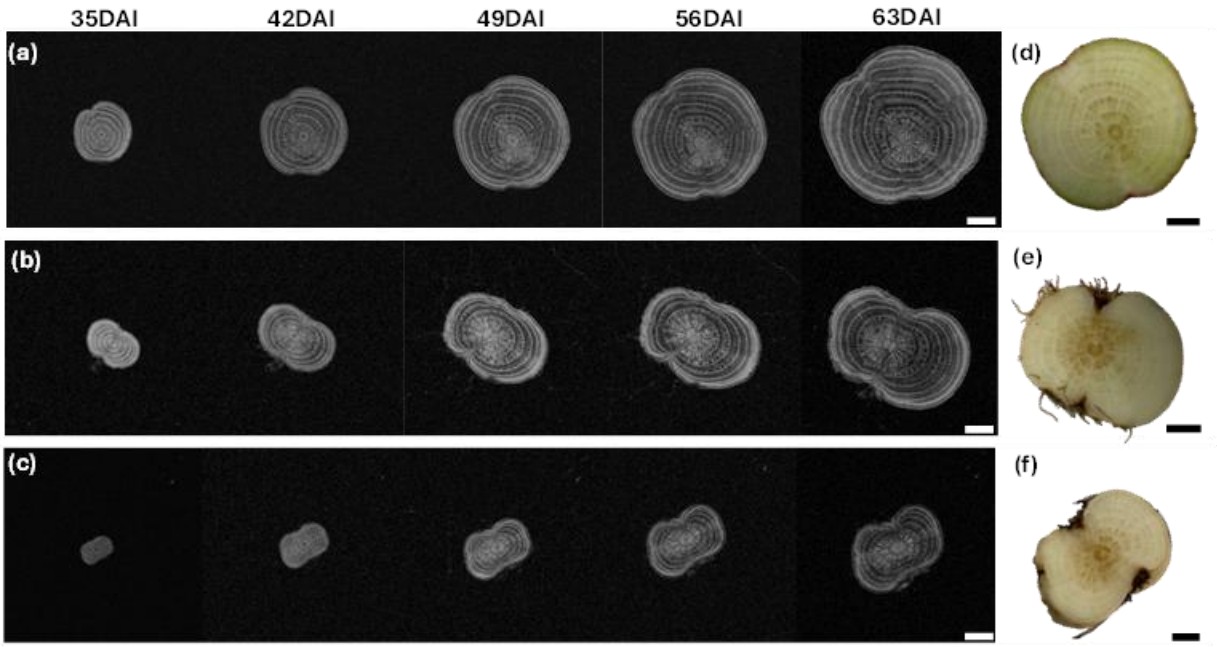

Figure A. S17. Cross-sectional anatomical features of diseased sample D6. (A-C) MRI and (D-F) RBG images for upper (A,D), middle (B,E) and lower (C,F) taproot slices. Scale bar, 0.5 cm.

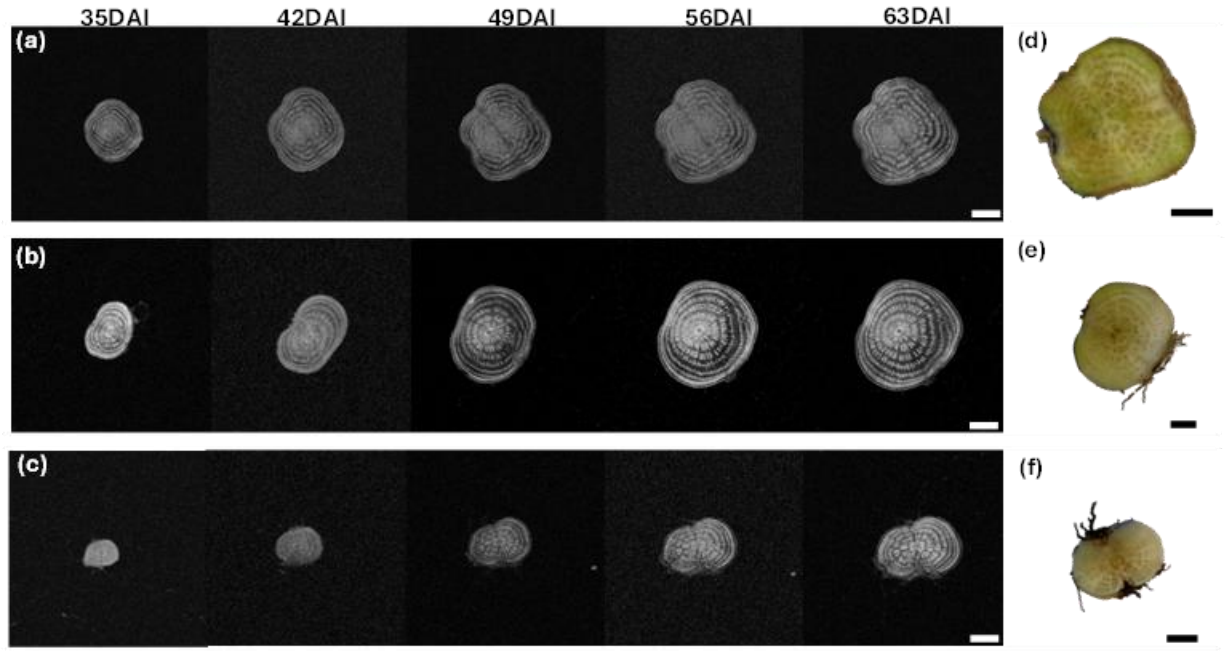

Figure A. S18. Cross-sectional anatomical features of diseased sample D7. (A-C) MRI and (D-F) RBG images for upper (A,D), middle (B,E) and lower (C,F) taproot slices. Scale bar, 0.5 cm.

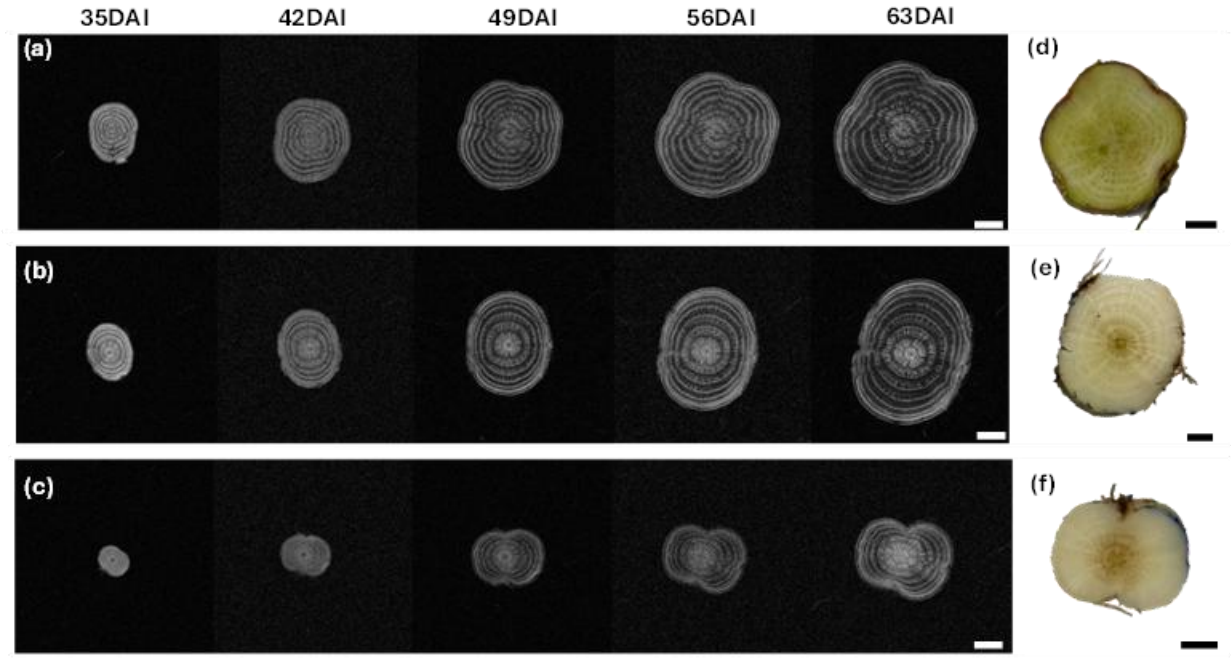

Figure A. S19. Cross-sectional anatomical features of diseased sample D8. (A-C) MRI and (D-F) RBG images for upper (A,D), middle (B,E) and lower (C,F) taproot slices. Scale bar, 0.5 cm.

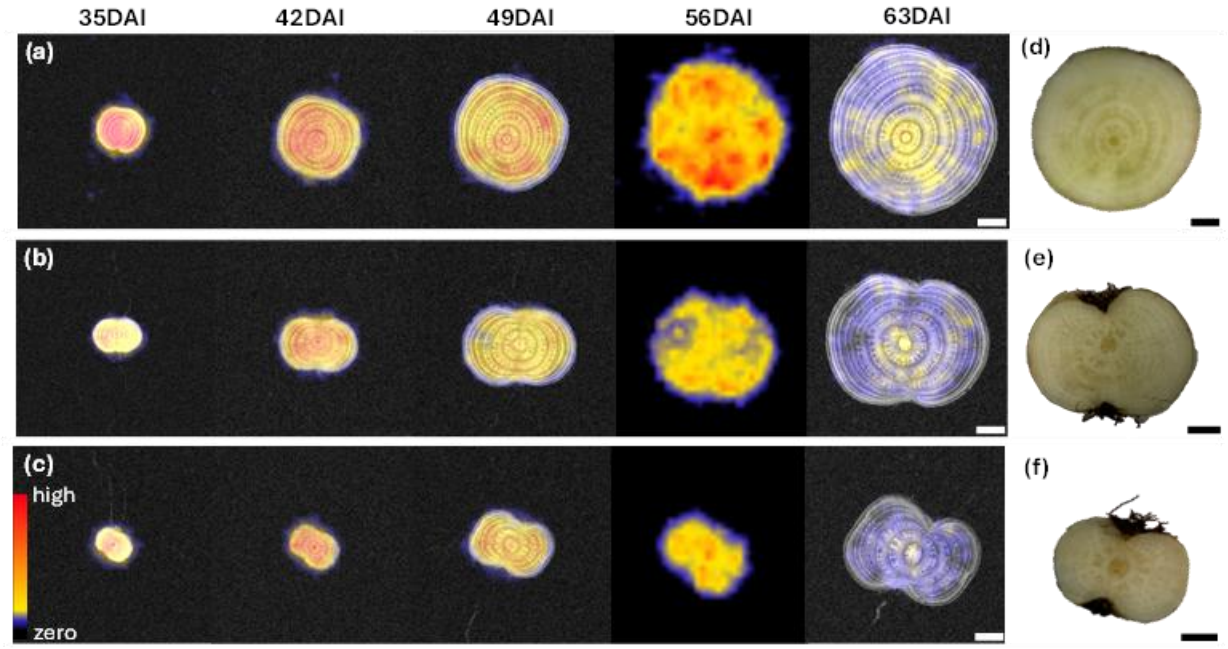

Figure A. S20. MRI-PET coregistration indicating tracer distribution within taproot for control sample C2. MRI data is missing for 56 DAI. Scale bar, 0.5 cm.

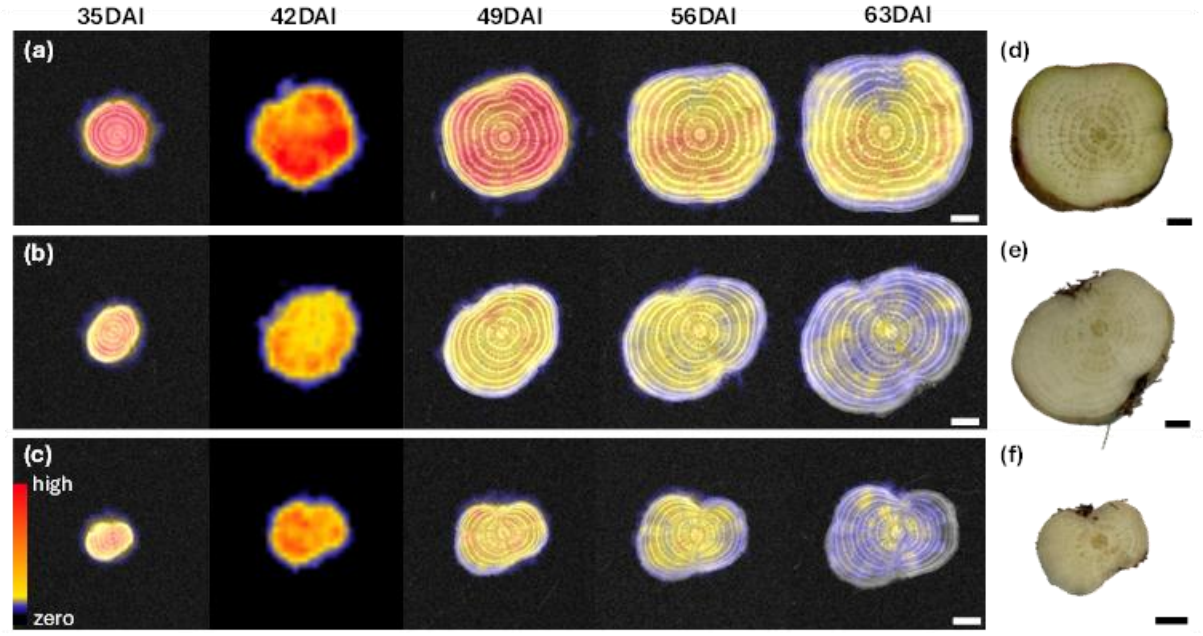

Figure A. S21. MRI-PET coregistration indicating tracer distribution within taproot for control sample C3. MRI data is missing for 42 DAI. Scale bar, 0.5 cm.

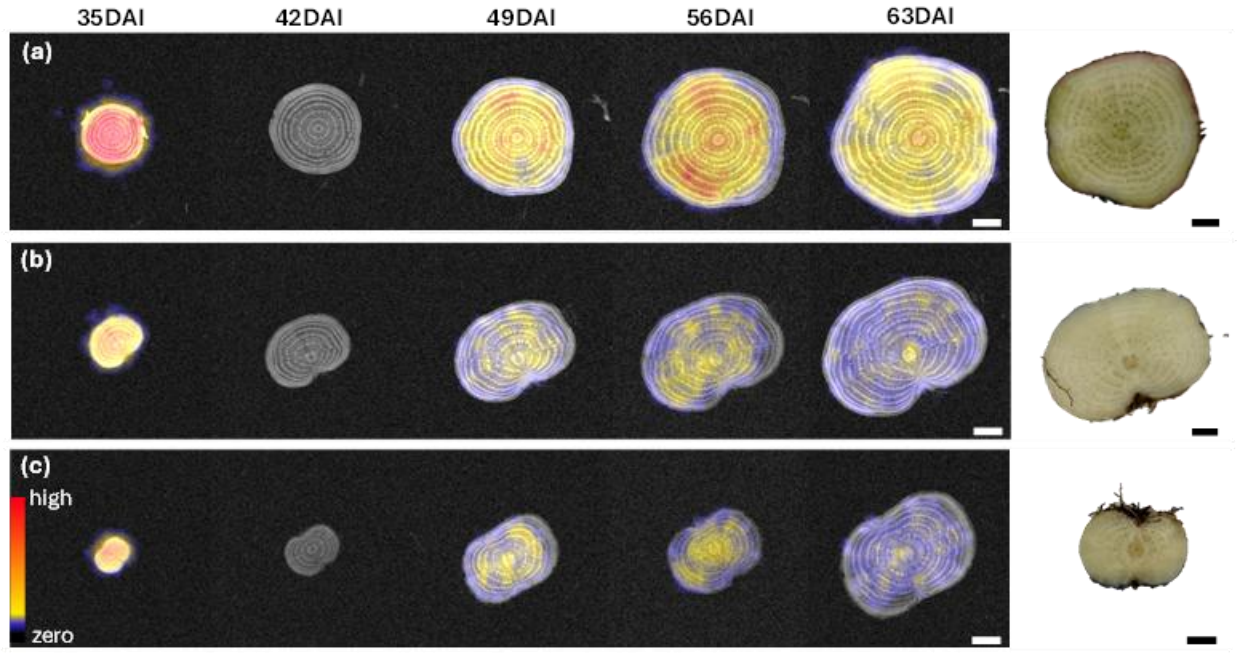

Figure A. S22. MRI-PET coregistration indicating tracer distribution within taproot for control sample C4. PET data is missing for 42 DAI. Scale bar, 0.5 cm.

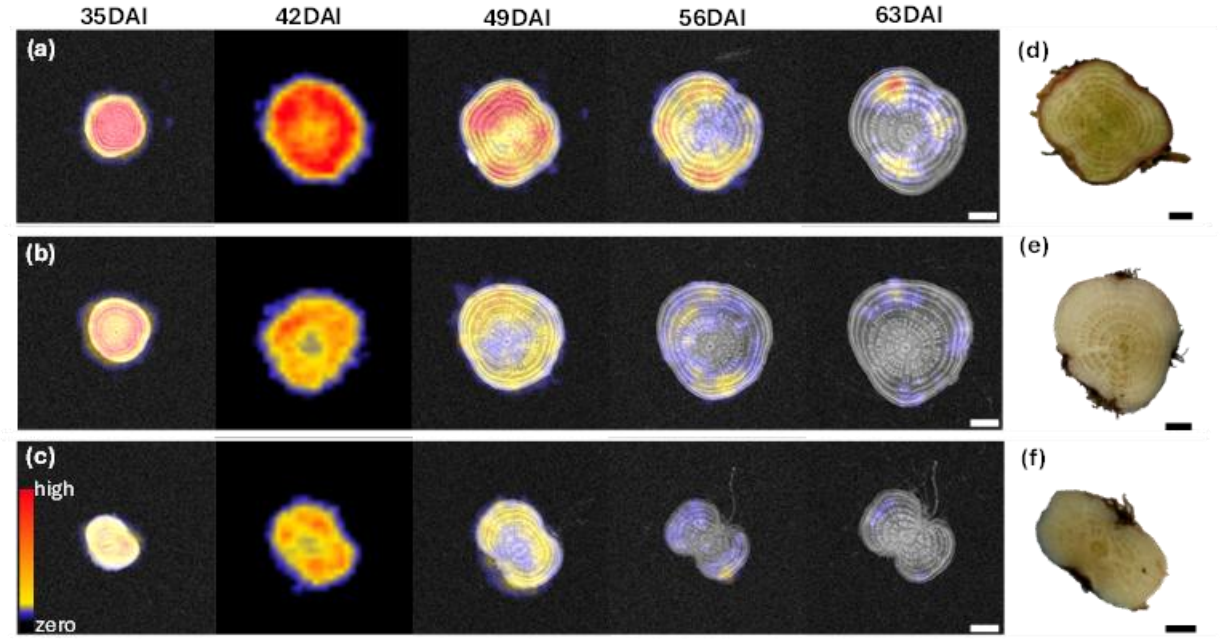

Figure A. S23. MRI-PET coregistration indicating tracer distribution within taproot for diseased sample D2. MRI data is missing for 42 DAI. Scale bar, 0.5 cm.

Table A. S1. Primers and probe for detection of 'Ca A. phytopatogenicus'.

	Sequence (5'-3')	Tm	labelling	Product size
Primer 1	tggaactcacagtagcggtt	58		90 nt
Primer 2	cacttttgccgctgatagtca	57		
Probe 1	aactcctgttgtttataaccagg	55	6-FAM/BHQ-1	

Table A. S2. Mean quantification cycle (Cq) values for each sample after qPCR for upper, mid and lower beet sections for each analyzed sample**.**

Sample ID	Upper	Mid	Lower
C3	N/D	N/D	N/D
C4	N/D	N/D	N/D
C10	N/D	N/D	N/A
C12	N/D	N/D	N/D
D1	27.01	25.87	24.91
D2	26.24	25.85	24.48
D3	26.44	28.40	26.42
D4	25.13	26.03	23.64
D5	29.70	28.50	28.53
D6	28.11	27.01	25.41
D7	25.93	26.03	24.34
D8	26.52	26.86	25.34

N/D, not detected, i.e. Cq > 35; N/A, not available.

Table A. S3. Taproot fresh weight and diameter after harvest.

Sample ID	Fresh weight [g]	Diameter [mm]
C1	43.8	26.6
C2	48.7	30.3
C3	52.4	32.7
C4	43.6	29.4
C5	44.5	31.5
C6	43.6	29.1
C7	48	30.2
C8	37.3	27
C9	35.5	30.5
C10	42.29	29.2
C11	40.7	27.7
C12	42.5	30.6
D1	28.2	24.2
D2	30.5	25.3
D3	31.8	26.7
D4	30.3	24.4
D5	37.4	26
D6	30.5	25.3
D7	41.7	29.5
D7	27.4	22.1
D8	41.7	27.4

Table A. S4. Heterogeneity in tracer distribution within several slices for each measured beet.

	Control				Infected	
DAI	C1	C2	C3	C4	D1	D2
35	0.36 ± 0.07	0.54 ± 0.07	0.34 ± 0.11	0.72 ± 0.34	0.64 ± 0.16	0.32 ± 0.06
42	0.45 ± 0.06	0.84 ± 0.25	N/A	N/A	0.78 ± 0.18	N/A
49	0.57 ± 0.07	0.59 ± 0.08	0.30 ± 0.04	0.64 ± 0.05	1.0 ±0.13	0.66 ±0.03
56	0.71 ± 0.17	N/A	0.42 ± 0.03	0.72 ± 0.05	1.06 ±0.26	1.08 ±0.11
63	0.44 ± 0.03	0.71 ± 0.09	0.50 ± 0.15	0.51 ± 0.06	1.33 ±0.17	1.40 ±0.14

DAI, days after inoculation. Values are mean ± STD: n= 10. N/A indicates missing data due to unsuccessful measurements.

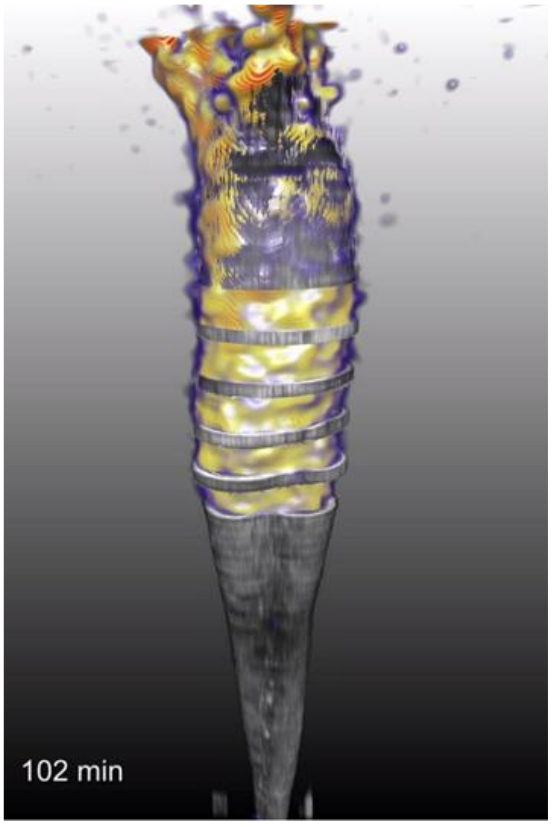

Video A. S1. Arrival and distribution of tracer in control taproot C1 visualized by MRI-PET co-registration. Video A S1 is available on bonndoc

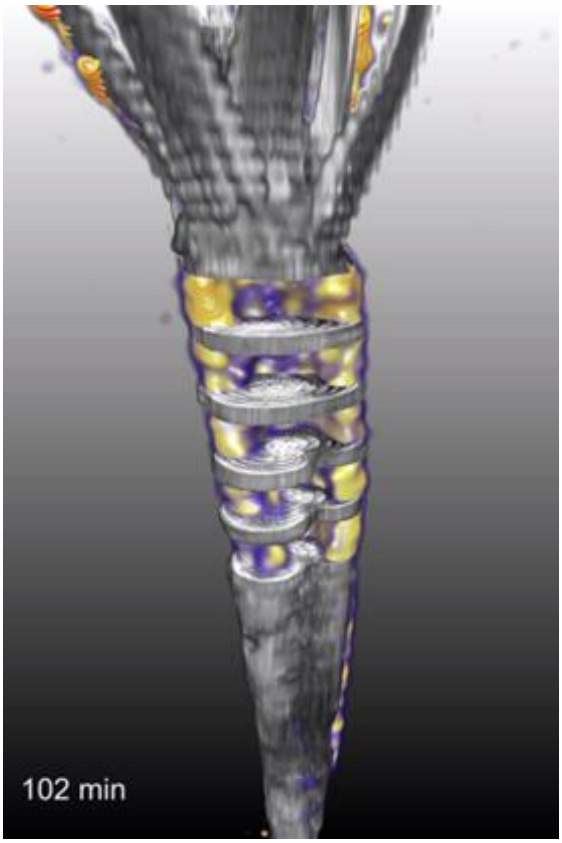

Video A. S2. Arrival and distribution of tracer in diseased taproot D1 visualized by MRI-PET co-registration.

Video A S2 is available on bonndoc

Appendix B: Supplementary materials for Chapter 3

Table B. S1. Parameters used to define ROIs for inner zones during radial zones analysis. Parameters were based on taproot geometry.

Table B. S2. Parameters used to define ROIs for mid zones during radial zones analysis. Parameters were based on taproot geometry.

Table B. S3. Parameters used to define ROIs for vertical sectioning analysis. Parameters were based on taproot geometry.

Figure B. S1. An example of sugar beet PET image with ROIs positioned directly around the whole girth of the taproot, indicating upper and lower ROIs sectioning during vertical sectioning analysis.

Table B. S1. Parameters used to define ROIs for inner zones during radial zones analysis. Parameters were based on taproot geometry.

Plant ID	d	Detector radius	Detector height	Number of detectors
C1	49	2	2	8
C1	56	2	2	8
C1	63	3	2	9
C1	70	4	2	10
C1	77	4	2	10
C1	84	4	2	10
C2	49	2	2	7
C2	56	3	2	8
C2	63	4	2	8
C2	70	4	2	8
C2	77	5	2	9
C2	84	5	2	9
C3	49	2	2	8
C3	56	2	2	8
C3	63	4	2	8
C3	70	2	5	9
C3	77	2	5	9
C3	84	2	6	9
C4	49	2	2	7
C4	56	2	3	7
C4	63	N/A	N/A	N/A
C4	70	4	2	8
C4	77	N/A	N/A	N/A
C4	84	5	2	9

N/A = missing data, d= days after planting.

Table B. S2. Parameters used to define ROIs for mid zones during radial zones analysis. Parameters were based on taproot geometry.

Plant ID	d	Detector radius	Detector height	Number of detectors
C1	49	3	2	8
C1	56	4	2	8
C1	63	5	2	9
C1	70	7	2	10
C1	77	7	2	10
C1	84	8	2	10
C2	49	3	2	7
C2	56	4	2	8
C2	63	5	2	8
C2	70	7	2	9
C2	77	8	2	9
C2	84	10	2	9
C3	49	2	2	8
C3	56	2	2	8
C3	63	5	2	8
C3	70	8	2	9
C3	77	10	2	9
C3	84	11	2	9
C4	49	4	2	7
C4	56	4	2	7
C4	63	N/A	N/A	N/A
C4	70	6	2	9
C4	77	N/A	N/A	N/A
C4	84	10	2	9

N/A = missing data, d= days after planting.

Table B. S3. Parameters used to define ROIs for vertical sectioning analysis. Parameters were based on taproot geometry.

Plant ID	d	Detector radius	Detector height	Number of detectors
C1	49	10	3	26
C1	56	15	3	26
C1	63	15	3	26
C1	70	17	3	26
C1	77	18	3	27
C1	84	20	3	27
C2	49	12	3	24
C2	56	12	3	24
C2	63	15	3	24
C2	70	18	3	24
C2	77	20	3	23
C2	84	20	3	25
D1	49	12	3	24
D1	56	N/A	N/A	N/A
D1	63	14	3	24
D1	70	16	3	24
D1	77	17	3	24
D1	84	20	3	24
D2	49	12	3	24
D2	56	16	3	26
D2	63	18	3	26
D2	70	16	3	24
D2	77	18	3	23
D2	84	20	3	23
C3	49	11	3	23
C3	56	15	3	24
C3	63	17	3	26
C3	70	20	3	26
C3	77	21	3	24
C3	84	22	3	23
C4	49	11	3	23
C4	56	13	3	23
C4	63	N/A	N/A	N/A
C4	70	16	3	23
C4	77	N/A	N/A	N/A
C4	84	20	3	23

N/A = missing data, d= days after planting.

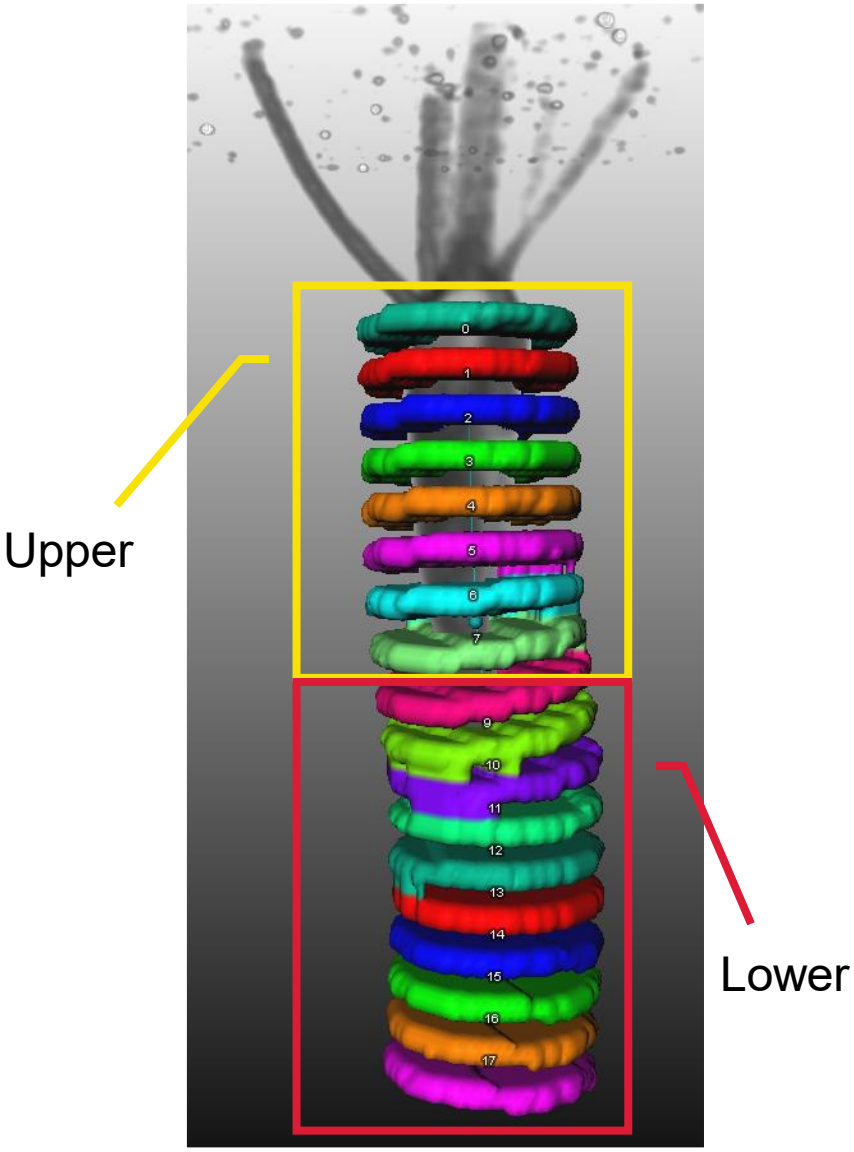

Figure B. S1. An example of sugar beet PET image with ROIs positioned directly around the whole girth of the taproot, indicating upper and lower ROIs sectioning during vertical sectioning analysis.

Appendix C: Supplementary materials for Chapter 4

Figure C. S1. Distribution patterns of ^{11}C tracer over a cross-section of sugar beet taproot for different labelling approaches prior to defoliation manipulation

Figure C. S2. Maximum intensity projection of MRI-PET cross-sections of sugar beet taproot, indicating the distribution pattern of ^{11}C tracer over a cross-section of sugar beet taproot for partially defoliated sugar beet plant (ID P2)

Figure C. S3. Maximum intensity projection of MRI-PET cross-sections of sugar beet taproot, indicating the distribution pattern of ^{11}C tracer over a cross-section of sugar beet taproot for partially defoliated sugar beet plant (ID P3).

Video C. S1. Trajectory of tracer movement along the vertical axis of taproot after single leaf labelling.

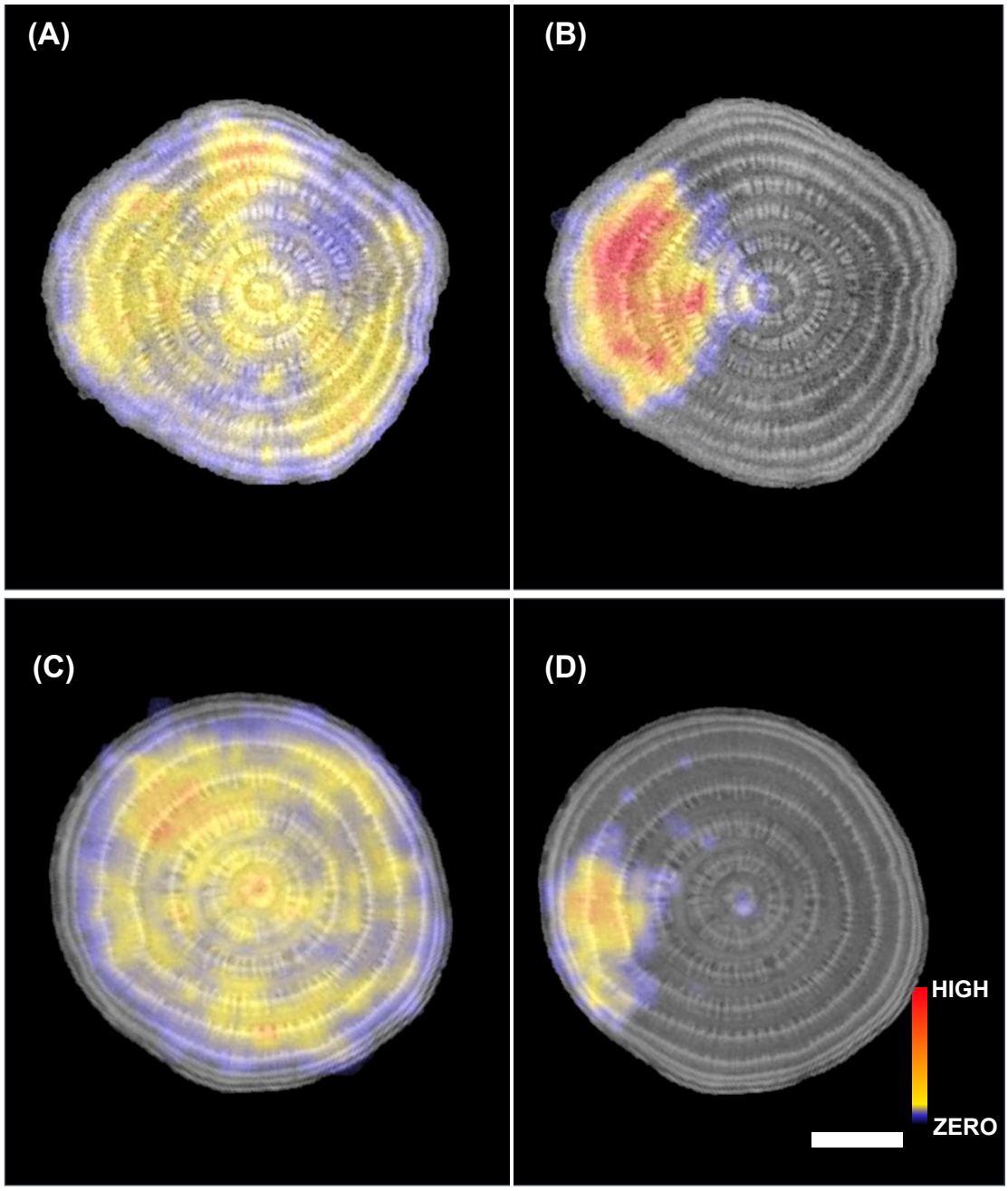

Figure C. S1. Distribution patterns of ^{11}C tracer over a cross-section of sugar beet taproot for different labelling approaches prior to defoliation manipulation. (A,C) distribution of ^{11}C tracer within the taproot for whole shoot $^{11}CO_2$ labelling prior to defoliation for samples 92 and P3, respectively (WSL, morning) and (B,D) distribution of ^{11}C tracer within the taproot for a single leaf $^{11}CO_2$ labelling prior to defoliation for samples 92 and P3, respectively (SLL, midday), Colored image parts represent PET, while grey image parts represent MRI. Areas with cooler colors (grey and blue) indicate a low ^{11}C tracer signal, while areas with warmer colors (yellow and red) indicate a high ^{11}C tracer signal. White bar, 0.5 cm

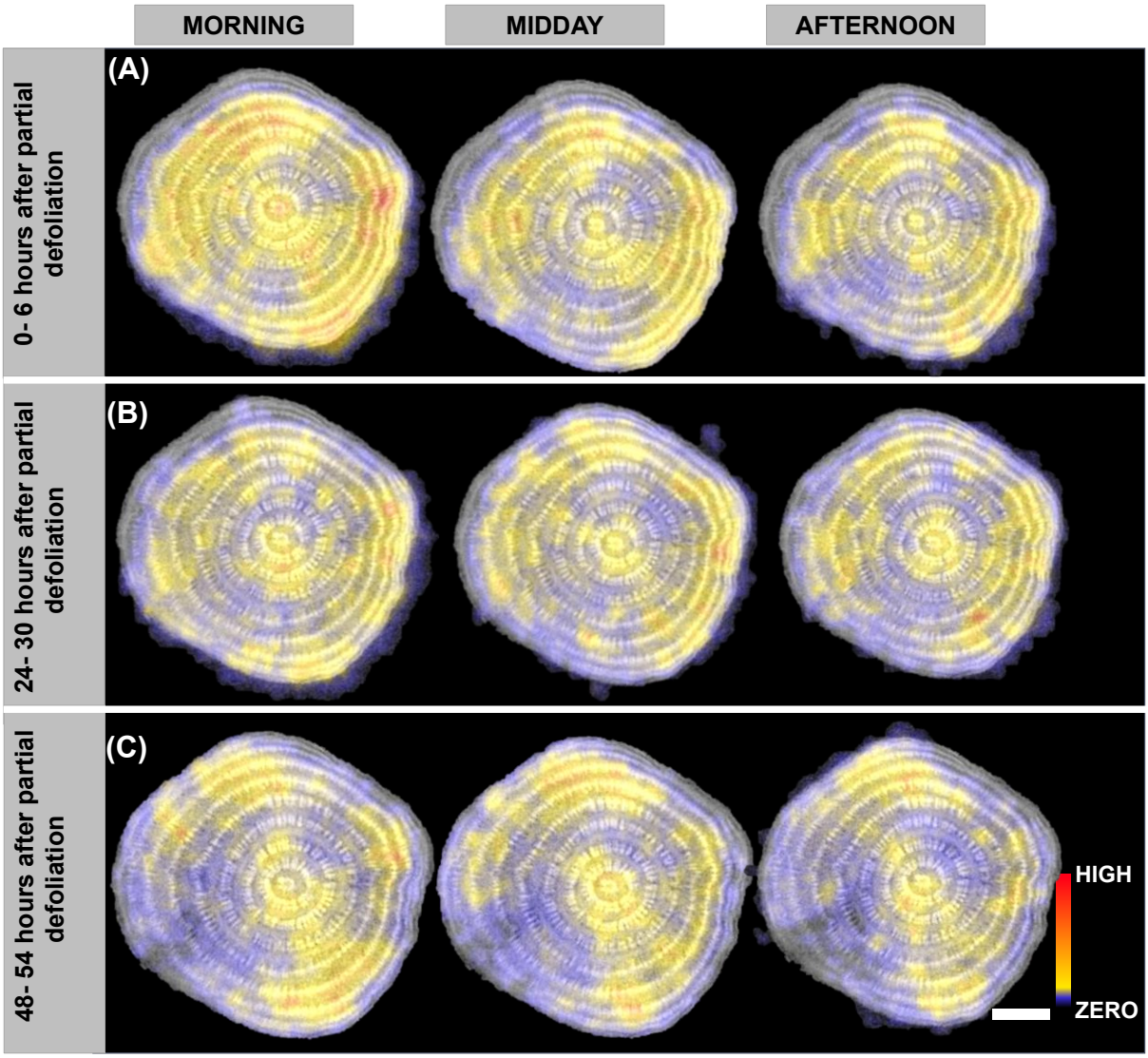

Figure C. S2. MIP of MRI-PET cross-sections of sugar beet taproot, indicating the distribution pattern of ^{11}C tracer over a cross-section of sugar beet taproot for partially defoliated sugar beet plant (ID P2). The distribution pattern of ^{11}C tracer over a cross-section of sugar beet taproot (A) at 0-6 hours after partial defoliation, (B) t at 24-30 hours after partial defoliation and (C) at 48-54 hours after partial defoliation. Colored image parts represent PET, while grey image parts represent MRI. Areas with cooler colors (grey and blue) indicate a low ^{11}C tracer activity while areas with warmer colors (yellow and red) indicate a high ^{11}C tracer activity. Measurements were obtained in the morning, midday and afternoon. White bar, 0.5 cm.

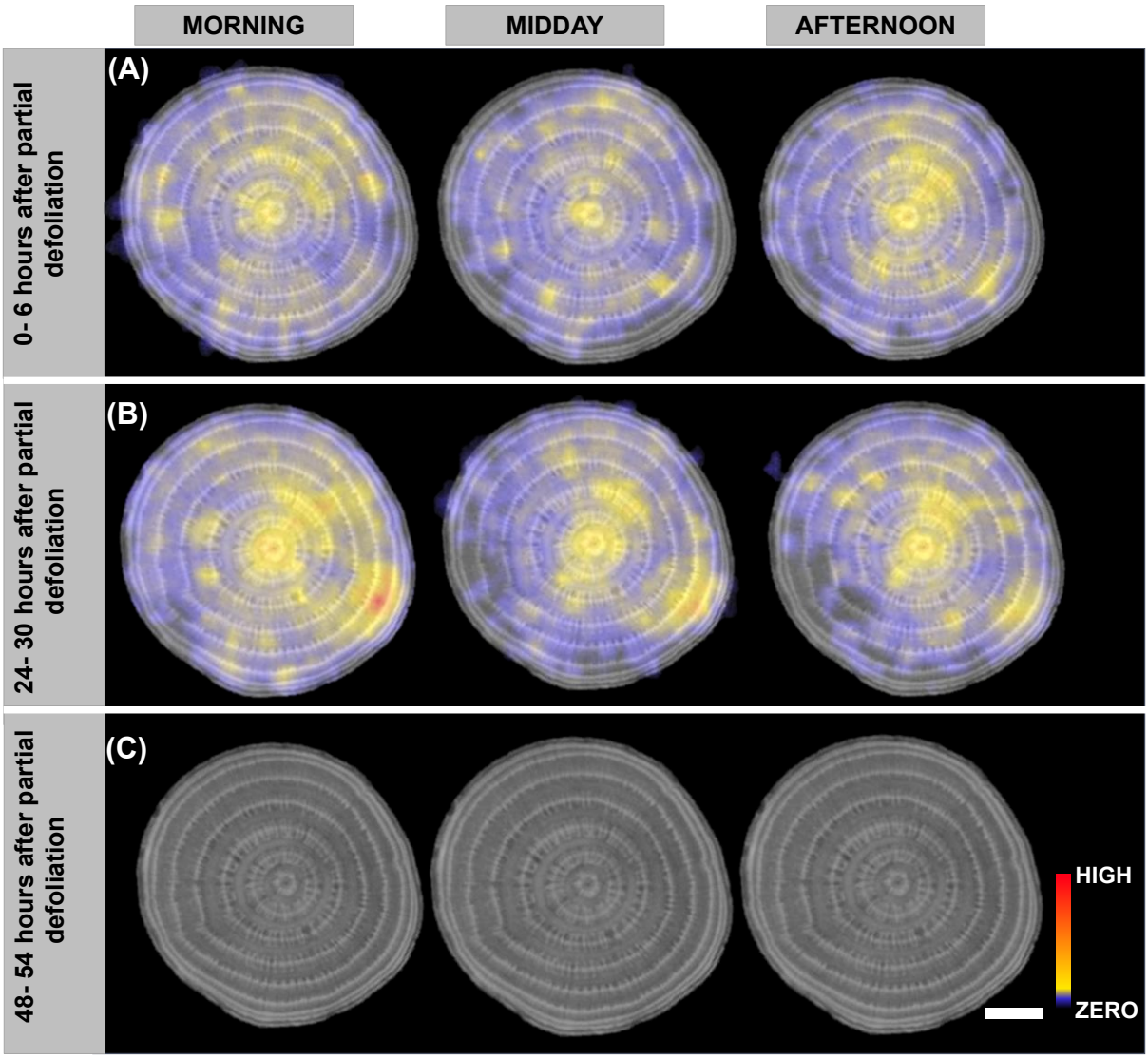

Figure C. S3. MIP of MRI-PET cross-sections of sugar beet taproot, indicating the distribution pattern of ^{11}C tracer over a cross-section of sugar beet taproot for partially defoliated sugar beet plant (ID P3). The distribution pattern of ^{11}C tracer over a cross-section of sugar beet taproot (A) at 0-6 hours after partial defoliation, (B) t at 24-30 hours after partial defoliation and (C) at 48-54 hours after partial defoliation. Colored image parts represent PET, while grey image parts represent MRI. Areas with cooler colors (grey and blue) indicate a low ^{11}C tracer activity while areas with warmer colors (yellow and red) indicate a high ^{11}C tracer activity. PET data is missing for measurements in C. Measurements were obtained in the morning, midday and afternoon. White bar, 0.5 cm.

Table C. S1. Temporal assimilation rates [µmol/LA*s] per single leaf (yellow cells) or per whole shoot of sugar beet plant before and after partial defoliation. All single leaf measurements were performed once (during midday) before partial defoliation. Green and red cells indicate when the highest and lowest assimilation rates per whole shoot were recorded, respectively. N/A; not available

Sample ID	Period	Before defoliation	0- 6 hours after defoliation	24-30 hours after defoliation	48-54 hours after defoliation
P1	morning	0.128 ± 0.003	0.116 ± 0.002	0.108 ± 0.002	0.102 ± 0.006
	Midday	0.034 ± 0.001	0.118 ± 0.002	0.110 ± 0.002	0.116 ± 0.002
	afternoon	0.107 ± 0.005	0.111 ±0.003	0.101 ± 0.002	0.120 ±0.002
P2	morning	N/A	0.052 ± 0.004	0.082 ± 0.002	0.088 ± 0.007
	Midday	0.030 ± 0.002	0.066 ± 0.002	0.091 ± 0.002	0.108 ± 0.002
	afternoon	0.041± 0.007	0.075 ± 0.002	0.097 ± 0.001	0.116 ± 0.002
P3	morning	0.025 ±0.006	0.063 ± 0.002	0.061 ± 0.001	0.097 ± 0.011
	Midday	0.055 ± 0.005	0.074 ± 0.003	0.061 ± 0.002	0.121 ± 0.003
	afternoon	0.034 ± 0.006	0.082 ± 0.002	0.064 ± 0.001	0.132 ± 0.001

Table C. S2. Temporal assimilation rates [µmol/LA*s] per single leaf (yellow cell) or per whole shoot of sugar beet plant before during and after removal of shade. Green and red cells indicate when the highest and lowest assimilation rates per shoot were recorded, respectively.

Sample ID	Period	Before shading	0-6 hours during shading	24-30 hours during shading	After removal of shade
S1	morning	0.018 ± 0.005	0.005 ± 0.004	0.046 ± 0.002	0.101 ± 0.002
	Midday	0.077 ± 0.004	0.022 ± 0.004	0.051 ± 0.003	0.106 ± 0.002
	afternoon	0.005 ± 0.004	0.031 ± 0.004	0.055 ± 0.002	0.109 ± 0.002

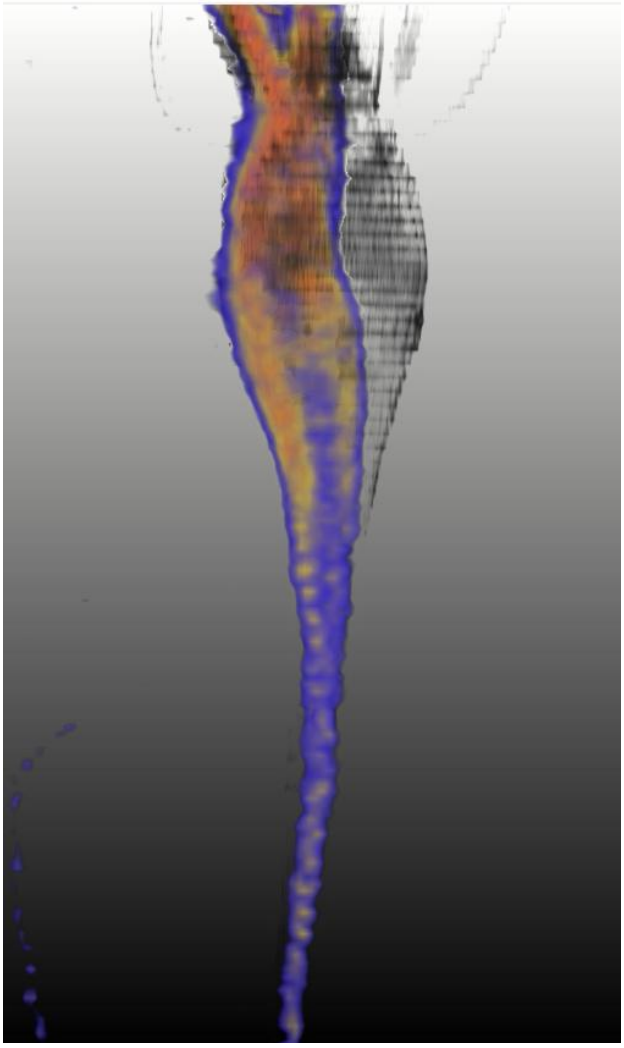

Video C. S1. Trajectory of tracer movement along the vertical axis of taproot after single leaf labelling visualized by MRI-PET coregistration. Video C S1 is available on bonndoc

Appendix D: Publications, presentations and posters contributions

Agyei, K., Detring, J., Metzner, R., Huber, G., Pflugfelder, D., Eini, O., Varrelmann, M., Mahlein, A.-K., & Koller, R. (2025). Syndrome “basses richesses” disease induced structural deformations and sectorial distribution of photoassimilates in sugar beet taproot revealed by combined MRI-PET. *Plant Phenomics.* https://doi.org/10.1016/j.plaphe.2025.100053

Agyei, K., Detring, J., Metzner, R., Huber, G., Pflugfelder, D., Eini, O., Varrelmann, M., Mahlein, A.-K., & Koller, R. (2025). Tomographic imaging reveals biotic disease effects in sugar beet taproot. Cover image of the Journal of Plant Phenomics. Vol 7, Issue 2. June, 2025.

Invited talk – KWS Einbeck, Germany, May 2025.

Speaker – 8th International Plant Phenotyping Symposium, Lincoln, USA, Oktober 2024.

Poster – International Society of Root Research Symposium, Leipzig, Deutschland, June 2024.

Acknowledgements

Special thanks to Dr. Robert Koller and Dr. Gregor Huber, for their patience, guidance and unwavering support throughout this work. I am also grateful to my co-supervisors, Dr. Daniel Pflugfelder and Dr. Ralf Metzner, whose expertise greatly enriched this project. My appreciation extends to the entire Enabling Technologies group at IBG-2 for their continuous support.

I am equally thankful to Prof. Dr. Uwe Rascher and Prof. Dr. Anne-Kathrin Mahlein for their insightful guidance and invaluable advice.

Finally, I would like to thank my family, friends and colleagues for their constant encouragement and support.